Indirect Experimental Techniques For Nuclear Astrophysics

By

RAJKUMAR SANTRA

PHYS05201604018

Saha Institute Of Nuclear Physics, Kolkata

A thesis submitted to the

Board of Studies in Physical Sciences

In partial fulfillment of requirements

For the Degree of

DOCTOR OF PHILOSOPHY

of

HOMI BHABHA NATIONAL INSTITUTE

December, 2020

Homi Bhabha National Institute[1]

Recommendations of the Viva Voce Committee

As members of the Viva Voce Committee, we certify that we have read the dissertation prepared by **Rajkumar Santra** entitled **Indirect Experimental Techniques for Nuclear Astrophysics** and recommend that it may be accepted as fulfilling the thesis requirement for the award of Degree of Doctor of Philosophy.

Prof. Anjali Mukherjee Chairperson	Anjali Mukherjee	26.05.21 (Signature and Date)
Prof. Subinit Roy Guide/Convener	Subinit Roy	25.05.2021 (Signature and Date)
Prof. Chinmay Basu Co-guide	Chinmay Basu	29.05.2021 (Signature and Date)
Prof. Samit Mandal External Examiner	Samit Kr Mandal	Digitally signed by Prof Samit Kr Mandal Date: 2021.05.26 18:31:53 +05'30' (Signature and Date)
Prof. Maitreyee Saha Sarkar Member 1	Maitreyee Saha Sarkar	27/5/2021 (Signature and Date)
Prof. Sukalyan Chattopadhay Member 2	Sattejee	29/05/21 (Signature and Date)
Prof. Chandana Bhattacharya Member 3	C Bhattacharya	28.05.21 (Signature and Date)

Final approval and acceptance of this thesis is contingent upon the candidate's submission of the final copies of the thesis to HBNI.

I/We hereby certify that I/we have read this thesis prepared under my/our direction and recommend that it may be accepted as fulfilling the thesis requirement.

Date: 25.05.2021

Place: Kolkata

Chinmay Basu 29.05.2021

Signature

Co-guide (if any)

Subinit Roy

Signature 25.05.2021

Guide

[1] This page is to be included only for final submission after successful completion of viva voce.

STATEMENT BY AUTHOR

This dissertation has been submitted in partial fulfillment of requirements for an advanced degree at Homi Bhabha National Institute (HBNI) and is deposited in the Library to be made available to borrowers under rules of the HBNI.

Brief quotation from this dissertation are allowable without special permission, provided that accurate acknowledgement of source is made. Requests for permission for extended quotation from or reproduction of this manuscript in whole or in part may be granted by the Competent Authority of HBNI when in his or her judgement the proposed use of the material is in the interests of scholarship. In all other instances, however, permission must be obtained from the author.

Rajkumar Santra

Rajkumar Santra

DECLARATION

I, hereby declare that the investigation presented in the thesis has been carried out by me. The work is original and has not been submitted earlier as a whole or in part for a degree/diploma at this or any other Institution/University.

Rajkumar Santra

Dedicated to my 'Parents'

ACKNOWLEDGMENTS

I gratefully acknowledge the constant and invaluable academic and personal support received from my supervisor Prof. Subint Roy throughout my thesis work. I am really thankful and indebted to him for having been the advisor everyone would like to have, for their clear and enthusiastic discussions, for helping me to find my firm grounding in the research problem and without his dedicated supervision it would have been never possible to complete this thesis. I am very much indebted to Dr. Balaram Dey, Dr. Haridas Pai, Dr. Subhandu Rajbansi and Dr. Suprita Chakraborty for their suggestions and help through out my Ph. D. work. I would like to give my sincere thanks to Prof. Rudrajyoti Palit and Mr. Md. S. R. Laskar from TIFR and Prof. Maitreyee Saha Sarkar, Prof. Chinmay Basu and Prof. Anjali Mukherjee of SINP for help and suggestions at various stages. I am indebted to Prof. Chandana Bhattacharya and Dr. Tapan Kumar Rana for their advice and support during and after the experiment at VECC, Kolkata. I would also like to thank Prof. G. Gangopadhyay, Calcutta University for his help and advice at certain stages of this project. The help and advice received from Mr. Sujib Chatterjee and Mr. Kaushik Chatterjee during the developmental work carried out by me are also much appreciated. The help of all the collaborators in the present work, from different institutions (VECC, TIFR, SINP) in India are gratefully acknowledged. The effort of the operators of the accelerators at VECC and TIFR are also acknowledged with gratitude. Thank you very much. I would like to thank my friends Ashis, Saikat, Tanmoy, Dipali, Ashok da, Sathi for their support and constant encouragement during my tenure as a Ph.D student at SINP. I sincerely apologize inadvertent omission of any name from the above list of acknowledgment.

Rajkumar Santra

List of Publications arising from the thesis

Journals

1. "Asymptotic normalization coefficients from transfer reaction and R-martix analysis of direct capture in ^{22}Ne(p, γ)^{23}Na reaction ", **Rajkumar Santra**, Suprita Chakraborty, Subnit Roy, Phys. Rev. C, **2020**, 101, 025802.

2. "Nuclear level density of ^{69}Zn from gamma gated particle spectrum and its implication on ^{68}Zn(n, γ)^{69}Zn capture cross section", **Rajkumar Santra**, Balaram Dey, Subinit Roy, Md.S.R. Laskar, R. Palit, H. Pai, S. Rajbanshi, Sajad Ali, Saikat Bhattacharjee, F.S. Babra, Anjali Mukherjee, S. Jadhav, Balaji S. Naidu, Abraham T. Vazhappilly, Sanjoy Pal, Physics Letters B, **2020**, 806, 135487.

Conferences

1. "Study of low energy resonances in ^{23}Na from transfer reaction ^{22}Ne (^{3}He, d) ^{23}Na and astrophysical implication ", **Rajkumar Santra**, and Subinit Roy, Proc. DAE-BRNS Symp. Nucl. Phys. (India), **2017**, 62, 680-681.

2. "Experimental nuclear level density of ^{69}Zn and its application in ^{68}Zn(n, γ)^{69}Zn capture cross-section estimation ", **Rajkumar Santra**, Balaram Dey, Subinit Roy, Md. S. R. Laskar, H. Pai, R. Palit, Subhendu Rajbanshi, Sajad Ali, Saikat Bhattacharjee, Anjali Mukherjee, S. Jadhav, Balaji S Naidu, Abraham T. Vazhappilly, Sanjoy Pal, Proc. DAE-BRNS Symp. Nucl. Phys. (India) **2019**, 64, 572-573.

Rajkumar Santra

Others

1. "Charged particle detection with the low-cost BPW21 Si Photodiode ", H. Pai, **Rajkumar Santra**, Sujib Chatterjee, Dwijendra Das, Subinit Roy. Nuclear Inst. and Methods in Physics Research A, **2020**, 955, 163363.

2. "A simultaneous R-matrix analysis of (α - α) elastic scattering and capture reaction data ", Suprita Chakraborty, **Rajkumar Santra**, Subinit Roy, Avijit Mukherjee, and V.M. Datar. Proc. DAE-BRNS Symp. Nucl. Phys. (India), **2018**, 63, 358-359.

3. "Investigation of structural evolution in ^{70}Ge", **Rajkumar Santra**, Subhendu Rajbanshi, Haridas Pai, Subinit Roy, Sajad Ali, Balaram Dey, Saikat Bhattacharjee, Anjali Mukherjee, F. S. Babra, Md. S. R. Laskar, Sanjoy Pal, R. Palit. Proc. DAE-BRNS Symp. Nucl. Phys. (India) **2018**, 63, 350-351 .

4. "Population of n-unbound states of ^{65}Ni via one neutron transfer reaction ^{64}Ni(^{9}Be, ^{8}Be)", **Rajkumar Santra**, Subinit Roy, Haridas Pai, Subhendu Rajbanshi, Sajad Ali, Balaram Dey, Saikat Bhattacharjee, Anjali Mukherjee, F. S. Babra, Md. S. R. Laskar, Sanjoy Pal, R. Palit. Proc. DAE-BRNS Symp. Nucl. Phys. (India) **2018**, 63, 802-803.

5. "Charged particle detection with the low-cost BPW21 Si Photodiode ", H. Pai, **Rajkumar Santra**, Sujib Chatterjee, Dwijendra Das, Subinit Roy. Proc. DAE-BRNS Symp. Nucl. Phys. (India), **2019**, 64, 908-909.

6. "Fission dynamics at energies far above the Coulomb barrier", Md. Moin Shaikh, T. K. Ghosh, A. Sen, D. Paul, K. Atreya, C. Bhattacharya, S. Kundu, T. K. Rana, S. Nandi, G. Mukherjee, J. K. Meena, S. Manna, Pratap Roy, R. Pandey, S. Mukhopadhyay, **Rajkumar Santra**. Proc. DAE-BRNS Symp. Nucl. Phys. (India), **2019**, 64, 321-322.

7. "Fusion of ^{16}O + ^{165}Ho at Deep Sub-barrier Energies ", Saikat Bhattacharjee, Ashish Gupta, **Rajkumar Santra**, D. Chattopadhyay, N. Deshmukh, A. Mukherjee, S. Gupta, S.K. Pandit, V.V. Parkar, K. Ramachandran, K. Mahata, A. Shrivastava, Re-

Rajkumar Santra

becca Pachuau, S. Rathi. Proc. DAE-BRNS Symp. Nucl. Phys. (India), **2019**, 64, 405-406.

8. "Fission fragment mass distribution of ^{225}Pa ", K. Atreya, T. K. Ghosh, A. Sen, MD. Moin Shaikh, D. Paul, C. Bhattacharya, Samir Kundu, S. Manna, G. Mukherjee, S. Nandi, R. Pandey, T. K. Rana, Pratap Roy, S. Mukhopadhyay, **Rajkumar Santra**. Proc. DAE-BRNS Symp. Nucl. Phys. (India), **2019**, 64, 395-396.

Rajkumar Santra

Contents

List of Figures

List of Tables

1.1 Conclusion

1.1.1 The ^{22}Ne(p,γ)^{23}Na capture reaction

A consistent analysis of direct capture reaction in ^{22}Ne(p,γ)^{23}Na has been performed within the *R*-matrix framework. constrained with the asymptotic normalization constants of the bound states of ^{23}Na obtained from the transfer reaction calculation. Asymptotic normalization constants have been extracted from finite DWBA analysis of ^{22}Ne(^{3}He,d)^{23}Na transfer data.

Astrophysical S-factor data for capture to the bound states of ^{23}Na have been reproduced from the analysis. Contribution of capture through the sub-threshold resonance at 8664 keV excitation in the total capture to the ground state of ^{23}Na has been delineated. The observed rise in the ground state capture data is reproduced nicely. The total direct capture S-factor at zero relative energy, $S_{DC}(0)$, is found to be 48.8 ± 9.5 having less uncertainty.

The total reaction rate obtained as a function of temperature differs from the recent estimations by Ferraro *et al.* in the temperature window of 0.1 GK ≤ T ≤ 0.2 GK. The difference is caused due to a slightly higher contribution from direct plus sub-threshold capture to the ground state. However, the present uncertainty in the total rate in this region is relatively higher due to the uncertainty in the resonance strength of the unbound state extracted from transfer angular distribution data. However, in T ≤ 0.1 GK, the uncertainty in the rate is comparable with the result of Ferraro, *et al.*.

1.1.2 The ^{68}Zn(n, γ)^{69}Zn capture reaction

In summary, the low energy (E_γ = 152 and 332 keV) γ-gated alpha emission spectra from the reaction ^{9}Be + ^{64}Ni have been measured. The γ-gated alpha energy spectra is predominantly from the compound nuclear events ensured by the even spin, odd parity (6^- or 8^-) of the decaying states in ^{68}Zn, the residual nucleus from αn decay of compound nucleus ^{73}Ge. The measured alpha energy spectra have been compared with the statistical model calculations to extract the NLD parameter and utilized to extract the level density

of ^{69}Zn nucleus as a function of excitation energy. The obtained NLD parameter evaluated at neutron separation has been used in TALYS code to calculate the ^{68}Zn(n, γ)^{69}Zn capture cross-sections. The excellent agreement with measured (n, γ) cross-section achieves the objective of experimentally constraining the parameters of the statistical model for a more accurate description of astrophysical reactions.

1.1.3 The α α(n, γ)^{9}Be capture reaction

The scattered α-particles from ^{9}Be target in singles and in coincidence with the two decay α-s from a resonant state of ^{9}Be were measured. In scattered α spectrum (both in singles and in coincidence) the $1/2^{+}$ state at 1.68 MeV is identified and fitted with Gaussian functions.The Gaussian functions FWHM of the corresponding peaks in the α energy spectrum provide the measure of the total width and the neutron decay width of the state. The resulting neutron branching ratio is comparable with the adopted value of real photon experiments.

SUMMARY

The primary aim of the present thesis is to explore some of the experimental techniques of nuclear reactions as indirect techniques in the study of astrophysical capture reactions. The work deals with the modeling of the astrophysical capture cross sections with relevant quantities extracted from the reaction studies. Three different astrophysical capture reactions *viz.* ^{22}Ne(p,γ)^{23}Na of NeNa cycle, ^{68}Zn(n,γ)^{69}Zn of s-process nucleosynthesis path and $\alpha\alpha$(n,γ)^{9}Be of r-process nucleosynthesis path have been studied.

Asymptotic normalization constants of ^{23}Na of bound states of ^{23}Na were estimated from finite range DWBA analysis of ^{22}Ne(^{3}He, d)^{23}Na transfer reaction data. A consistent analysis of the direct capture component of ^{22}Ne(p, γ)^{23}Na reaction was performed within the R-matrix framework, constrained with the asymptotic normalization constants of the bound states of ^{23}Na obtained from the transfer reaction calculation. The contribution of capture through the sub-threshold resonance at 8664 keV excitation in the total capture to the ground state of ^{23}Na was also determined. The observed rise in the astrophysical S-factor data for ground state capture, including the effect of capture through sub-threshold state, was reproduced nicely. The total direct capture S-factor at zero relative energy was found to be 48.8 ± 9.5 keV b, having less uncertainty corroborates with the recent measurements. The total reaction rate obtained as a function of temperature differs from the recent estimations by Ferraro et al. in the temperature window of $0.1 \leq T \leq 0.2$ GK. The difference is due to slightly higher contribution from direct plus sub-threshold capture to the ground state. However, for $T \leq 0.1$ GK, the uncertainty in the rate is comparable with the result of Ferraro et al.

In the ^{68}Zn(n,γ)^{69}Zn reaction study, the thesis attempts the extraction of nuclear level density (NLD) of ^{69}Zn experimentally. Evaporated α-spectra have been measured in coincidence with the low energy γ-rays from the purely compound nuclear reaction ^{64}Ni(^{9}Be, αn)^{68}Zn at E(^{9}Be)=30 MeV . The first chance α emission spectrum, producing ^{69}Zn, have been compared with statistical model calculation to extract the asymptotic value of NLD. Subsequently, with the asymptotic NLD, the NLD parameter at neutron separation energy of ^{69}Zn has been evaluated and used in the TALYS reaction code to calculate the ^{68}Zn(n, γ)^{69}Zn capture cross-sections. Excellent agreement with the measured (n,

γ) cross-section, does highlight the objective of direct experimental determination of the parameters of statistical model for more accurate description of astrophysical reactions.

To investigate the formation of ^{9}Be in the explosive astrophysical scenario, we studied the population of near threshold states of ^{9}Be by inelastic α scattering and their decay by emission of two α particles. As the $1/2^{+}$ state at 1.68 MeV is of particular interest as a doorway for formation of ^{9}Be, the scattered α-particles from the state in singles and in coincidence with the two decay α-s were detected. The FWHM of the corresponding peaks in the α energy spectrum provide the measure of the total width and the neutron decay width of the state. The resulting neutron branching ratio is compared with the adopted value.

Finally, the thesis includes the developmental work related to a hybrid telescope with a gas ΔE and a solid state stop E detector. Sensitivity of the detector for the detection of low energy α particles has been tested.

Chapter 1

Stellar Nucleosynthesis

1.1 Introduction

The subject 'Nuclear Astrophysics' is an overlay area of nuclear physics and astrophysics. It integrates the information like isotopic abundances, masses, half-lives, nuclear reaction cross section from nuclear physics with the models of stellar and other astrophysical environments. In the process, it answers some of the key questions of big bang nucleosynthesis, the source of energy of the stars for billions of years, the origin of chemical elements in nuclear chart and their abundances shown in Fig. 1.1, the evolution of stars from its birth to its death. Astronomy deals with the observations of the objects of the universe. To explain and validate the observations of Astronomy one needs nuclear astrophysics, one needs to study the microscopic processes taking place inside the stars. The first systematic study in this direction was presented in the seminal paper by Burbidge, Fowler and Hoyle [1].

1.2 Reactions in stars

Stars are formed initially from the Inter Stellar Medium (ISM) composed of molecular, atomic and ionized gases and also of solid particles of dust. The general idea is that

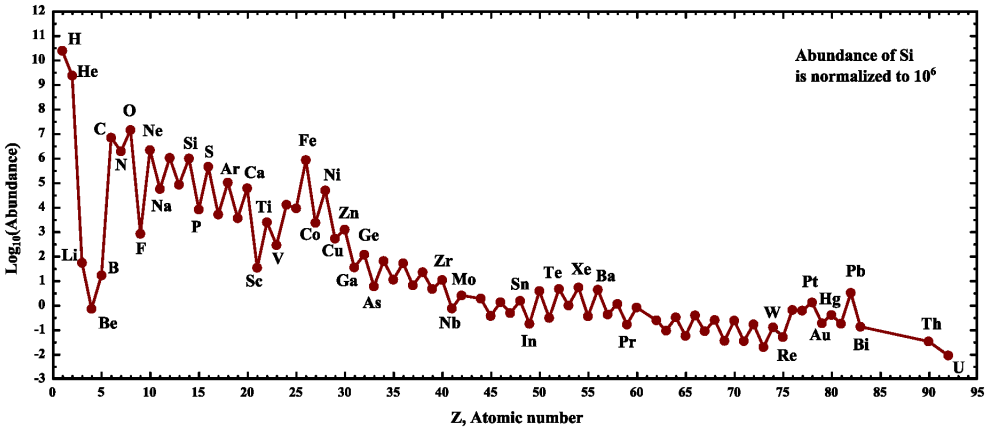

Figure 1.1: The chemical elements abundance as a function of atomic number in the solar system. [2]

star formation is initiated in the large molecular gas clouds of the ISM when certain instability conditions are reached. Under these conditions, the molecular clouds collapse under gravity and the gravitational energy released. These gravitational energy is used in raising the temperature and also in dissociating and ionizing the molecular hydrogen in the cloud. The collapsing cloud of ISM takes the shape of an accretion disk, due to angular momentum conservation, with a denser protostar at the centre. The protostar at the centre slowly grows with accretion of matter from the surrounding disk. When the temperature of the central region becomes 10^7 K, Hydrogen burning is ignited in the core region. Nuclear burning releases energy that increases the pressure in the central region. The outward thermal pressure balances the inward gravitational pressure. The collapse is eventually stopped and the star attains a hydrostatic equilibrium condition. The star is said to reach the main sequence (MS) phase. Different initial cloud masses lead to a range of main sequence stars. The main sequence stars are depicted in the Hertzsprung-Russel diagram (H-R diagram, Fig. 1.2) in an alignment that roughly follows the relation L$\propto$ R^2T^4, where R is the radius of the star, T is its surface temperature and L is the luminosity of the star.

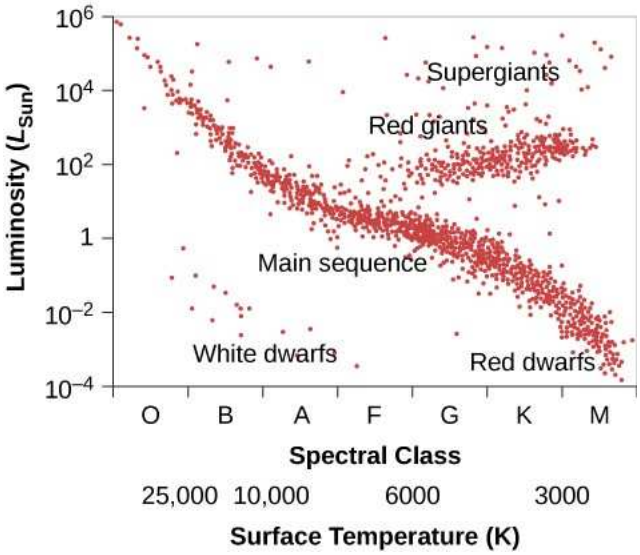

Figure 1.2: H. R diagram. [3]

1.2.1 Hydrogen burning

In stars, Hydrogen burning progresses via different sequences of nuclear capture reactions converting four hydrogens into a helium with a Q-value of 26.73 MeV. Depending on the initial mass, composition and core temperature, the H-burning can proceed through proton-proton(p-p) chain or through Carbon-Nitrogen-Oxygen(CNO) cycle. If higher core temperature is attained, synthesis heavier elements upto Aluminium can take place by H-burning processes through Neon-Sodium (NeNa) and Magnesium-Aluminium (MgAl) cycles.

p -p chains

The initial sequence of nuclear reactions generating energy in first generation stars and in stars with mass M $\leq$ 1.5 $M_\odot$, where $M_\odot$ is the mass of the Sun, is the p-p chain. The three p-p chains converting 4p $\rightarrow$ ^{4}He, are illustrated in Fig. 1.3. The second (p-p II) and third (p-p III) chains occur at higher core temperature as they involve the fusion of ^{3}He and ^{4}He. The neutrinos are produced in beta decay processes at different stages throughout the p-p chains. In fact, p-p chain starts with fusion of two protons that requires a beta decay to occur during the interaction of the two protons. The process has extremely low probability and controls the time scale of p-p chain (10^{10} yrs or 10^{18} s) of reactions. The

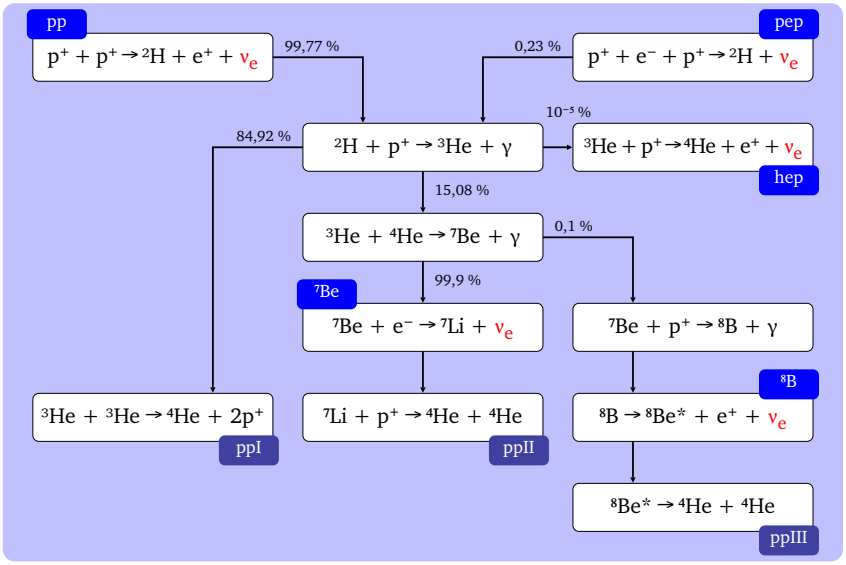

Figure 1.3: The network of p-p chain reactions. [6]

neutrinos come out from the star system with different average kinetic energy for p-pI, p-pII and p-pIII chains [5]. Thus energy retained in the star for p-pI chain is 26.19 MeV, for p-pII chain it is 25.65 MeV and for p-pIII chain its 19.75 MeV [5], respectively.

CNO cycles

In second generation stars, condensed from interstellar medium having fraction of heavy elements, hydrogen burning can also proceed through CNO cycles of reactions. CNO cycles are the dominating H-burning reactions in stars with mass M $\geq$ 1.5 $M_\odot$ and the core temperature T $\geq$ 2.0 x 10^7 K. The different branches of the cycles are shown in Fig. 1.4. Unlike the first reaction in p-p chain, CNO cycle of reactions does not require a beta decay to occur simultaneously for fusion to take place. So these are much faster and efficient processes for conversion of hydrogen and producing energy but larger Coulomb barrier affects the reaction rate. This requires higher core temperature of the more massive stars compared to that required for p-p chain.

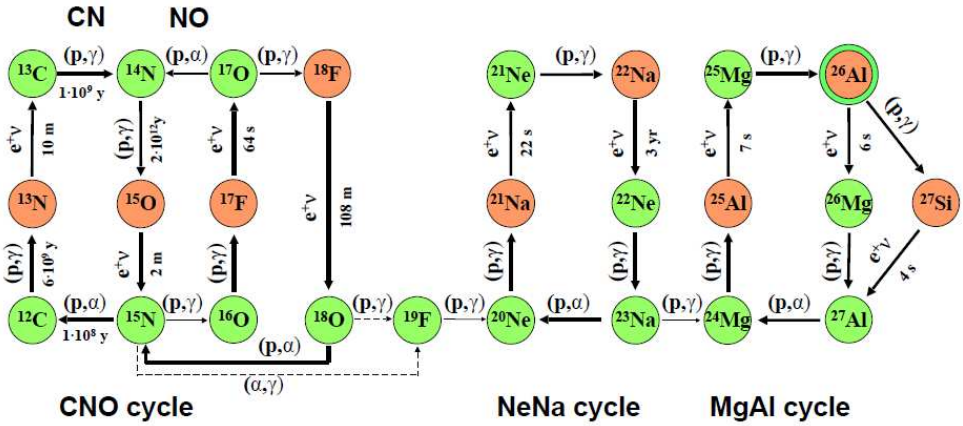

Figure 1.4: The CNO, NeNa, and MgAl cycles reaction networks.[11]

NeNa and MgAl cycles

The NeNa and MgAl cycles of hydrogen burning occur in more evolved stars, like in the Asymptotic Giant Branch (AGB) with initial masses ≥ 4 - 10$M_{\odot}$. These stars core have reached the higher burning stage and the NeNa and MgAl cycles [13] of H-burning take place in the convective outer envelope with T ~ 60-100 MK. The sequence of reactions are depicted in Fig. 1.4. The cycles are mainly responsiable for the observed anticorrelations of Al-Mg and O-Na abundances in the Galactic Globular Clusters stars [14]. The reaction ^{22}Ne(p,γ)^{23}Na of NeNa cycle is of particular interest of the present thesis because of the large uncertainty in its reaction rate [15] and its role in Nova nucleosynthesis [16].

1.2.2 Helium burning

When hydrogen as a fuel in the core of a star is depleted, thermal energy produced in the residual h-burning is not sufficient to support the outer layers of star material. The star begins to contract and core temperature rises. The hotter core radiates energy into the adjacent shells of hydrogen. As a consequence, the shell expands and also H-burning starts in the shell. Expansion increases the surface area of the star and the surface becomes cooler while the H-burning in the shells contributes to higher luminosity (energy emitted per unit time from the stellar surface) of the star. The star is then located in the "red giant" zone of the HR diagram [17].

In the stellar core, when the temperature, in the process, reaches between 1 and 2 x 10^8 K the Coulomb barrier between the two alpha particles can more easily be overcome and Helium burning will start.

Triple-α reaction

At the end of H-burning phase, there are many alpha particles as ashes. But an alpha particle does not form a bound binary system with another alpha particle, with a proton, or with a neutron as there are no stable nuclei with A = 5 or 8 nucleons. However, ^{8}Be (= $\alpha + \alpha$) is a quasi-bound resonance requiring only 92 keV energy to form it and having a lifetime of $\sim 10^{-}16$ s to decay back to $\alpha + \alpha$. In the hot core of the star the two states form an equilibrium with a small concentration of ^{8}Be (N(^{8}Be)/N(α) $\backsim 10^{-10}$). This small concentration of ^{8}Be at $T_9 = 0.3$ and density of 10^5 g/cm^3, typical of He-burning in stellar core, still has some probability of capturing a third alpha particle to form ^{12}C nucleus.

The non-resonant direct triple-α reaction does not produce enough carbon to explain the observed abundance of the nucleus. The key point is a narrow 0^+ resonance in the ^{8}Be+ α = ^{12}C* system that enhances the triple-α fusion reaction. The resonance is called the Hoyle resonance, named after Fred Hoyle who predicted it in 1954 [7] on the basis that this is the only way to produce the measured quantities of ^{12}C in the Universe. The Hoyle resonance was, subsequently corroborated by experiments, at 287 keV (E_{ex} = 7.654 MeV) above the 3α breakup threshold with a narrow width of 8.3 eV [8]. The state can decay back to 3 α, or with a small branching ratio for gamma emission to the 4.44 MeV state of ^{12}C, or via direct e^+ - e^- decay to 0^+ ground state.

Other alpha capture reactions

After ^{12}C formation through triple-α process, burning proceeds through the capture reaction chain ^{12}C(α, γ)^{16}O(α, γ)^{20}Ne. The rate of ^{12}C(α, γ)^{16}O reaction relative to the 3α capture process, determines the C/O ration in the post-He burning phase, which, in turn, affects the abundances of heavier elements produced in subsequent phases. The C/O ratio is crucial in determining whether the final remnant of massive star, following a supernova

explosion, is a neutron star or a black hole [18]. The 3α reaction is comparatively well known but the $^{12}C(\alpha, \gamma)^{16}O$ reaction is still the most important source of uncertainty in stabilizing the C/O ratio. Further α capture reactions producing ^{20}Ne and ^{24}Mg occur with much less probability because of the hidrance due to higher Coulomb barriers. Thus the net result due He-burning is a star core with mostly ^{12}C and ^{16}O and a small amount of ^{20}Ne and ^{24}Mg.

Neutron producing alpha capture reactions

The reactions of the type (α, n) are the main sources of neutrons for nucleosynthesis of elements beyond the iron peak in the abundance curve through neutron capture reactions. Some of the reactions like $^{9}Be(\alpha, n)^{12}C$, $^{13}C(\alpha, n)^{16}O$ and $^{22}Ne(\alpha, n)^{25}Mg$ are the primary neutron sources for the slow capture processes (s-process) in massive stars. While $^{13}C(\alpha, n)^{16}O$ reaction (Q = 2.21 MeV) is mainly activated during the post CNO H-barning phase, the reaction $^{22}Ne(\alpha, n)^{25}Mg$ with low Q = 0.48 MeV occur in late He-burning stages.

1.2.3 Advanced Burning

Once He-burning stops, the stellar core with mostly C and O stars to contract under gravity and the core temperature starts to rise. If the mass of the star exceeds $8M_{\odot}$, as the core temperature becomes $T_9 = 0.8$ carbon burning is ignited. The fusion of $^{12}C+^{12}C$ produces ^{20}Ne, ^{23}Na and ^{23}Mg nuclei. After C-burning, under gravitational contraction core temperature and density rises again. When the density becomes about 10^7 g/cm^3 and T~1.4, Neon burning is initiated in massive stars. Ne-burning yields primarily ^{16}O and ^{24}Mg.

When a star with mass M ≥ 10-11 $M_{\odot}$ achieves a core density of a few times 10^7 g/cm^3 and a temperature $T_9 = 2$, Oxygen burning can start. O-burning with the fusion of $^{16}O+^{16}O$ results into ^{28}Si, $^{30,31}P$, ^{31}S and other nuclei. Following the O-burning, the core of the star can further contract increasing the density to 10^8 g/cm^3 and T_9=3.5 when the photodisintegration of a ^{28}Si nucleus, from previous burning, into seven α particles occurs [18]. The resulting α particles are captured by ^{28}Si to form ^{32}S and subsequently other higher mass

nuclei. A nuclear statistical equilibrium is set in involving protons, neutrons and aplha particles and gradually Fe-Ni peak nuclei are reached.

Massive stars undergo all stages of burning till the iron group of nuclei with A=56 are produced in the core. The outer envelope of the core consists of different shells of burning with H-burning shell being the outermost. Moving inward, the concentric shells are composed of helium, carbon, neon, oxygen and silicon burning regions, respectively. This is the so called 'onion-like' structure of massive stars. When the core grows further because of high temperature and density, reactions like nuclear photodisintegration and neutronization take palce in the core releasing huge amount of energy in the process.

1.2.4 Synthesis of heavy nuclei

Synthesis of maxium elements heavier than Fe occurs mainly via s- and r-process neutron capture reactions. The heavy ion fusion reactions can not produce elements beyond ^{56}Fe, because the reactions are of negative Q-value and energy is not gained any more in these reactions. The neutron capture is the alternative for producing heavier nuclei. Cross section of neutron capture rises at low energies, as 1/v for relative velocity v, and the coefficient of 1/v increases for heavier nuclei.

s-process neutron capture reactions

s-process corresponds slow neutron capture process where the neutron capture time is longer than the β-decay half life of the nucleus, i.e., $t_{capt} \gg t_{\beta}$ and is activated in low neutron density environment ($\rho \approx 10^7$ - 10^{10} g/cm^3) [19] of astrophysical sites. The s-process progresses with (n, γ) capture on stable nuclei, producing neutron-rich isotopes that are a few nucleons away from the β-stability line. When a radioactive species is populated in the sequence that β-decays by electron emission to the next element with the same mass, a branching point is said to have reached. Several branching points are shown in Fig. 1.5. In red giant pahse with neutron flux of 10^{20} m^{-2}s^{-1}, nuclei are built up slowly through s-process neutron capture.

Figure 1.5: The s-process nucleosynthesis path.

r-process neutron capture reactions

Now r-process nucleosynthesis corresponds to rapid neutron capture that occurs when the stellar environment has very large density of neutrons ($\rho \gg 10^{20}$ cm^{-3}) [20]. It is widely believed that in core collapse supernovae [21], neutron star mergers [22] huge number of neutrons are produced, at least for a few seconds, leading to rapid capture sequences that extend the horizontal isotopic chains to the right in the nuclear chart well beyond the first radioactive isotopes (the shaded region in Fig. 1.6). Neutrons are progressively captured by (n,γ) reactions at a rate much higher than the β-decay rate. The process continues until the production of extremely neutron-rich isotopes is limited by the increased probability of (γ, n) photo-disintigration reaction. The n $\Leftrightarrow$ γ balance point between capture and the disintegration defines the location of the r-process path on the Segre chart.

The synthesis of heavy nuclides via explosive nucleosynthesis at a type II supernova site has connection with the rate of ^{9}Be production [24]. Before the r-process, the α-process [21] is dictated by charged-particle reactions at the time of the rebounding shock wave, generated by collapse of the iron-group core of the massive stars. The neutrino driven wind from the collapsing core blows off the gaseous envelope of the star. As the slightly neutron rich outer layer expands off and cools, a small number of seed nuclei are formed through the alpha induced reactions. Heavier nuclei are formed through the capture of available free neutron by the seed nuclei. In this stage of nucleosynthesis a reaction path

Figure 1.6: The r-process nucleosynthesis path.

is needed to bridge the stability gaps at A = 5 and A = 8. The most efficient path is α + $\alpha \rightarrow {}^{8}$Be and ^{8}Be(n, γ)^{9}Be, followed by ^{9}Be + $\alpha \rightarrow {}^{12}$C + n [23]. As cooling continues this reaction sequence largely establishes the neutron-to-seed-nucleus ratio to which the subsequent r-process is very sensitive [25]. Because the r-process abundance predictions in stellar models are extremely sensitive to the $\alpha(\alpha$n,$\gamma)^{9}$Be rate [24, 26, 27], establishing a precise rate for the formation of ^{9}Be via the $\alpha(\alpha$n,$\gamma)^{9}$Be reaction is required for accurately modeling nucleosynthesis during supernovae explosion.

1.3 Input for nucleosynthesis modeling

Understanding the abundance of chemical elements and the energy generation in nucleosynthesis process of a particular astrophysical environment requires calculation of nuclear reaction networks for different cycles including all the relevant nuclear reactions. The reaction network equation is basically an ordinary coupled differential equation with large systems of nuclear reaction rates [5]. So reaction rate (i.e, number of reactions per projectile-target pair) is one of the inputs of the stars network modeling. The reaction rates of different astrophysically important nuclear reactions, described in the nest chapter, are estimated from experiments in the laboratory.

Chapter 2

Experimental Techniques In Nuclear Astrophysics

2.1 Stellar Reaction Rate

In understanding the nucleosynthesis of the elements in stars, one of the most important quantities is the reaction rate. It is required to determined the rate as a function of stellar temperature T. The quantity reaction rate is defined as

$$r_{aX} = n_a n_X < \sigma v > (1 + \delta_{aX})^{-1} \tag{2.1}$$

where n_a (n_X) are the number densities of interacting particles a and X in the stellar environment. The term $(1 + \delta_{aX})^{-1}$ is to compensate the condition of identical particles. Its determination requires the knowledge of the cross section as a function energy, σ(E), of the specific nuclear reaction. In stellar site, the reaction rate per particle pair is calculated as [17]

$$< \sigma\upsilon >= (\frac{8}{\pi\mu})^{1/2} \frac{1}{(kT)^{3/2}} \int_0^\infty \sigma(E) E \exp(-\frac{E}{kT}) dE \tag{2.2}$$

where μ is the reduced mass of the two colliding nuclear particles, k is the Boltzmann's constant. The exponential factor in the integral comes from the distribution of velocities of the particles in the hot stellar interior. Taking the extremely hot stellar interior as a

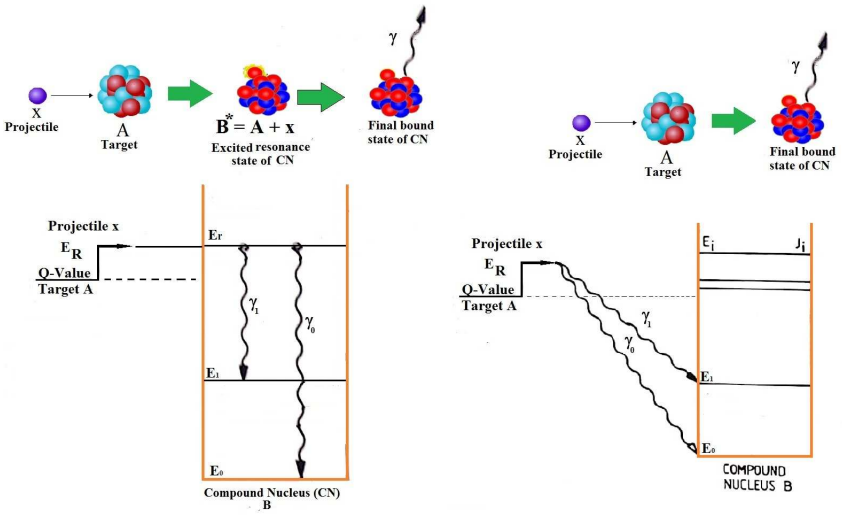

Figure 2.1: The pictorial representation of resonance and non-resonance capture reaction.

non-relativistic, classical gas system. the velocity distribution is described by Maxwell-Boltzmann distribution. It is important to obtain analytic expression for rate in terms of temperature T. The mathematical approach used in arriving at such an analytic expression is determined by the energy dependence of the cross section, σ(E), the experimentally measured quantity. The energy dependence of the cross section reflects the reaction mechanism involved in the process. Resonance and non-resonance processes along with the interference effect of the reaction mechanisms are mainly observed in capture reaction experiments.

2.1.1 Non-resonant Capture

Reaction taking the target-projectile system from the entrance channel (scattering state) to the exit channel (bound state) without forming any intermediate compound nucleus is described as a non-resonant capture reaction. A schematic diagram representing the process is shown in Fig. 2.1. The time scale of this type of reaction is around ($\approx 10^{-21}$sec), more like the direct nuclear reaction.

The process is entirely electromagnetic and is similar to the well known bremsstrahlung process [82]. The cross section for γ-ray emission in direct capture is describe by a single matrix element,

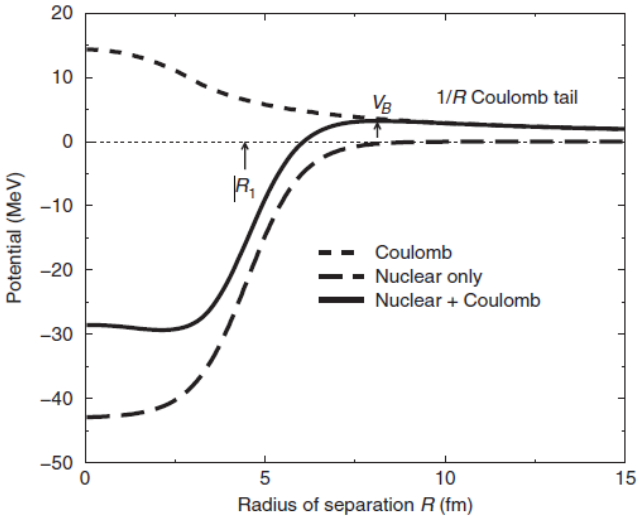

Figure 2.2: The potential energy curves between two charged nuclei.

$$\sigma_\gamma \propto | < B|M_\lambda|A + x > |^2 \tag{2.3}$$

Where A + x is the initial state from which the system is going to the final bound states of B nucleus via electromagnetic operator M_λ transition. In this single step transition process a γ-ray with energy E_γ = E + Q - E_i is emitted.

Charged particle induced process

A capture reaction between two charged nuclei, is hindered by the long range Coulomb repulsive force of the particles, which dominates the interaction region at larger separation with respect to the nuclear interaction range between them. The interaction potential energy pattern between them as a function of radial distance, r, is shown in Fig. 2.2.

At low energies, the tunneling factor from the penetration of Coulomb barrier of the two charged nuclei, will dominate the cross-section in all astrophysical scenarios, and will very often be the limiting factor for nuclear reactions to occur. At low energy the cross-section σ(E) can be factorize as

$$\sigma(E) = \frac{1}{E}\exp(-2\pi\eta)S(E) \tag{2.4}$$

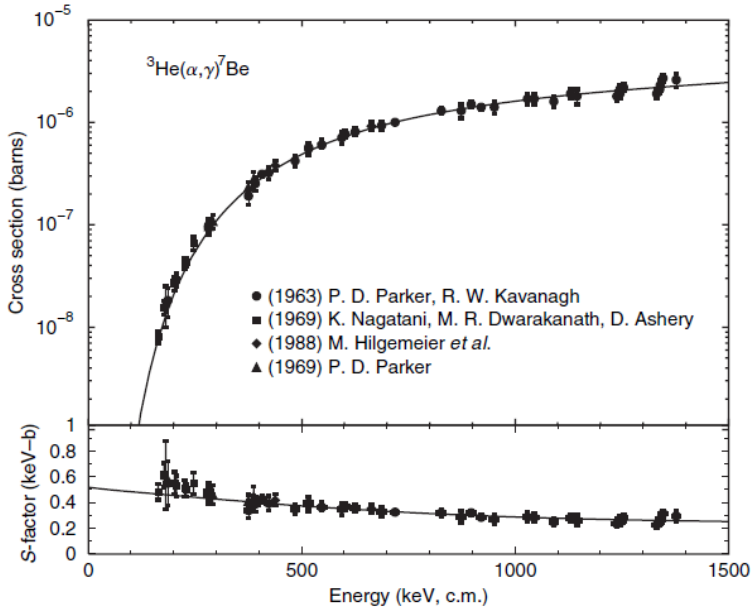

Figure 2.3: The variation of cross section and S-factor for $\alpha(^3\text{He}, \gamma)^7\text{Be}$ non-resonance capture reaction.

where $\frac{1}{E}$ is the geometrical factor related to the wavelength of the incoming particle, $\exp(-2\pi\eta)$ is tunneling factor through the Coulomb barrier. η is the Sommerfeld parameter related to product of charges and relative energy of interacting nuclei. S(E) is the astrophysical S-factor, slowly varying function with energy, depends on structure of nuclei and the reaction mechanism. In Fig. 2.3 an example of the cross-section for the α capture on ^{3}He to synthesize ^{7}Be, which is a direct capture process, has been presented. The reaction cross section (upper panel) falls off rapidly as the energy decreases, whereas the S-factor (lower panel) is nearly constant.

A. Gamow Window

One can estimate the typical energies at which nuclear burning takes place inside the stars at a particular temperature T. This effective energy region is known as the Gamow window, at T and is depicted in Fig. 2.4. Now over a narrow energy window for burning, the S-factor can be assumed to be constant and can be taken out of the integral. Hence, the energy at which the integral has its maximum, it is known as the Gamow peak.

$$E_0 = 1.22(Z_1^2 Z_2^2 \mu T_6^2)^{1/3} \tag{2.5}$$

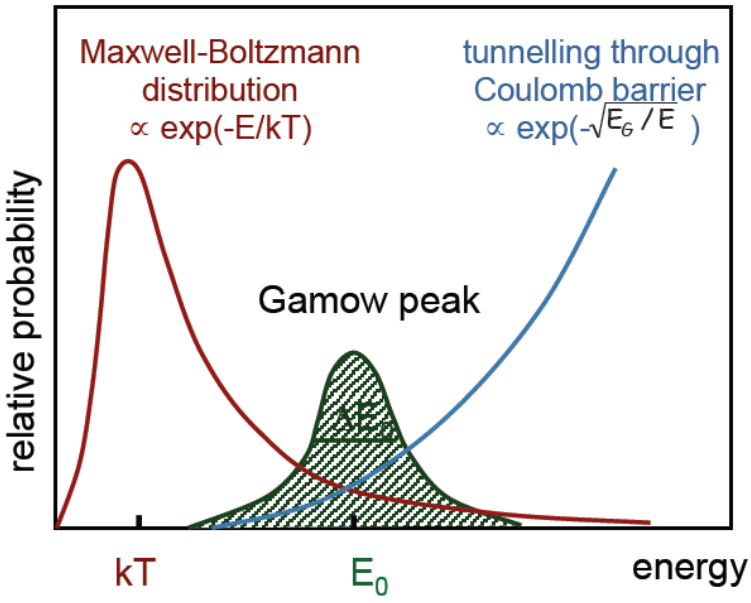

Figure 2.4: The Gamow window.

The effective width of the Gamow peak can be estimated by approximating the overlap region of the two distribution as a Gaussian distribution of width and the maximum [17] at E_0. By setting the second derivative of this overlap integrand at E_0 equal to the second derivative of a Gaussian expression around E = E_0 we find:

$$\Delta = 0.749(Z_1^2 Z_2^2 \mu T_6^5)^{1/6} keV \tag{2.6}$$

The Gamow window is the most relevant astrophysical energy region where a nuclear reaction is most likely to proceed depending upon the temperature of the environment. This estimation relies upon the assumption that the S-factor, containing all required information in the cross-section, is constant across the Gamow Window. This, of course, is rarely the case and more accurate calculations had been performed for many reactions of interest relevant to different burning regions in Ref.[69].

Neutron-induced non-resonant reactions

The neutron induced capture reactions, (n,γ), are important for s- and r- process nucleosynthesis. The charge less neutrons do not face the Coulomb barrier and are quickly ther-

malized (time scale $\sim 10^{-11}$ s) in stars when produced in astrophysical reactions. Their velocity distribution can also followed by the Maxwell-Boltzmann distribution. At stellar environments the nutron-induced reactions are occurs at the maximum of the Maxwell-Boltzmann distribution, at E = kT. The neutron capture cross section at low energies for l th partial wave is given as

$$\sigma_l \sim (\frac{1}{v^2})\Gamma_l, \tag{2.7}$$

where v is the relative velocity between neutron and the target. Γ_l is the partial width, can be express as

$$\Gamma_l \sim (vR)^{2l+1} \sim E^{l+1/2}, \tag{2.8}$$

where l is the orbital angular momentum and R be the channel radius, respectively. Accordingly, the reaction rate can be written as

$$< \sigma v > \sim E^{l+1/2} \exp(-\frac{E}{kT}) \tag{2.9}$$

The relevant energy of the neutron-induced capture reaction in the stellar environments is defined by the $E^{l+1/2}exp(-\frac{E}{kT})$ function. As influence of the centrifugal barrier on the cross-sections are smaller than the Coulomb barrier, the effective astrophysical energy window can be controlled by the Maxwell-Boltzmann distribution.

Non-resonant form of reaction rate

If the astrophysical S-factor is fairly constant over the Gamow energy window does not vary much at other energies, then we can set S(E) = $S(E_0)$ and it can be taken out of the integral. Completing the integration over the Gaussian shape of the energy window, one

gets the non-resonant reaction rate per interacting particle pair at temperature T as [17]

$$< \sigma v >= \frac{2}{\mu}^{1/2} \frac{\Delta}{(kT)^{3/2}} S(E_0) \exp(\frac{-3E_0}{kT}) \tag{2.10}$$

where μ is the reduced mass. This expression is the zeroth order expression for reaction rate and can be refined for the case of slow energy dependence of S-factor. It also describes the dependence of reaction rate on temperature and charges of the interacting particles.

2.1.2 Resonant capture

Instead of proceeding directly from the entrance channel into the exit channel, the target and projectile system in a nuclear reaction can form a compound nucleus in an intermediate step if an energetically favorable state exists in that nucleus.The positive energy resonant state of the composite nucleus then decays by emission of p, n, α particle or emission by photons. The later process is defined as resonance capture. The resonance capture is graphically described in Fig. 2.1, where E is the beam energy in the center of mass frame. When E matches with resonance energy (= E_r - Q, E_r being the excitation energy) of a state above the threshold given by the Q value, the resonance will occur. The probability of resonance capture is now additionally hindered by the centrifugal barrier dependent upon the relative spins of the state and the reactants.

$$V_{cf} = \frac{l(l+1)h^2}{2\mu r^2} \tag{2.11}$$

Here, l is the angular momentum transfer required to populate the state of spin J such that standard vector addition applies to the relationship $J = J_a + J_X + l$. The lower l states are more favorably accessible. When a resonance is populated, there can be a significant enhancement of the reaction cross-section with sharp variation of the reaction cross section. A decaying resonance state has an energy distribution given by Breit- Wigner distribution. The energy variations of nuclear cross section for formation of the state with resonance energy E_R through a channel j (a+X) and its decay into channel k (b+Y) is written as

$$\sigma(E) = \sigma_{max}\frac{\Gamma_j\Gamma_k}{(E - E_R)^2 + (\Gamma/2)^2} \tag{2.12}$$

where $\Gamma_j(\Gamma_k)$ is the partial width for formation (decay) of the resonance state and $\Gamma = \Gamma_j + \Gamma_k + ...$ is the total width related to mean life time (τ) of the state as $\Gamma = \frac{\hbar}{\tau}$. The notation σ_m here represents the product

$$\sigma_m = \pi\bar{\lambda}^2\omega(1 + \delta_{aX}) \tag{2.13}$$

with statistical spin factor $\omega = \frac{(2J+1)}{(2J_a+1)(2J_X+1)}$. The factor $(1+\delta_{aX})$ is to account for the increase in the cross section for identical particles.

This is the Breit-Wigner equation for an isolated resonance. The widths, the partial and total, are all energy dependent quantities. When there are only two channels j and k such that $\Gamma = \Gamma_j + \Gamma_k$, then the reaction cross section σ_{jk} is maximum for the condition $\Gamma_j = \Gamma_k = \Gamma/2$ and $(\sigma_{jk})_{max} = \sigma_m$. Under this condition the reaction cross section σ_{jk} is equal to the elastic cross section σjj.

Resonant form of the reaction rate

If the Breit-Wigner expression for an isolated resonance cross section is inserted in Eq.2.1 and it is assumed that the resonance is sufficiently narrow so that the energy dependent terms in the integrand don not vary much over the width of the resonance, then the resonance form of the reaction rate can be written as

$$< \sigma v >= (\frac{2\pi}{\mu kT})^{3/2}\hbar^2\omega\frac{\Gamma_j\Gamma_k}{\Gamma}\exp(\frac{-E_R}{kT}) \tag{2.14}$$

The quantity $\omega\frac{\Gamma_j\Gamma_k}{\Gamma} = \omega\gamma$ is the strength of resorance of the reaction and is an experimentally measurable quantity. For a narrow resonance case the reaction rate can be estimated from the experimental values of resonance energy, width and the strength.

The reaction rates for both the non-resonant and resonant cases need to be modified by the electron screening effect. The effect is incorporated by multiplying the rate by a factor

f. The factor f is nearly equal to unity for typical stellar densities and compositions but has a strong effect at higher densities.

2.2 Measurement methods in Nuclear Astrophysics

In general, the two different experimental approaches for relevant nuclear astrophysical cross section measurement are - *i) the direct method, and ii) the indirect method*. While the direct measurement, if possible, is always preferable and is the first priority, the indirect method of measurement provides realistic alternative where direct measurement is impossible to carry out. In the next subsection we will discuss in brief the difficulties related to direct measurement and then go over to the indirect techniques of measurement in nuclear astrophysics that is the topic of present thesis.

2.2.1 Direct method

The direct measurements in nuclear astrophysics imply the measurements of exactly the reactions at energies with which they occur in astrophysical environments. The two most important challenges in such measurements are the extremely low cross sections of the reactions at relevant energies and the involvement of unstable radioactive nuclei in many reactions of interest.

Direct measurement of low cross sections at low energies involve the issue of stability and background reduction. The three major sourcees of backgrounds in Earth based experiments are - cosmic rays, natural radioactivity, and target-beam induced backgrounds. Active shielding can reduce the cosmic ray induced background. But carrying out the experiments in underground laboratories can improve the backgrounds due to cosmic rays as well due to natural radioactivity. At low energies, direct measurement cross sections are also affected by electron screening [17]. Often measurements are carried out at higher energies and then extrapolated to required low energies using models. However, the extrapolations may often involve significant uncertainties.

These difficulties combined lead to indirect techniques of measurements in nuclear astrophysics. Applications of some of these indirect techniques constitute the structure of this thesis work.

2.2.2 Indirect Method

Indirect techniques have been developed with the aim to bypass the difficulties faced in direct measurements of astrophysical reactions. The indirect method is adopted to extract the relevant information of associated nuclei that are involved in astrophysical reactions to determine the cross sections and/or reaction rates of the astrophysical processes. The primary advantage of the techniques is that the required reactions can be performed in the laboratory at much higher energies where the cross sections of the processes are high.

The general scheme followed in indirect methods is to perform a suitable nuclear reaction measurement in the laboratory and then compare with theoretical model to extract nuclear information, typically nuclear structure information like spectroscopic factors. Then to use the extracted nuclear information in estimating nuclear astrophysics data like cross sections, astrophysical S-factors or reaction rates. The important aspect of extraction of nuclear information for nuclear astrophysics through an indirect method is the model independence of the quantity, as much as possible, and with uncertainty, as low as possible. Any deviation from this requirement can introduce extremely large error in the astrophysical data. Also the results from indirect measurements should corroborate with that from direct measurements wherever available.

In the following subsections we will introduce the different indirect techniques that are adopted in obtaining the astrophysical information for different mass regions of nuclei. The discussion will be restricted to synthesis of nuclei in two nuclear mass regions that are of interest of the present thesis.

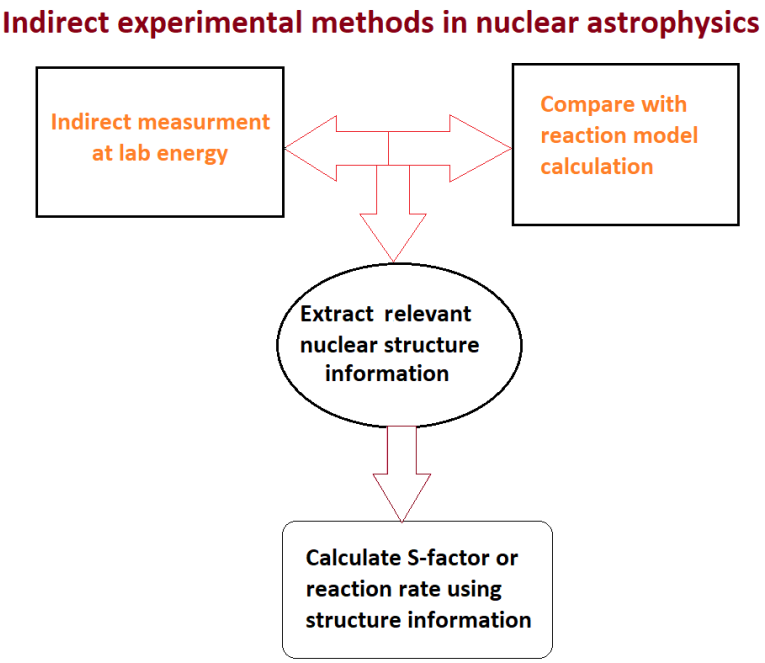

Figure 2.5: The schematic representation of indirect method for nuclear astrophysics.

Indirect method for $A \leq 25$

In this mass region the energies of the thermonuclear reactions correspond to a range of excitation energies in the compound nucleus where the levels of interest are discrete in nature, *i.e.*, the level spacing (D) is larger than the widths (Γ) of the states. Indirect methods generally used for nuclei of this mass region can be classified as follows

A. The Asymptotic Normalization constant (bound states)

B. Spectroscopy of resonances (unbound states)

C. Inelastic Spectroscopy

D. The Trojan Horse Method

E. The Coulomb Dissociation(CD) method

A. The Asymptotic Normalization constant (bound states)

Direct capture reaction in astrophysical scenario occurs at very low energy and the cross section of the reaction involves the square modulus of the two body nuclear overlap function at large radial separation. The nuclear overlap function is defined as the projection of

the many body wave function of the composite nucleus, formed after the capture, onto the product of the ground state wave functions of the target and the projectile. The tail of the overlap function is controlled by the Coulomb interaction. The asymptotic behaviour of the overlap function describing the capture process is given by a known Whittaker function, based on the binding energy of the final state, and a normalization constant. This normalization constant is known as the Asymptotic Normalization Coefficient or the ANC [28, 29, 30]. Transfer or break up reaction experiments can also measure the Asymptotic Normalization Coefficients.

(i) ANCs from peripheral transfer reactions

In transfer reaction, the particle extracted from the projectile and transferred to the target to form a bound state that can be the final state in a direct capture reaction [31, 55]. Thus the two reactions processes share the same overlap function. The ANC associated with the nuclear overlap function, therefore, can be extracted from the peripheral transfer reaction experiments at energies near the Coulomb barrier. At above barrier energy, the transfer reaction cross-sections are of much larger orders in magnitude than the radiative direct capture reaction at astrophysical relevant energy. The peripheral condition can be achieved by restricting the measurment to forward angles where Coulomb interaction is dominating. In the sub-Coulomb barrier energy, the condition of peripherality is automatically satisfied. Though the cross section is much lower than above barrier energy, it is still significantly larger than the direct capture reaction at astrophysical energies.

The overlap of transfer reaction and radiative capture reaction was first demonstrated by C. Rolfs [97]. Subsequently, the method has been used extensively in heavy ion induced one nucleon transfer reactions in the Refs. [34, 35, 37]. The details of theoretical modeling of the technique are given in Refs. [38, 30, 39, 40, 41, 42, 43, 44, 45].

The ANC technique has also been applied to α-transfer reactions treating the transfer as a single particle transfer, both at sub-Coulomb energies [109, 47, 48] and above Coulomb barrier energies [49, 50]. The particular interest in alpha transfer reaction came from the investigation of the capture reaction $^{12}C(\alpha,\gamma)^{16}O$.

The relevant steps to extract the ANCs from transfer reaction cross section will be given

in the Chapter III of the present thesis describing our work on the reaction ^{22}Ne$(p,\gamma)^{23}$Na.

(ii) ANC from breakup reaction

One nucleon removal through breakup of loosely bound light projectile in a collision at energies above the respective Fermi energy can also provide the ANC of the single particle configuration in the ground state of the nucleus [29]. It has been demonstrated that with proper choice of the target, for large range of energies breakup of loosely bound projectiles are peripheral in nature [52]. As the breakup experiment provides the momentum distribution of the removed single nucleon in the ground state of the projectile, the ANC of the configuration and hence, the corresponding astrophysical S-factor of non-resonant capture can be extracted from such measurement. The technique has been applied in detail in the Refs. [53, 54]. However, for the extraction of astrophysical information with acceptable uncertainty, reliable modeling, which reproduces the experimental breakup

B. Spectroscopy of resonances (unbound states)

Apart from the direct component in astrophysical capture process, contribution can come from capture to the resonance states in the continuum of the composite nucleus. The compound resonant state can decay to lower bound states of the composite nucleus by γ-emission or it can also cool down by emitting decay particles. In case of near threshold resonance states γ-decay is the dominant colling down channel while for states at higher excitation energies particle decay becomes dominant [17]. The reaction rate for resonant capture is given above in Eq, 2.14. Estimating the rate requires the knowledge of the resonance strength $\omega\gamma$ or the branching ratios involved in $\omega\gamma$, the spin of the state (J) and the resonance energy (E_R).

Different indirect experimental probes are used to obtain the relevant astrophysical quantities. We list below the different techniques highlighting the quantities that can be extracted from them without going into any detail description.

(i) **Transfer reaction to unbound state** $\rightarrow$ spin(J), parity, particle decay width (Γ_p) and resonance energy (E_r) of resonance states. [55].

We have used this technique in our investigation of the resonance states in ^{23}Na from ^{22}Ne(p,γ) capture reaction. The necessary relations related to the extraction of the parti-

cle decay width of the resonance are given in Chap III.

(ii) **γ-ray spectroscopy** $\rightarrow$ spin(J), parity, particle decay width (Γ_γ), branching ratio, lifetime of a state and resonance energy (E_r) [29].

(iii) **Beta-delayed particle emission** $\rightarrow$ the resonance energy, the spins and parity of the states involved and probability of the decay branching of different modes of decay. The scheme in this particular technique is to populate the required resonance state above the particle threshold of the compound nucleus through suitable *beta*-decay process and then look for the particle and γ decays of the state populated in coincidence with the β-particle. The method quite effective in case of radioactive nuclei important in astrophysical scenario.

(iv)**Thick Target Inverse Kinematics(TTIK)** $\rightarrow$ the resonance energy, the particle and γ-decay widths of resorance states [29].

C. Inelastic Spectroscopy

The inelastic scattering cross section from ground state to an exited state of a nucleus depends on the intrinsic structure of the nucleus and the cross section of the process depends on the reduced transition probability $B(i \rightarrow f)$ between initial state i and final state f. For one step transition inelastic scatting can be treated within DWBA approaches just like transfer reaction. The normalization of the predicted DWBA cross section to the experimental cross section yields the transition strength and the shape of the angular distribution again provides information on the angular momentum of the state [3]. Carefully designed inelastic scattering experiments exciting unbound states above the threshold and then a coincident detection of decay particles from the state can provide information about the branching ratio, derived from suitable inelastic experiments populating near threshold states or sub-threshold states in the nucleus of interest can be used in estimating the data, like the resonance strengths, to be used to obtain the reaction rate contributions of the states.

In the thesis, a study of ^{9}Be(α, α') ^{9}Be* $\rightarrow$ ^{8}Be + n reaction has been presented investigating the $1/2^{+}$ (1.68 MeV) state as the entry level of formation of ^{9}Be nucleus.

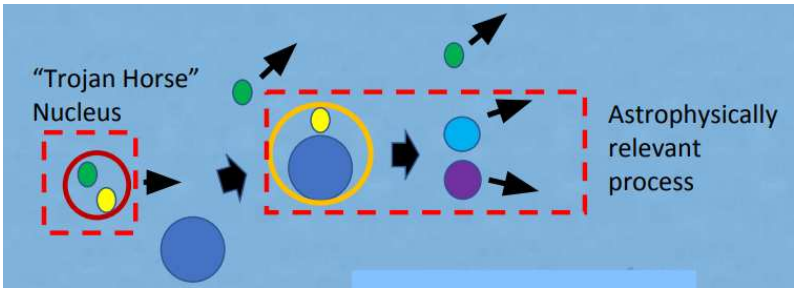

Figure 2.6: The THM reaction.

D. The Trojan Horse Method

Determination of the astrophysical S-factor for low energy capture reaction the Trojan Horse Method (THM) is a powerful indirect technique. The technique is said to be more 'direct' amongst the 'indirect' methods. The THM was first conceived as an indirect method in Ref. [39] and later modified and applied to different nuclear astrophysical reactions in Refs. [56, 57, 58, 59, 60] The theoretical modeling of THM was further refined and developed in Refs. [61, 62].

The THM works under the kinematic condition of quasi-free mechanism. In THM, the Trojan Horse nucleus a, having a strong 2-body cluster structure ($a = s + x$), moves with an energy higher than the Coulomb barrier relative to the target nucleus A. Thus overcoming the barrier, the TH nucleus a breaks up into its fragments s and x in the mutual nuclear field with much higher probability. Under the chosen kinematic condition, the fragment x moves slowly relative to the traget A and the fragment s acts as a spectator. The $A - x$ subsystem, moving at a low relative energy as in the stellar environment, forms a compound nucleus that subsequently decays to $C+c$ channel. The mechanism simulates the astrophysical reaction $A + x \rightarrow C + c$. Performing exclusive measurement, one can connect the triple differential cross section of the 3-body final state, comprising of $C+c+s$, to the cross section of the 2-body reaction in the sub-system $A+x \rightarrow C+c$ of astrophysical reaction.

The main accomplishment of the THM reaction are:

• The cross-section can be achieved in a wide energy window and upto very lower energy. So One can obtain the exact trend of S-factor near zero energy, locations and widths of very low energy resorances or effect of sub-threshold resorances when another methods

are fails [58].

• This method provides the relevant astrophysical cross section free of the effect of electron screening. This is an advantage of THM mechanism as the reaction occurs within the Coulomb barrier between the fully stripped nuclei.

E. Coulomb Dissociation(CD) method

In the Coulomb dissociation process [64], the projectile A is dissociated by the virtual photon field of a high-Z target Z_T into a binary fragments of $B + c$. The energy of the virtual photons should be greater than the separation energy S_c of A into the channel $B+c$. The measured double differential breakup cross section can be related to the dissociation cross section along with the number of virtual photons and virtual photon energy

$$\frac{d\sigma_{dis}(E_\lambda)}{dE} = E_\gamma \left(\frac{dn_{E\lambda}}{d\Omega}\right)^{-1} \frac{d^2\sigma_{B,c}}{dEd\Omega} \tag{2.15}$$

The process is equivalent to the photodisintegration of nucleus A, i.e., $A + \gamma \rightarrow B + c$. Using the principle of detailed balance, the experimentally determined dissociation cross section can be related to the cross section of capture reaction $B + c \rightarrow A + \gamma$ as shown below

$$\frac{d\sigma}{dE_\gamma} = \frac{2(2J_A + 1)}{(2J_B + 1)(2J_c + 1)} \frac{k_\gamma^2}{k_{Bc}^2} \frac{d\sigma_{dis}}{dE} \tag{2.16}$$

The excitation function of the capture cross section, $\sigma(E)$ or the astrophysical S-factor, $S(E)$ can be obtained by varying the virtual photon energy as $E = E_\gamma - S_p$.

The method has its own shortcomings. To obtain a good break up cross section, the number of virtual photons and hence the experiment is to be carried out at higher energies. But then the cross sections are to be measured for large impact parameter to disentangle the purely Coulomb induced dissociation. However, the advantage of the method is that $\sigma(E$ or $S(E)$ of radiative capture process can be obtained for very low energy, $E \sim 0$. The method is also useful at relativistic energies that allow to use of thick targets.

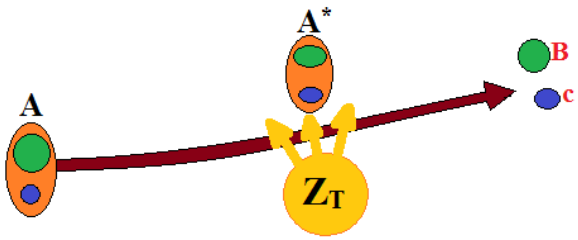

Figure 2.7: The coulomb dissociation technique.

Indirect method for $A \geq 50$

Capture reaction can occur in an excitation region above the particle threshold($E_x \geq S_n$) where the energy levels overlap with each other because the level spacing (D) becomes less than the widths of the levels (Γ) i.e.,(D$\leq$ Γ). The compound nucleus is then populated in the continuum. So the description of capture reactions relies on statistical model calculations to determine the astrophysical reaction rate. Capture of neutrons on targets in the mass region $A \geq 50$ populate levels in the continuum region.

The Hauser-Feshbach model is used to calculate the reaction cross section. The model requires the optical model potentials (OMP) for particle transmission coefficients, nuclear level density (NLD) parameter and gamma ray strength function for extraction of γ-ray transmission coefficients [66]. The nuclear level densities and gamma-ray strength functions are the key elements for Hauser-Feshbach statistical model calculations to predict the reaction cross sections. Constraining these parameters through indirect experiments are made at different energies available in the nuclear physics laboratories. Indirect methods usually adopted in such cases are

A. Oslo method to estimate nuclear level density (NLD) and gamma ray strength function

B. Surrogate reaction to estimate γ-decay branching probability.

C. Particle evaporation technique to estimate nuclear level density (NLD)

A. Oslo method

The simultaneous extraction of the level density and γ-ray transmission coefficient from a set of particle-γ coincidence data is the main technique in Oslo method [83, 84, 85, 86].

The particle gating has been used to identify the excitation energy of the residue. Final particle gated by primary continuum γ-ray yields the probability *P (E, E_γ)* for a particular excitation energy window and is fitted with an expression given by

$$P(E, E_\gamma) \sim \tau(E_\gamma) \times \rho(E - E_\gamma) \tag{2.17}$$

where $\tau(E_\gamma)$ is the γ-ray strength function(γSF) and $\rho(E - E_\gamma)$ is nuclear level density (NLD). From this comparison gamma-ray strength function and NLD are simultaneously determined up to particle threshold energy. This NLD and γSF are used in statistical model calculations to constrain the rate of capture reaction[87].

B. Surrogate reaction

In general surrogate reaction method was used mainly to determine the decay channel branching ratios of compound nucleus relevant to requirement. In statistical model theory, the capture reaction cross section expressed as the product of the compound nucleus (CN) formation cross section and the probability of decay branching channel [67, 68]. The formation cross section of CN is calculated from theory using potential model potential parameters, with relatively higher accuracy than the decay probability. The decay of compound nucleus from an excitation energy is independent of its formation. In surrogate method, transfer or inelastic reactions are used to populate the compound nucleus in astrophysical relevant excitation energy region and measured the decay probability of astrophysical relevant channel [68]. Finally, the extracted decay probability is used to constrain capture reaction rate in SM calculation.

C. Particle evaporation technique

The particle evaporation technique is mainly used to determine NLD of a residual nucleus that is formed after particle emission from the compound nucleus. Experimentally fusion evaporation reaction is used so that the evaporated particles are measured. This evaporated particle spectrum is compared with SM model calculation and NLD is extracted as a function of energy. This slope of NLD used to constrain NLD, γ-ray transmission coefficient to calculate the cross section of capture reactions.

2.2.3 Methods used in the present thesis

Present thesis work deals with the modeling of the astrophysical capture reactions ^{22}Ne(p, γ)^{23}Na in NeNa cycle, ^{68}Zn(n, γ)^{69}Zn in s-process nucleosynthesis path and $\alpha\alpha$(n, γ)^{9}Be in r-process nucleosynthesis path, based on the application of indirect nuclear reaction techniques to extract the relevant quantities for the models.

1. The modeling ^{22}Ne(p, γ)^{23}Na capture cross section has been done using ANC mathod used to describe the cross section or astrophysical S-factor data.
2. The ^{68}Zn(n, γ)^{69}Zn capture cross section has been modeled with the nuclear level density parameter of the model derived experimentally using the particle evaporation technique.
3. The $\alpha\alpha$(n, γ)^{9}Be capture cross section has been modeled using inelastic spectroscopy.

Chapter 3

The ^{22}Ne(p,γ)^{23}Na capture reaction

Proton capture reaction ^{22}Ne(p,γ)^{23}Na of the neon-sodium cycle of hydrogen burning in stars consumes ^{22}Ne, a seed nucleus for neutron production for *s*-process nucleosynthesis and converts to ^{23}Na, the only stable isotope of sodium. The reaction occurs in the convective envelop of massive ($M \geq 4M_{\odot}$) asymptotic giant branch (AGB) stars at temperature $T \approx 1.0 \times 10^{8}$K ($T_9 \approx 0.1$). In more massive stars ($M \geq 50M_{\odot}$), the reaction takes place in the surface layer along with the carbon-nitrogen-oxygen (CNO) and magnesium-aluminum (Mg-Al) cycles of hydrogen burning at temperature up to $T_9 \approx 0.8$ [88, 89, 90, 91].

Since oxygen is destroyed in the CNO cycle and Na is produced in the Ne-Na cycle, the reaction ^{22}Ne(p,γ)^{23}Na is said to be responsible for the observed anti-correlation in surface oxygen and sodium abundances in galactic globular clusters [14, 92, 93]. In addition to the AGB star scenario and the HBB process, hydrogen-burning of ^{22}Ne also plays a role in explosive nucleosynthesis scenarios.

• In classical novae—-(0.15 ≤ T ≤ 0.45 GK, 150 ≤ E_p ≤ 300 keV) [94].

• For an oxygen-neon nova, the uncertainty on the ^{22}Ne(p,γ)^{23}Na reaction rate leads to 6 orders of magnitude uncertainty on the ^{22}Ne yield [95].

• For a carbon-oxygen nova, ^{22}Ne(p,γ)^{23}Na was found to affect the abundances of ele-

ments between neon and aluminum [95].

• In core-collapse supernova precursors, proton capture on ^{22}Ne competes with the neutron source reaction ^{22}Ne(α, n)^{25}Mg, thus affecting neutron capture nucleosynthesis [96]. As a consequence, there is a call for a more precise ^{22}Ne(p,γ)^{23}Na thermonuclear reaction rate for several highly topical astrophysical scenarios ranging from AGB stars to supernovae. In Table 3.1, the reaction rates at T $\approx$ 0.1 GK found in the literature are tabulated. The contribution of direct capture component of astrophysical S-factor at relative energy E=0, $S_{DC}(0)$, in the total astrophysical S-factor at zero energy is also shown. In astrophysical relevant energy region, several resonance states of ^{23}Na along with the off-resonance part contribute in ^{22}Ne(p,γ)^{23}Na reaction rate. The relevant resonances and direct capture transitions have been shown in Fig. 3.1.

In this thesis, we primarily report a detailed analysis of the available S-factor data for non-resonance capture to the ground state and 440, 2392, 2982, 6318, 6918, and 8664 keV excited states of ^{23}Na nucleus and the total non-resonant S-factor data within the framework of R-matrix model. The aim is to investigate the energy dependence of the total off-resonance astrophysical S-factor including the contribution of broad, sub-threshold (-130 keV) state at 8664 keV and to extend the curve to still lower energy of astrophysical interest. The spectroscopic information required for the R-matrix calculation for the direct capture contribution has been extracted from the re-analysis of one proton transfer reaction data on ^{22}Ne from the literature. The total reaction rate is then estimated from the calculated reaction rate due to the off-resonance process and using the measured strengths of important low energy resonances in ^{23}Na except for the state with resonance energy of 151 keV. Experimental evidence shows that the state at 8945 MeV excitation corresponding to resonance energy 151 keV is actually a doublet with the capture of d- and f-waves respectively. A reanalysis of proton transfer reaction to 8945 MeV unbound state (Q_p = 8794 MeV) has been performed to extract the resonance strengths indirectly. This constitutes the second part of the present analysis. The resultant reaction rate up to T = 1.0 GK has been compared with the recent estimations.

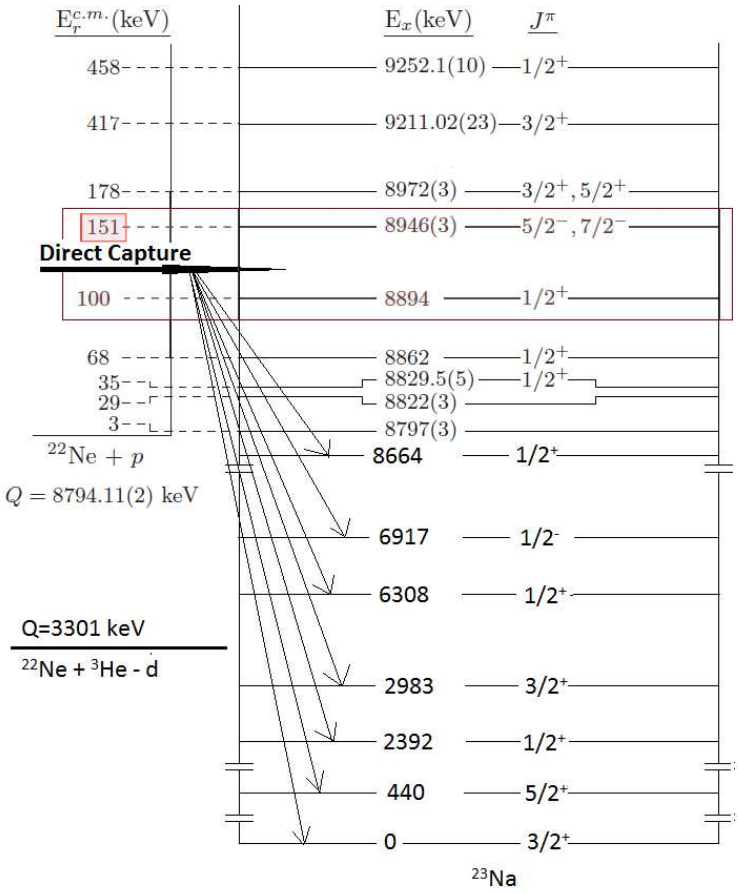

Figure 3.1: Level scheme of ^{23}Na

Table 3.1: Present status of $^{22}Ne(p,\gamma)^{23}Na$ reaction rate.

Year	$S_{DC}(0)$ (keV.b)	Reaction rate(T_9 ~0.1) $cm^3mol^{-1}s^{-1}$
Rolfs 1975 [97]	67±19	-
Gorres 1983 [98]	62	-
Hale 2001 [99]	-	2.1×10^{-9}
Sallaska 2013 [100]	-	5.52×10^{-9}
Cavanna 2015 [101]	-	6.6×10^{-8}
Depalo 2016 [102]	-	2.7×10^{-8}
Kelly 2017 [103]	-	3.53×10^{-8}
Ferraro 2018 [104]	50±12[104]	2.1×10^{-8}

3.1 Relevant Previous Work

• Rolfs measurement in 1975[97]:

The ^{22}Ne(p,γ)^{23}Na capture reaction was studied in the proton energy range E_p=0.37 to 2.1 MeV. Only direct-capture transition to six bound state (E_x= ground state and 440, 2392, 2982, 6308, 6917 keV) observed with significant contribution. The astrophysical S-factor at zero energy extrapolated from these data to stellar energies, is S(0) = 67 ± 12 keV b.

• G*ö*rres measurement in 1982[105]:

The ^{22}Ne(p,γ)^{23}Na capture reaction had been further studied in the energy range of E_p=0.077 to 1.6 MeV in steps 20 keV. Nine expected resonances were observed within this energy range and upper limits were summarized.

G*ö*rres measurement in 1983[98]:

The ^{22}Ne(p,γ)^{23}Na capture reaction was remeasured in the same energy range of E_p=0.37 to 2.1 MeV but in small energy steps to compare with the data from Rolfs work.The direct-capture transitions to several bound states were observed with a significant contributions. The astrophysical S-factor extrapolated from this re-measurement, is S(0) = 62 keV b.

• Hale measurement in 2001 [99]

The direct capture component had been studied by Rolfs and Gorres but the resonance component was not accurately determined. Hale *et al.* re-examined the states near the ^{22}Ne + p threshold using the ^{22}Ne(^{3}He,d)^{23}Na transfer reaction in an effort to determine more precise proton widths, and, therefore, leading to a more accurate rate for the ^{22}Ne(p,γ)^{23}Na reaction at low temperatures. The resonance strengths of the astrophysical important resonance states had also been estimated. A new rate for the ^{22}Ne(p,γ)^{23}Na reaction was calculated and its implications were discussed.

• Cavanna measurement in 2015 [101]

The first direct observations of the ^{22}Ne(p,γ)^{23}Na resonances at 156.2, 189.5, and 259.7 keV were reported. Their resonance strengths had been derived with 2 –7 % uncertainty. In addition, upper limits for three other resonances were greatly reduced. The new reaction rate reported a factor of 20 higher than the previous evaluation at a temperature of 0.1 GK, relevant to nucleosynthesis in asymptotic giant branch stars.

• Depalo measurement in 2016 [102]

Three resonances at 156.2 keV, 189.5 keV, and 259.7 keV proton beam energy, respectively, reported by Cavanna, et al. were remeasured with higher precision. For the levels at E_x = 8943.5, 8975.3, and 9042.4 keV excitation in ^{23}Na energy corresponding to the new resonances, the γ-decay branching ratios had been precisely measured. Three additional, tentative, resonances at 71, 105, and 215 keV proton beam energy, respectively, had not been observed by the authors. For the strengths of these resonances, experimental upper limits were derived that are significantly more stringent than the upper limits reported in the literature previously.

• Kelly measurement in 2017 [103]

In this work new measurements of resonances at E_R = 417, 178, and 151 keV and of the direct-capture process at 427 keV in the ^{22}Ne(p,γ)^{23}Na reaction have been performed. The resulting total ^{22}Ne(p,γ)^{23}Na rate was approximately a factor of 20 higher than the rate listed in a recent compilation at temperatures relevant to hot-bottom burning in AGB stars. Although the rate was close to that derived from a recent ^{22}Ne(p,γ)^{23}Na measurement by Cavanna et al. [101] in 2015, the large increase in the rate resulted in only a modest 18 % increase in the ^{23}Na abundance predicted from a 5 M_o thermally pulsing AGB star model from Ventura and DAntona (2005). The estimated astrophysical impact of this rate increase was in marked contrast to the factor of ∼3 increase in ^{23}Na abundance predicted by Cavanna et al. [101] and was attributed to the interplay between the ^{23}Na(p,α)^{20}Ne and ^{20}Ne(p,γ)^{21}Na reactions, both of which remain fairly uncertain at the relevant temperature range.

• **Ferraro measurement in 2018 [104]**

Three new resonances at E_p = 156.2, 189.5, and 259.7 keV were observed and confirmed by Depalo, et al. However, uncertainty on the reaction rate remained due to the contributions of the non-resonant process and the two suggested resonances at E_p = 71 and 105 keV. Here, new ^{22}Ne(p,γ)^{23}Na data with high statistics and low background were reported. Stringent upper limits of 6×10^{-11} and 7×10^{-11} eV (90% confidence level), respectively, are placed on the two suggested resonances. In addition, the off-resonant S-factor was measured at unprecedentedly low energy, constraining the contributions from a subthreshold resonance at excitation energy, E_x = 8664 keV in ^{23}Na and the direct capture process. As a result, at a temperature of 0.1 GK the error bar of the ^{22}Ne(p,γ)^{23}Na rate is now reduced by 3 orders of magnitude.

3.2 Modeling

3.2.1 Context of Present Modeling

The recent measurement by Ferraro et al.[104] reported a mean rate at T_9=0.1 which is about 18 % higher than the rate predicted by Kelly et al.[103] but 46% higher than the rate estimated by Depalo et al. [102]. Also, the value of ground state S-factor component of the direct capture process, obtained by Ferraro et al. [104] is relatively lower than that by Kelly et al. [103]. Again, Ferraro et al.[104] obtained a value of 13 ± 5 keV b from their analysis that is considerably higher than the value used by G*ö*rres et al. [105]. Although the direct capture cross-section is not significantly high in contribution, we intended to perform a consistent analysis of the direct capture data including the data from the recent measurement of Ferraro et al. [104] and then look at the temperature dependence of the rate of ^{22}Ne(p,γ)^{23}Na capture reaction.

3.2.2 Single particle transfer reaction

Transfer reaction is used to probe the nuclear structure, like the single-particle nature of the states of the residual nucleus from one particle transfer reaction [29]. Typically, the spectra of final states and angular distributions are measured in experiments. Considering the direct, one step nature of the transfer reaction, the perturbative approach of Born Approximation is employed to describe the process, either in the from of Plane Wave (PWBA) or the Distorted Wave (DWBA) from is used[106]. The PWBA describes only the forward angle region (i.e Coulomb dominated region) of the distribution but fails to describe the whole angular range of it [106]. If nuclear interaction has a significant role in the transfer process for given energy then incoming and outgoing waves are distorted. To take into account the nuclear potential effect, DWBA theory has been introduced that predicts experimental angular distribution data accurately the whole angular region. Differential cross-section of transfer reaction A(a,b)B is written as

$$\left(\frac{d\sigma}{d\Omega}\right)_{exp} \propto |T_{\beta\alpha}|^2 \tag{3.1}$$

where, α, β denote the entrance (A + a) and exit (B + b) channels respectively. $T_{\beta\alpha}$ represents transition amplitude for transfer process.

$$T_{\beta\alpha} = \int \chi^{(-)}(\overrightarrow{k_\beta}, \overrightarrow{r_\beta})^* < \Psi_B \Psi_b | \Delta V | \Psi_A \Psi_a > \chi^{(+)}(\overrightarrow{k_\alpha}, \overrightarrow{r_\alpha}) \tag{3.2}$$

The $\chi^{(-)}$ and $\chi^{(+)}$ are incoming and outgoing two-body scattering wave functions describing the relative motion of the initial and final channel. This scattering wave function is generated from the optical model potential of incoming and outgoing channels. The factor within the bra-ket notation in Eqa. 3.2 representing the nuclear matrix is called the form factor. This factor plays the role of a perturbative interaction for the transition from the initial state α to final state β and contains all the nuclear structure-related information. Basically, it includes two nuclear overlaps: (i) Target overlap $< \Psi_B | \Psi_A > \propto [C^2S(B \rightarrow A + x)]^{1/2}_{l_1, j_1} * \phi^B_{l_1, j_1}(r_{Ax})$ and (ii) The projectile overlap $< \Psi_b | \Psi_a > \propto [C^2S(a \rightarrow b + x)]^{1/2}_{l_2, j_2} * \phi^a_{l_2, j_2}(r_{bx})$. The ϕ-s describe the bound state wave functions between $A - x$ in nucleus B with quantum numbers l_1, j_1 and $b - x$ in nucleus a with quantum numbers l_2, j_2.

$C^2S(B \rightarrow A + x)$ and $C^2S(a \rightarrow b + x)$ are the spectroscopic factors (S_{lj}) times the square of the isospin Clebsch Gordon coefficient (C^2) respective overlap configurations.

3.2.3 Determination of spectroscopic factor

i) By comparing the shape of the measured angular distributions with DWBA calculations, the quantum numbers nlj of the single-particle orbitals involved could be determined(not always uniquely). From this quantum numbers nlj of the single-particle orbitals, we calculate spin, parity of the states populated.

ii)The spectroscopic factor of the state populated, S_{nlj}, n being the number of nodes in the bound state wave function without counting the origin, can be determined by comparing the absolute value of measured transfer reaction cross-section with the theoretical cross-section obtain from DWBA calculations assuming the spectroscopic factor for the overlap to be unity. In the finite range DWBA (FRDWBA) model, conventionally the experimental cross-section of a transfer reaction $A + a(= b + x) \rightarrow B(= A + x) + b$ (where x is the transferred particle) is written in terms of the calculated cross section as

$$\left(\frac{d\sigma}{d\Omega}\right)_{exp} = (C^2S)_{bx}(C^2S)_{Ax}\left(\frac{d\sigma}{d\Omega}\right)_{mod} \tag{3.3}$$

where C^2S_{bx} is the product of spectroscopic factor S_{bx} and isospin Clebsch-Gordan coefficient C^2_{bx} of $b + x$ configuration in projectile a and C^2S_{Ax} is that for $A + x$ configuration in residual nucleus B. $\left(\frac{d\sigma}{d\Omega}\right)_{mod}$ is the cross section obtained from model calculation.

The spectroscopic factor is proportional to the "probability" that a many-body system (the nucleus) is found in a certain configuration. The determination of spectroscopic factors from one-nucleon transfer reactions was and is crucial in building our current understanding of the fermionic degrees of freedom in nuclei and their coupling to other types of excitation. However, in determining the absolute values of the spectroscopic factors as the ratio between the experimental cross-section and the DWBA calculated cross-section one makes (1) a strong assumption that the single-particle configuration assumed is dominant in the wave function (actually in the contribution to the cross-section

measured) of the state under consideration and (2) that the parameters used in the DWBA calculations are appropriate.

3.2.4 Transfer to bound state and Asymptotic Normalization Coefficients (ANC-s)

In the transfer reaction process involve with target overlap

$$I^B_{Ax} =< \Psi_B|\Psi_A >= [C^2S(B \rightarrow A + x)]^{1/2}_{l_f,j_f} * \phi^B_{l_f,j_f}(r_{Ax}) \tag{3.4}$$

In the parifarial region (beyond the nuclear radius,R_N) $\phi^B_{l_f,j_f}(r_{Ax}) \approx b_{l_f j_f} \frac{W_{\eta,l+1/2}(2k_{Ax}r_{Ax})}{r_{Ax}}$ and $I^B_{Ax} = C^B_{Ax} \frac{W_{\eta,l+1/2}(2k_{Ax}r_{Ax})}{r_{Ax}}$. It is related to the spectroscopic the factor from Eqa 3.4 of the two-body configuration as

$$C_{J_f l_f} = \sqrt{(C^2S)_{J_f l_f}} b_{l_f j_f} \tag{3.5}$$

where $C^2S_{J_f l_f}$ is the spectroscopic factor of the configuration in the composite nucleus with total spin J_f. The relative orbital angular momentum and spin of the two clusters in the final bound state are denoted by l_f and j_f. $C_{J_f l_f}$ is the corresponding ANC and $b_{l_f j_f}$ is the single-particle asymptotic normalization constant (SPANC) with l_f and j_f quantum numbers of the bound state orbital used in the DWBA calculation. The SPANC b is expressed in terms of bound state wave function of the composite nucleus [3] as

$$b(r_0, a_0) = \frac{u(r, r_0, a_0)}{W_{-\eta,l+1/2}(2\kappa r)} \tag{3.6}$$

in the asymptotic radial region. $W_{-\eta,l+1/2}(2\kappa r)$ is the Whitaker function, $\kappa = \sqrt{2\mu\epsilon}$ the wave number, and μ, ϵ, R_N are the reduced mass, binding energy and the nuclear interaction radius, respectively for the bound state of the final nucleus. Both bound state wave function and Whitaker function have similar radial fall of in the asymptotic region. The parameters r_0 and a_0 are the radius and diffuseness parameters of the Woods Saxon potential generating the required bound state wave function. The spectroscopic factor so determined includes the effect of the nuclear interior and measures the many-body effect

in the transfer reaction process. It depends on the choice of the potentials, more sensitively on the geometry parameters of bound state potential used to describe a particular configuration. In low energy radiative capture reactions where the behavior of the wave function at large separation is important, instead of spectroscopic factor, asymptotic normalization coefficient or ANC is more relevant a quantity. ANC measures the amplitude of the tail of the overlap function between the bound state wave functions of initial and final nuclei.

3.2.5 Transfer to unbound state and particle decay width

If transfer to the unbound state above the particle threshold has taken place then the particle decay width (Γ_p) of the state is related to the extracted spectroscopic factor (C^2S) by the relation

$$\Gamma_p = (C^2S)\Gamma_{sp} \tag{3.7}$$

where C^2S represent the spectroscopic factor of the resonant state of ^{23}Na for the particular configuration and Γ_{sp} is the single-particle width of the state. The width Γ_{sp} for a pure single-particle configuration depends, like the spectroscopic factor, on the choice of the nuclear potential used to generate the corresponding wave function. It is observed that partial width Γ_p is more-or-less independent of the chosen parameters as C^2S and Γ_{sp} have opposing trends of dependence on the parameters.

3.3 Present DWBA Calculation

In this present work, the model calculation progressed in two steps. In the first step, the data from ^{22}Ne(^{3}He,d)^{23}Na transfer reaction to the states of ^{23}Na (E_x= G.S, 440, 2392, 2982, 6308, 6917, 8664 keV bound state) have been reanalyzed to extract the Asymptotic Normalization Coefficients (ANCs) and to extract the proton decay width(Γ_p) of E_x=8945(E_R=151) keV state for its doublet configuration, respectively.

3.3.1 DWBA analysis of ^{22}Ne(^{3}He,d)^{23}Na reaction and extraction of ANC

For bound state of ^{23}Na

To extract the spectroscopic factors from data, a finite range distorted wave Born approximation (FRDWBA), using the code FRESCO (ver. 2.9) [115], has been performed for ^{22}Ne(^{3}He, d)^{23}Na transfer reaction. Angular distribution data, measured at 15 MeV incident energy of ^{3}He, for transfer to ground state and 440, 2392, 2982, 6308, 6917 keV excited states are taken from Ref. [116]. In the reanalysis of 15 MeV data, within the FRDWBA framework, the optical model potential parameters for entrance and exit channels are taken from Ref. [116]. Standard Woods-Saxon form has been used for the potentials. The shape parameters for the bound sate potentials related to ^{22}Ne+p and d+p systems are from Refs. [116] and [117], respectively. The strengths of the bound state potentials are varied to get the binding energies of the states of the composite nuclei.

The model calculations reproduced the angular distributions for transfer to ground state and 440, 2392, 2982, 6308, 6917 keV excited states of ^{23}Na quite well shown in Fig. 3.3. While extracting the spectroscopic factors of the states of ^{23}Na, the spectroscopic factor C^2S_{dp} for ^{3}He is taken as 1.092, a value that is derived for the ^{3}He ground state with $d+p$ configuration using the method reported in Ref.[117]. The resultant spectroscopic factors of ^{23}Na states are shown in Table 3.2. The values obtained from the present FRDWBA analysis match well with those reported from zero range DWBA calculation in Ref. [116].

For E$_x$=8664 keV sub-threshold resonance state

The excited state 8664 keV of ^{23}Na is 130 keV below the proton threshold at 8794 keV. Capture through this sub-threshold resonance controls the low energy behavior of the astrophysical S-factor of ^{22}Ne(p,γ) reaction. In order to extract the spectroscopic factor of this state we again performed an FRDWBA calculation for the transfer reaction ^{22}Ne(^{3}He,d) at 20 MeV with the data from Ref. [99]. In order to get more precise optical model potentials (OPM), elastic scattering angular distribution data are fitted with

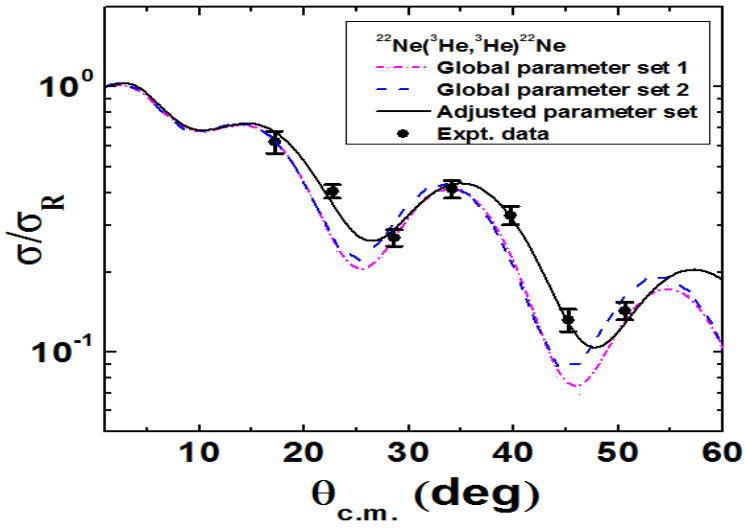

Figure 3.2: The elastic scattering angular distributions compare with model calculation for different sets of optical model calculation.

Table 3.2: Spectroscopic factors and asymptotic normalization coefficients (ANC-s) for the six states of ^{23}Na.

E_x (keV)	J^π	nl_j	C^2S^1 Present	C^2S Ref. [116]	b ($fm^{-1/2}$)	ANC ($fm^{-1/2}$)
g.s.	$3/2^+$	$1d_{3/2}$	0.082±0.012	0.08	6.86	1.96±0.5
440	$5/2^+$	$1d_{5/2}$	0.38±0.08	0.35	7.62	4.69±0.8
2392	$1/2^+$	$2s_{1/2}$	0.26±0.05	0.25	17.56	8.8±1.6
2982	$3/2^+$	$1d_{3/2}$	0.35±0.04	0.32	4.38	2.59±0.87
6308	$1/2^+$	$2s_{1/2}$	0.14±0.02	0.13	11.14	4.16±0.79
6917	$1/2^-$	$2p_{1/2}$	0.18±0.04	0.15	7.27	3.1±0.7

different sets of OMP shown in Fig. 3.2. Potential parameters used to obtain the transfer angular distribution are given in Table 3.3. It has been observed that unlike the more deeply bound states in ^{23}Na, a complex remnant term is required to obtain a very good overall fit to the angular distribution data. The parameters of d+^{22}Ne core-core potential are also given in Table 3.3. The resultant fit is shown by a solid red line in Fig. 3.4. The blue dashed-dotted line represents the FRDWBA calculation without the remnant term. Improvement in the fit is quite remarkable. In Col.5 of Table 3.4, the extracted spectroscopic factors have been shown. The value obtained from the present work is very close to the values reported in Refs. [99, 98].

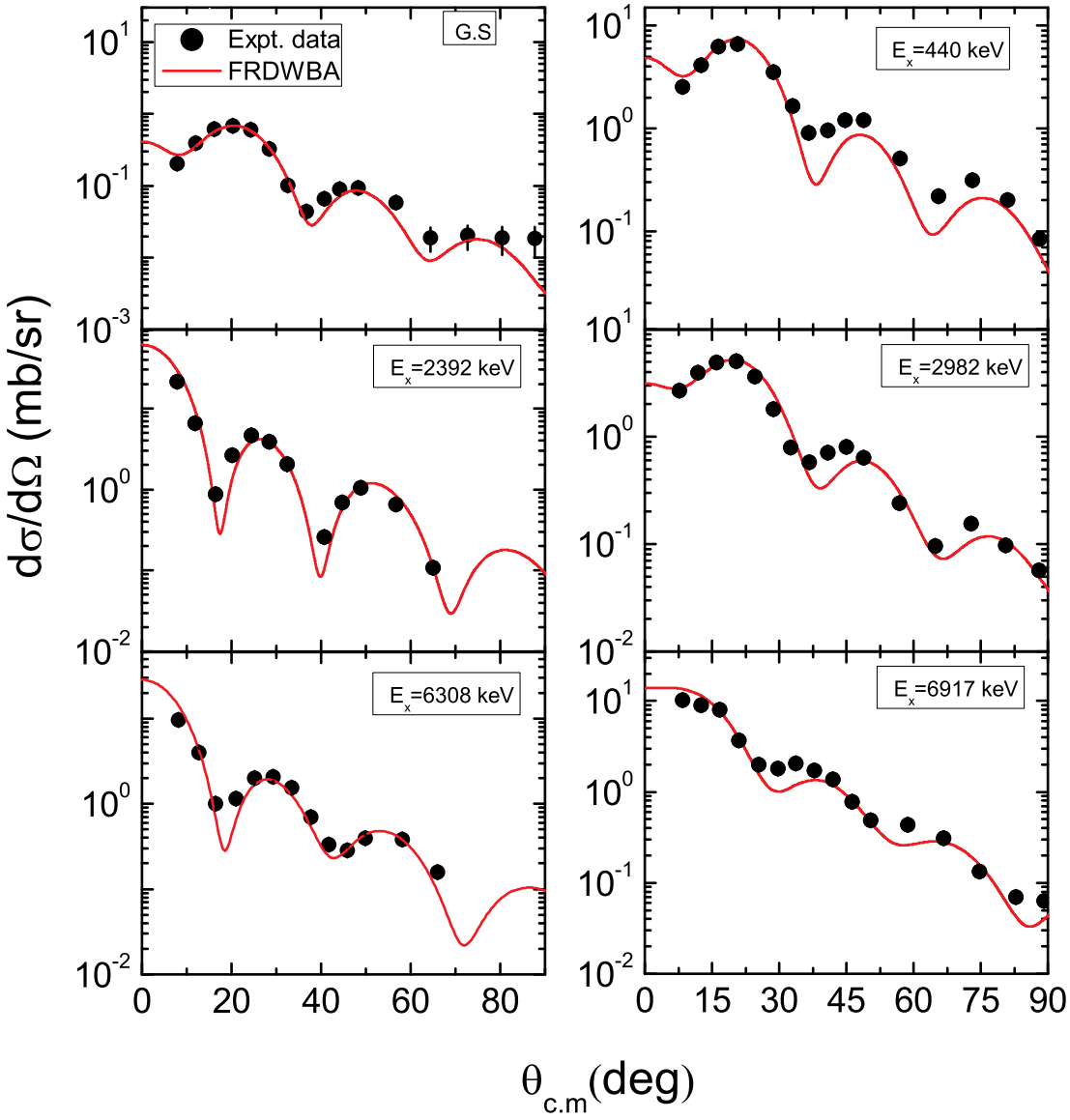

Figure 3.3: Transfer angular distributions fitted with FRDWBA model calculation.

Table 3.3: Potential parameters for ^{22}Ne(^{3}He,d)^{23}Na (E*= 8664 keV), E_{lab} = 20 MeV [99]. * Varied to match separation energy.

channel	V_r (MeV)	r_r (fm)	a_r (fm)	W_i (MeV)	W_D (MeV)	r_i=r_D (fm)	a_i=a_D (fm)	V_{so} (MeV)	r_{so} (fm)	a_{so} (fm)	r_c (fm)
^{3}He+^{22}Ne	Ref. [99]										
d+^{23}Na	Ref. [99]										
d+^{22}Ne	88.0	1.17	0.73	0.24	35.8	1.33	0.73	13.85	1.07	0.66	1.33
d+p	*	1.25	0.65					6.2	1.25	0.65	1.30
p+^{22}Ne	Ref. [99]										

Table 3.4: Spectroscopic factor and asymptotic normalization coefficient (ANC) of 8664 keV state of ^{23}Na

E_x (MeV)	J^{π}	l_p	nl_j	C^2S	b (fm$^{1/2}$)	ANC (fm$^{1/2}$)
8664[2]	1/2$^+$	0	2s$_{1/2}$	0.32±0.05	252[3]	143.7±15.2
				0.29[99]		
				0.3[98]		
				0.42±0.08[104]		
				0.58±0.08[118]		

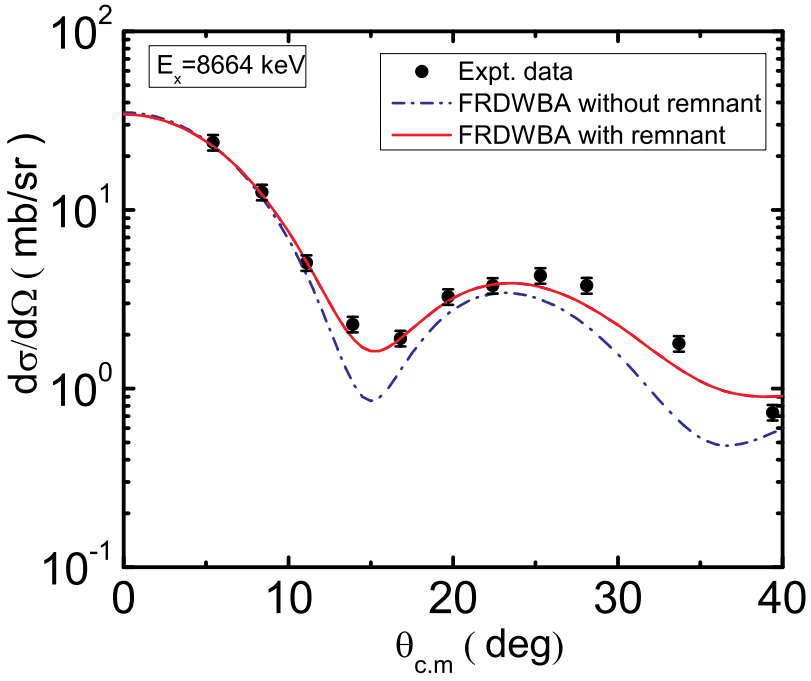

Figure 3.4: DWBA fit to angular distribution data of Power *et al.* [116] for the state E_x=8664 keV. The line represents calculated cross section

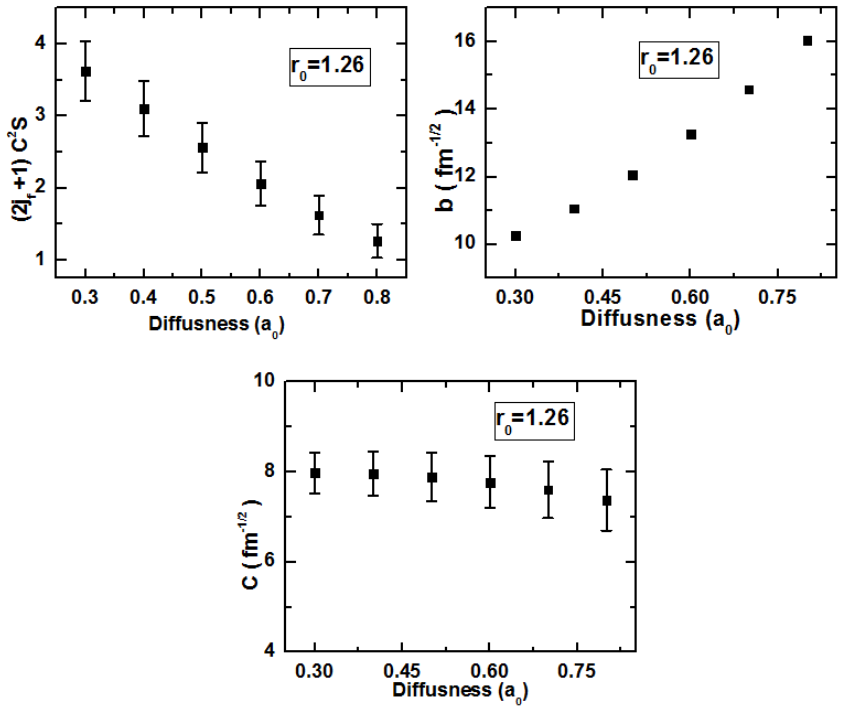

Figure 3.5: Variation of the spectroscopic factor, SPANC and ANCs with a_0 for E_x=440 keV state.

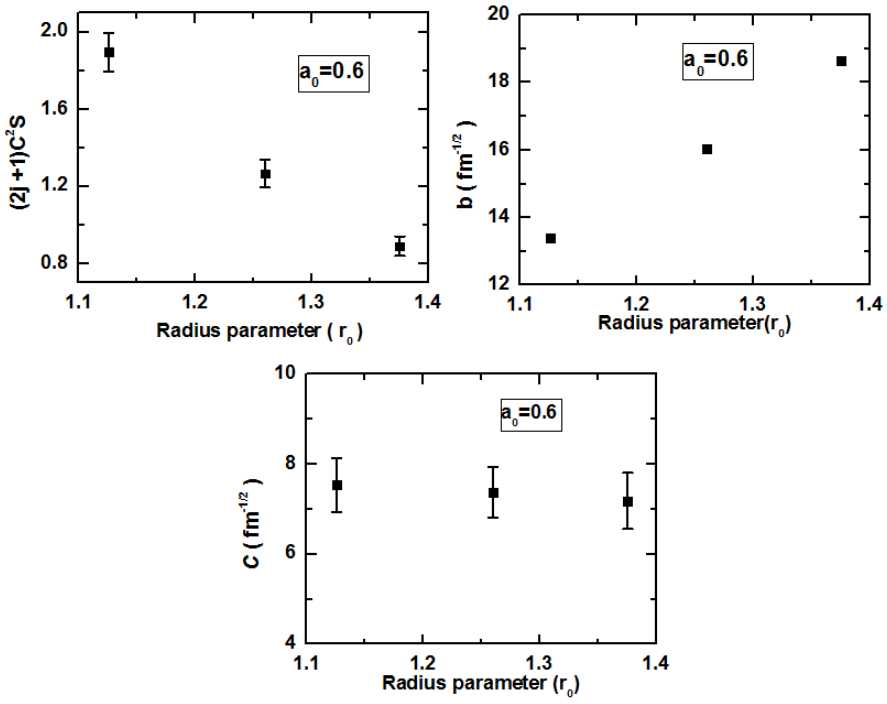

Figure 3.6: Variation of the spectroscopic factor, SPANC and ANCs with r_0 for E_x=440 keV state.

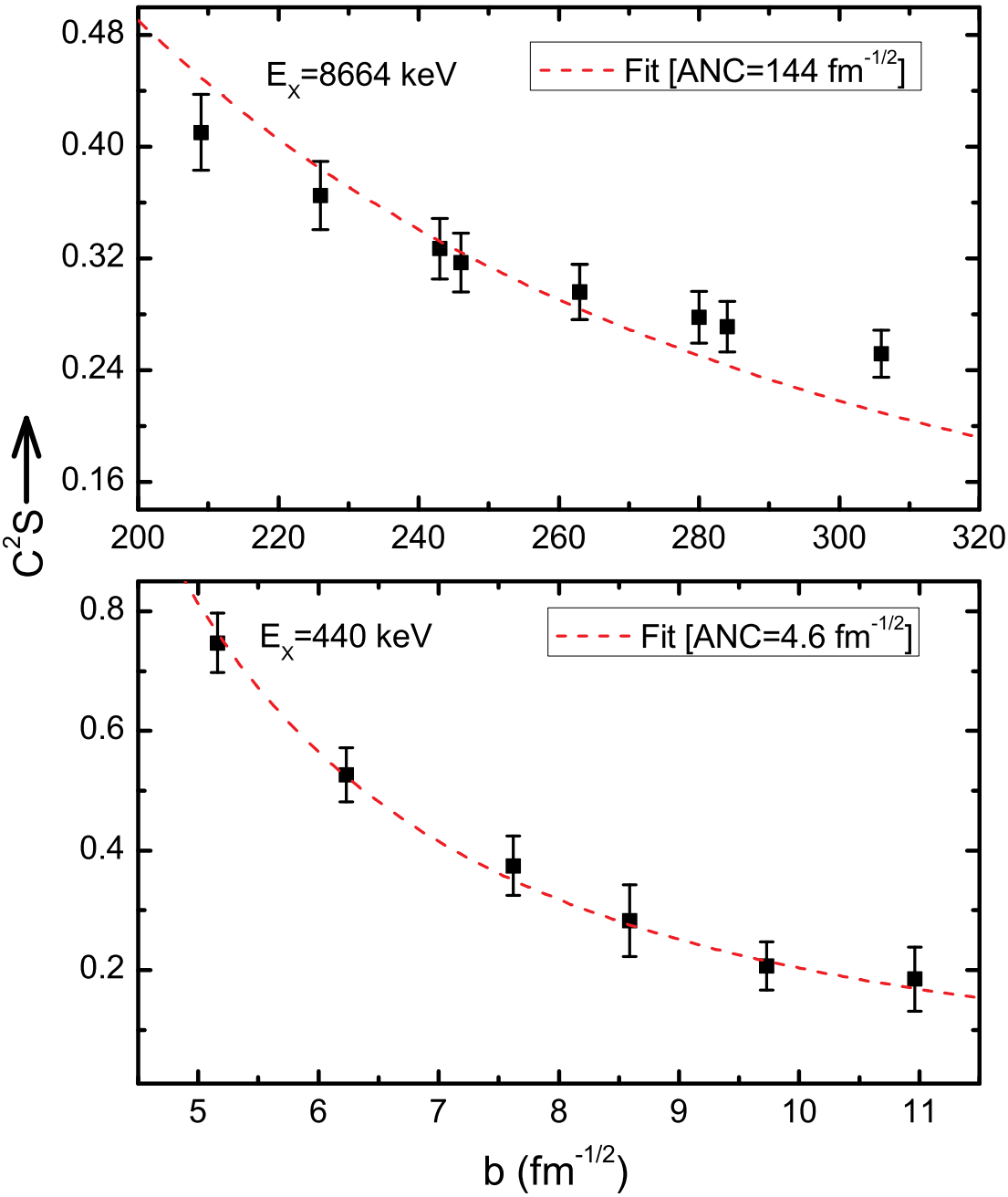

Figure 3.7: Variation of the spectroscopic factor with single particle ANC for 8664 MeV (top panel) and 440 MeV (lower panel) states.

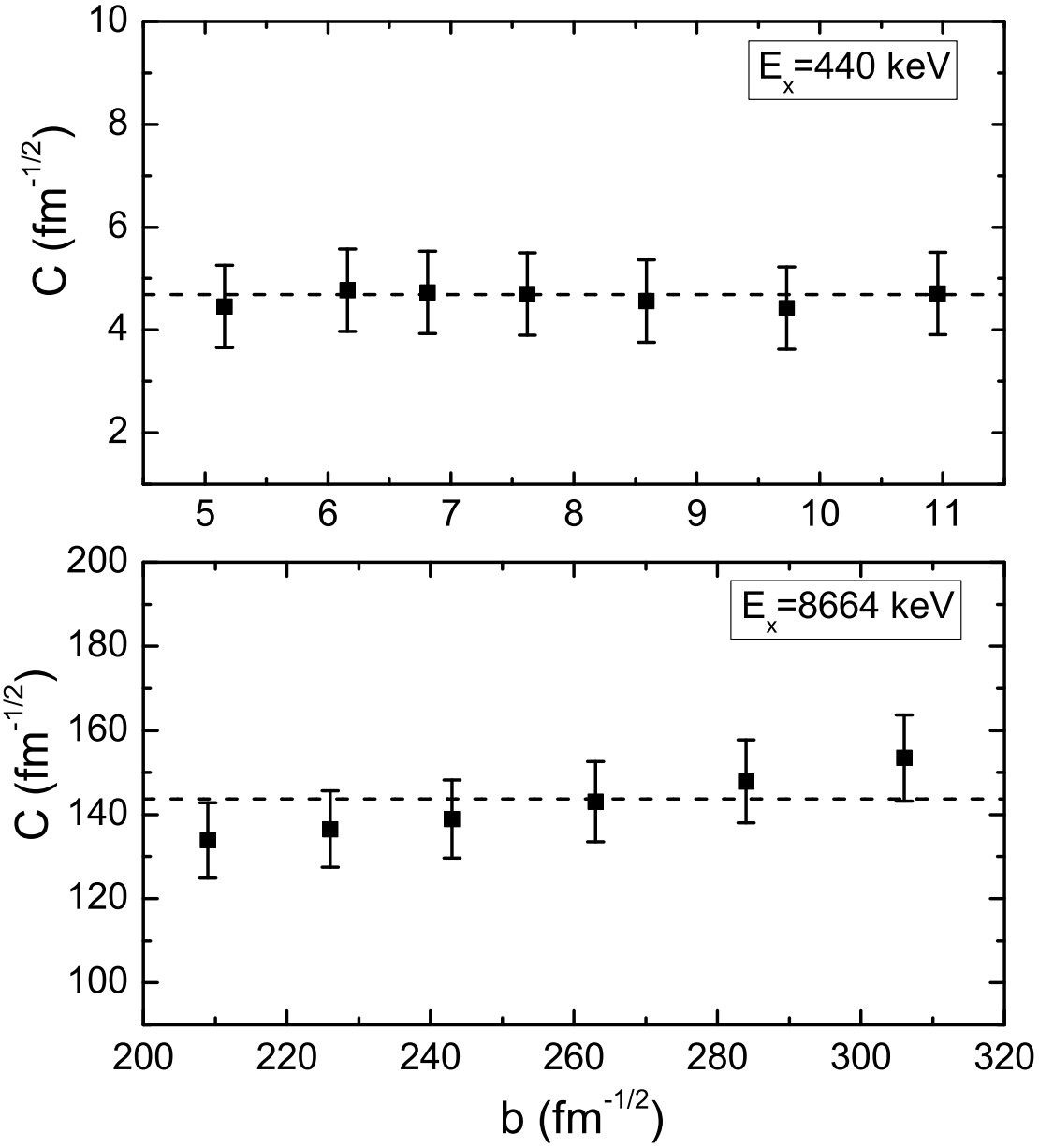

Figure 3.8: Variation of ANC (C $fm^{-1/2}$) as a function of SPANC (b $fm^{-1/2}$) for 440 keV (top panel) and 8664 keV (bottom panel) states.

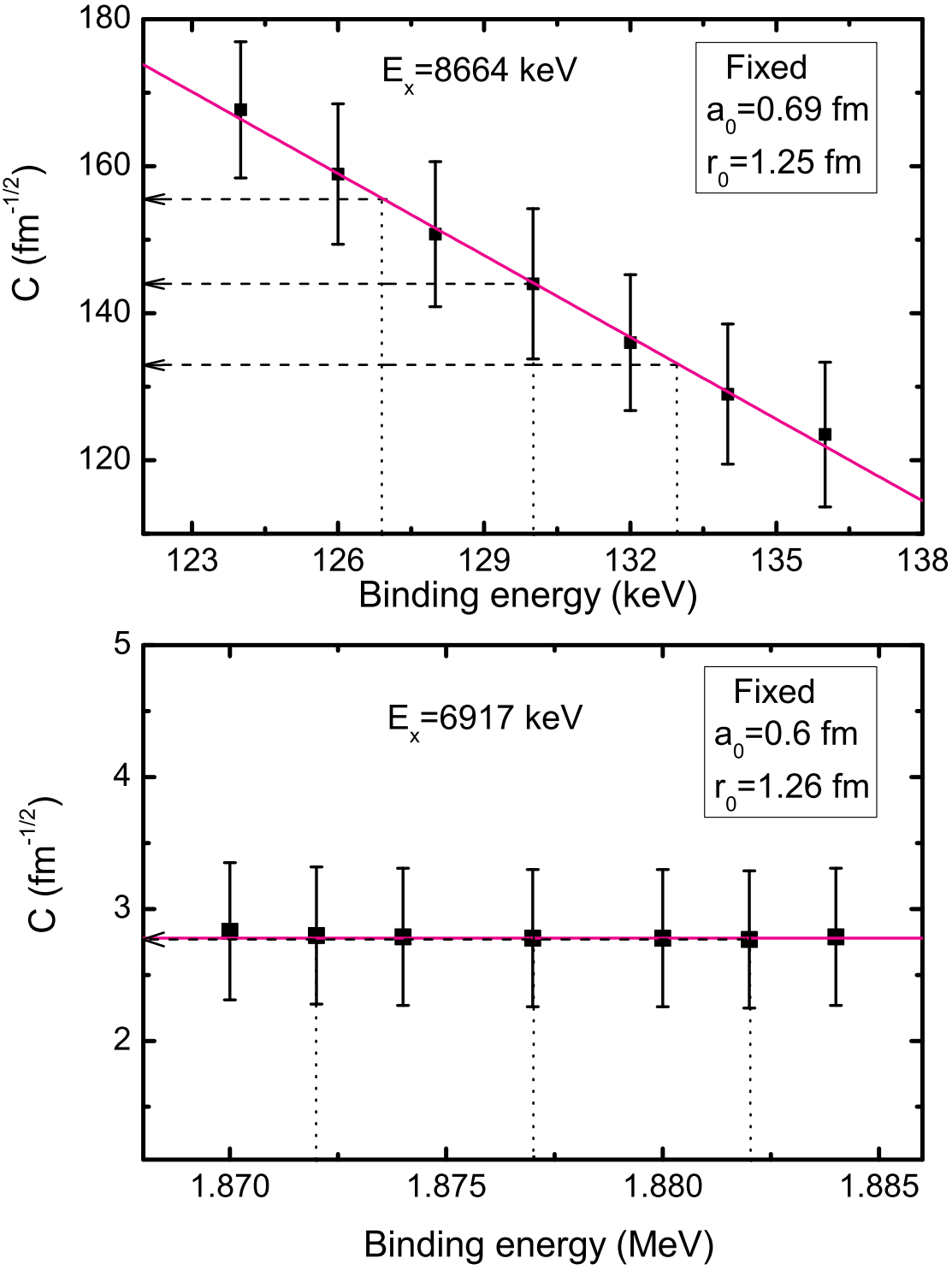

Figure 3.9: Variation of ANC (C $fm^{-1/2}$) as a function of binding energy for 8664 keV (top panel) and 6917 keV (bottom panel) states for fixed geometry parameters of bound state potential.

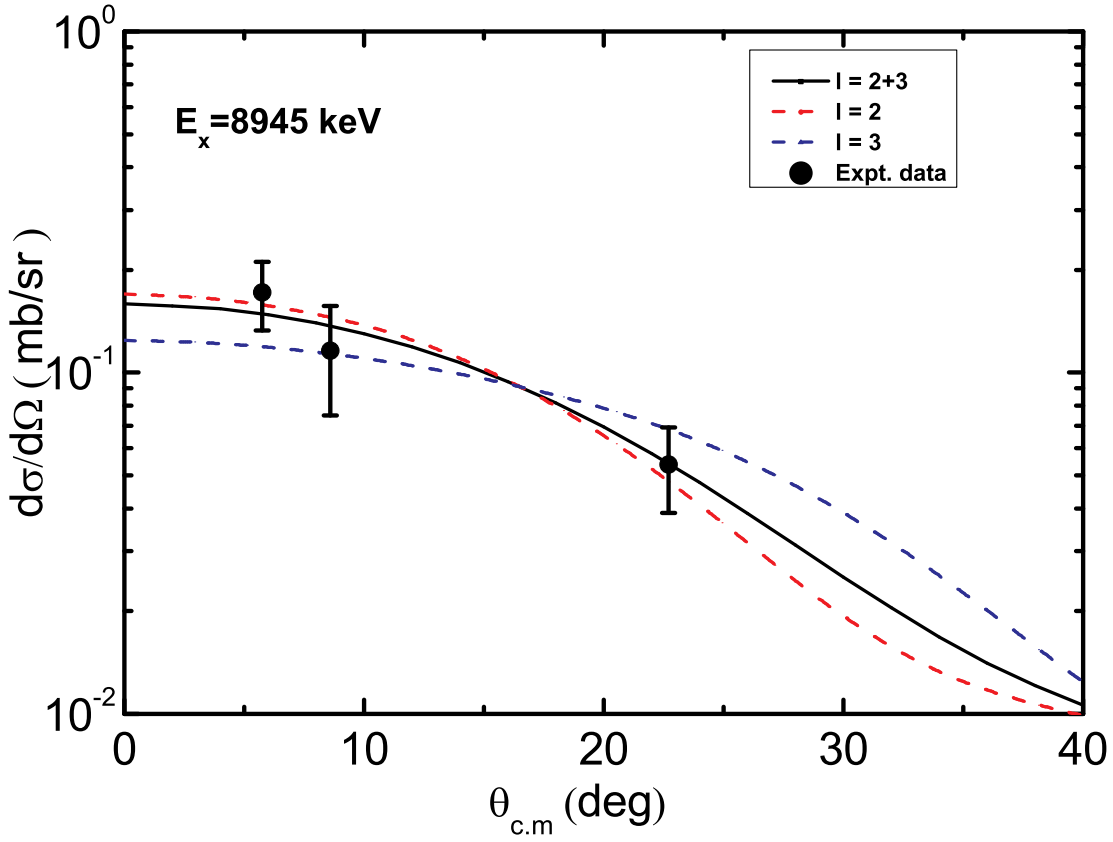

Figure 3.10: Angular distribution data and DWBA fits to 151 keV resonance state of 23Na.

Parameter independence of extracted of ANC

In the present work, the value of SPANC, $b_{l_f j_f}$, associated with each bound state has been obtained from the best fit ratio value using Eq.3 for the region beyond the nuclear interaction radius (R_N = 5.5 fm). Like the spectroscopic factor, SPANC b also depends on the choice of potential parameters. But the variations of the two quantities with the geometry parameters of the bound state potential are opposite in nature. Typical variation of the spectroscopic factor, SPANC b and ANC with r_0 and a_0, for E_x=440 keV state, have been shown in Fig. 3.5 3.6 respectively. Hence, the product of these two quantities that give the required ANC, remains constant with the change of potential parameters for a peripheral reaction. Thus, for a pure peripheral condition the variation of the spectroscopic factor should be proportional to the inverse square of SPANC value [119] from Eq.3. In Fig. 3.7 we have shown the plots of variation of C^2S as a function of SPANC b for the 8664 keV sub-threshold state and deeply bound 440 keV state. The error shown in the figure for C^2S includes the uncertainty of DWBA fit to the angular distribution data for a particular SPANC value obtained for the chosen r_0 and a_0 parameters of the bound state potential and the experimental error of individual cross-section data. The radius and diffuseness parameters have been changed in small steps and the corresponding SPANC value are generated. The fits with inverse square function to the extracted data ensure the peripheral nature of the process and hence the correctness of the extraction of ANC value. In the case of 8664 keV state, which is a sub-threshold state, the reproduction of the variation does not follow a purely inverse square dependence. The mismatch is a result of the non-reproduction of the tail part of this weakly bound state with the asymptotic radial behavior of the Whitaker function. The values of SPANC-s and the corresponding ANC-s of the states of ^{23}Na have been listed in Tables 3.2 and 3.4.

Uncertainties of extracted ANC values

The uncertainty of the estimated value of ANC has been calculated by propagating the error of the spectroscopic factor through the relation given in Eq.2. In Fig. 3.8, extracted ANC with the estimated error has been shown as a function of b, the SPANC. The fit

Table 3.5: Angular momentum transfers, spectroscopic factors and proton widths of 8945 MeV state in ^{22}Ne(^{3}He,d)^{23}Na reaction.

E_x (keV)	J^π	l_p	nl_j	C^2S Present	C^2S (Litt.) Ref.[99]	Γ_p (keV)
8944	$3/2^+$	2	$1d_{3/2}$	$(5.54\pm1.41)\times10^{-4}$	8.32×10^{-4}	$(9.99\pm2.50)\times10^{-8}$
8945	$7/2^-$	3	$1f_{7/2}$	$(3.94\pm0.9)\times10^{-4}$	$\leq1.08\times10^{-3}$	$(9.83\pm2.24)\times10^{-10}$

to these secondary data points produces the mean ANC value along with its uncertainty. Besides, the dependence of the extracted ANC on the binding energy of the state has also been checked. In Fig. 3.9, we have shown the plots of ANC as a function of binding energy [120] for the states at 8664 keV and 6917 keV excitation energies of ^{23}Na. The binding energy of a state is varied keeping the geometry parameters of the bound state potential corresponding to the mean ANC value for the state fixed. The plots show that unlike the more bound 6917 keV state, the ANC value of sub-threshold state 8664 keV decreases with the increasing binding energy. Thus for the 8664 keV state, the uncertainty of the ANC due to the ±3 keV [99] uncertainty in the binding energy has been estimated graphically from the plot shown in Fig. 3.9. Uncertainties in the ANC-s for other deeply bound states corresponding to the error in the binding energies are negligibly small and not considered.

DWBA calculation for E_x=8945 keV resonance state

The state at excitation of 8945 keV in ^{23}Na is a resonance state about 151 keV above the proton threshold. It has an important contribution to the reaction rate of ^{22}Ne(p, γ) reaction at T = 0.1 GK as it falls within the Gamow window at this temperature. In earlier reports [105, 99], it was considered that at this excitation a single state exists with generally adopted spin parity of $7/2^-$. Later Jenkins, et al.[121] in their γ spectroscopic study of ^{23}Na has shown that at this excitation the nucleus has a doublet of states with about a keV difference in excitation energy. One of them has a spin parity of $J^\pi = 7/2^-$ and decays to $9/2^+$ and $5/2^+$ states of ^{23}Na by dipole transitions. The assignment is consistent

with a $l = 3$ angular momentum transfer from a (d, n) study [122]. On the other hand, the measurement also shows a distinct coincidence of a 3914 keV γ ray depopulating the $5/2^+$ state at 3914 keV excitation with a 5030 keV γ ray that depopulates the relevant 8944 keV state. A spin parity of $3/2^+$ has been assigned to this second state from its decay branches and angular correlation ratio. In a further study, Kelly, *et al.* [103] have also observed a strong primary transition from this $3/2^+$ state to the $5/2^+$ 3914-keV state with a branching ratio of 80% and to the $1/2^+$ 2391 keV state with 20%. Authors have also performed zero-range DWBA fits to the data of ^{22}Ne(^{3}He, d)^{23}Na* (8945 MeV) reaction [99] with l=1,2,3 angular momentum transfers. They opted for l=2 transfer assigning a $3/2^+$ spin-parity for the 8945 MeV state.

Although the number of data points in the angular distribution is small, we carried out a re-analysis within the zero range DWBA framework for this unbound state using the code DWUCK4 code [123]. The same set of potentials from Ref. [99] is used. Values obtained by Hale, *et al.* assuming a l=3 transfer and by Kelly, *et al.* [103] assuming l=2 are reproduced. Subsequently, we completed a least-square fit to the angular distribution data assuming that both l=2 (J^π=3/2$^+$) and l=3 (J^π=7/2$^-$) can contribute and the calculation yielded the spectroscopic factors shown in Col.5 of Table 3.5. The fits obtained are compared in Fig. 3.10. A normalizing constant N=4.42 has been used in the zero range DWBA calculation for (^{3}He,d) [99, 116]. It is apparent from Fig. 3.10 that the fit obtained considering the contributions of both l=2 and 3 is a better reproduction of the limited angular distribution data available.

The partial widths Γ_p have been estimated for the doublet states having excitation energy E_x= 8945 MeV from the extracted spectroscopic factors, using the relation

$$\Gamma_p = (C^2S)\Gamma_{sp} \tag{3.8}$$

where C^2S is the spectroscopic factor of the resonant state of ^{23}Na for the particular configuration and Γ_{sp} is the pure single particle width of the state. The width Γ_{sp} for a pure single-particle configuration depends, like the spectroscopic factor, on the choice of the nuclear potential used to generate the corresponding wave function. To estimate the systematic uncertainty in extracted Γ_p, we varied the radius and diffuseness parameters of

Table 3.6: Background pole parameters obtained from *R*-matrix fits

J^π	E_x (MeV)	Γ_P (MeV)	Γ_γ[E1] (eV)						
			R→g.s	R→0.44	R→2.39	R→2.98	R→6.30	R→6.91	R→8.66
$1/2^-$	15	5.0	589.92	-	2.77×10^3	499.10	912.64	-	118.42
$1/2^+$	15	5.0	-	-	-	-	-	4.41	
$3/2^-$	15	5.0	-	632.97	-	-	-	-	

the bound state potential from 1.125 to 1.375 fm and from 0.39 to 0.89 fm, respectively keeping the binding energy fixed. It is observed that partial width Γ_p is more-or-less independent of the chosen parameters as C^2S and Γ_{sp} have opposing trends of dependence on the parameters. In the last column of Table 3.5, the extracted particle widths have been listed. The error shown includes the fitting uncertainty as well as the systematic uncertainty. We retained the individual contributions of the doublet pair in the estimation of the rate of proton capture reaction within the relevant temperature window.

3.3.2 The ANC and capture cross section

The direct capture in charged particle induced reactions at low energy astrophysical process mainly occurs through the tail of the nuclear overlap function in the corresponding two-body channel. The shape of this tail part of the overlap function is dictated by the Coulomb interaction between x and A. Hence, the capture rate may be calculated accurately if one knows the amplitude of the tail, which is given by the ANC. The ANC determines the overall normalization of peripheral radiative capture reactions. Cross-section of a direct capture reaction A(a, γ)B for the direct transition from initial state a+A to final state B requires the calculation of matrix element of electromagnetic transition operator between the initial scattering state to final bound state and is written as

$$\sigma = \lambda < I^B_{Ax} | M_\lambda(r) | \psi^+_i(r) > \tag{3.9}$$

where λ contains kinematic factors, I^B_{Ax} is the overlap function for A+x configuration in

nucleus B in the final channel, M_λ(r) is the electromagnetic transition operator, and $\psi_i^+(r)$ is the incident scattering wave. For a low energy direct capture process, the dominant contribution to the matrix element comes from outside the nuclear radius,R_N. So the overlap function I_{Ax}^B may be replaced by

$$I_{Ax}^B \approx C_{Ax}^B \frac{W_{\eta,l+1/2}(2kr)}{r} \tag{3.10}$$

C_{Ax}^b defines the amplitude of the tail of the radial overlap function, I_{Ax}^B, $W_{\eta,l+1/2}(2kr)$ is the Whitaker function,η is the Coulomb parameter and $k = \sqrt{2\mu_{Ax}\epsilon_{Ax}}$ is the bound state wave number for the bound state B=A+x and ϵ_{Ax} is the corresponding binding energy. The same radial overlap function I_{Ax}^B is also present in DWBA formalism of transfer reaction of particle x transferred from a projectile(a) to target nucleus A. So the required ANCs can be determined from peripheral transfer reactions at energies above the Coulomb barrier or sub-Coulomb energies and used to calculate the peripheral radiative capture reaction. In the present thesis, we extracted the required ANCs from the ^{22}Ne($^3He, d$)^{23}Na transfer reaction and utilized them in the R-matrix calculation to obtain the direct capture cross section of ^{22}Ne(p, γ)^{23}Na reaction.

3.3.3 Phenomenological R-matrix description

The R-matrix formalism for low energy resonance reactions was introduced by Wigner and Eisenbud [131]. The phenomenological R-matrix was, subsequently, developed by Lane, Thomas [79] and Brune [109] to describe the low energy reaction cross section efficiently in terms of a small set of parameters. The details of the variants of R-matrix formalism is given in the review work of Descouvemont and Baye [107].

In the R-matrix formalism, within each channel, the configuration space is divided into two distinct regions - an internal and an external region separated by a channel radius r_c. The internal region corresponds to the compound nucleus (A) in a single volume. The external region consists of two particle 'channels' with the particles in the pair having A_1 and A_2 (such that $A_1 + A_2 = A$) nucleons, respectively in their own nuclear volumes. The

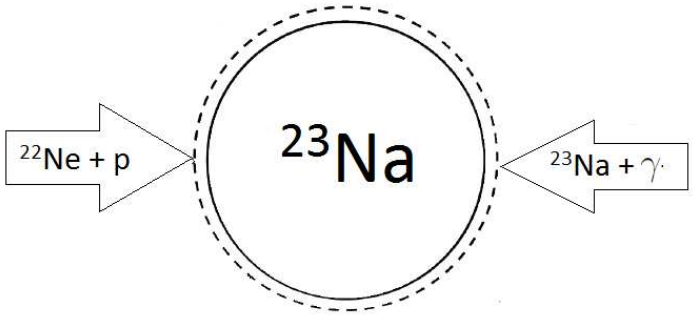

Figure 3.11: The R-matrix formalism of a low energy nuclear reaction system separated (dashed line) into internal and external regions. The radius of this boundary is just larger than nuclear radius.

boundary between the two regions is so chosen that the strong nuclear force is negligible outside this radius (r_c) and thus beyond r_c only the well known Coulomb interaction is to be considered. The compound nucleus, formed through a particular channel (c) defined by a particle pair, can decay through several available exit channels (c'), each having its own configuration space. A schematic representation is shown in Fig. 3.11.

In R-matrix theory is essentially a boundary matching theory. The external wavefuntion, based upon the well known Coulomb wave functions, is matched at the channel radius to an unknown internal wavefunction. The internal wave function is modeled with a set of formal states in the nucleus [79] that have definite angular momentum and satisfy arbitrary boundary condition,

$$\psi_c = \sum_{\lambda} C_\lambda \chi_\lambda \tag{3.11}$$

The formal states (χ) are labeled by λ with C_λ giving the contribution of each formal state. Each internal state is assigned an energy eigenvalue E_λ, which is linked to the observed resonance energy E_R. Each state is also assigned a set of amplitudes $\gamma_{\lambda c}$, which are linked to the observed partial widths, one for each channel c (Γ_c).

Hence, one can construct the R-matrix in terms of levels of the nucleus and all entrance and exit channels.

$$R_{cc'} = \sum_{\lambda} \frac{\gamma_{\lambda c}\gamma_{\lambda c'}}{E_\lambda - E} \tag{3.12}$$

which is defined for each partial wave and has a matrix element for each channel pair.

Now, in the external region of the system, the complete wave function can be expressed as the combination of the incoming and outgoing waves, I and O, which depend on the Coulomb wave functions F and G [111]. This eventually allows the radial part of the external wave function to be expressed as:

$$\phi_c = \frac{1}{v_c^2}\left(A_c I_c - \sum_{c'} U_{cc'} A_{c'} O_c\right) \tag{3.13}$$

Where $U_{cc'}$ is the collision matrix, on which the cross-section of the corresponding channel strongly depends and A_c is the amplitude of the incoming wave in the channel c.

In the internal part, the radial wavefunction can be expressed in terms of eigenstate wavefunctions at the boundary surface as [124]

$$\phi_c(r = r_c) = \left(\frac{\mu_c r_c}{\hbar^2}\right)^{1/2} \sum_{c'} R_{cc'} \left(\frac{\hbar^2}{\mu_{c'} r_{c'}}\right)^{1/2} [\rho_{c'}\phi'_{c'} - B_{c'}\phi_{c'}] \tag{3.14}$$

where μ_c represents the reduced mass, $\rho_c = k_\alpha \mathrm{r}_c$, k_α is the wave number corresponding to particle pair α in channel c ($c = \alpha ls$ where l is the angular momentum of relative motion in the channel and s is the channel spin). The prime denotes the derivative with respect to $k_\alpha r$. B_c represent the boundary conditions of the theory that come from the logarithmic derivatives with respect to r of an eigenstate evaluated at $r = r_c$..

By varying the parameters E_λ and $\gamma_{\lambda c}$, constructed from the observed energy and partial width of the resonances, the experimental cross-sections for each incoming and outgoing channels are fitted. The collision matrix $U_{cc'}$ for the transition $c \to c'$, can be obtained in terms of R-matrix elements by matching the logarithmic derivative of the wavefunctions

of internal and the external regions at the boundary surface.

The collision matrix $U_{cc'}$ and the transition matrix $T_{cc'}$ are related via

$$T_{cc'} = e^{2i\omega_c}\delta_{cc'} - U_{cc'} \tag{3.15}$$

where ω_c is the Coulomb phase shift. The angle-integrated cross cross-section for a reaction going from α to α' with considering J dependence is written as

$$\sigma_J^{\alpha,\alpha'}(E) = \frac{\pi}{k^2}\frac{2J+1}{(2J_t+1)(2J_p+1)}\sum_{I,ll',l'}|T_{c,c'}|^2 \tag{3.16}$$

and total cross-section is

$$\sigma_{c,c'}(E) = \sum_J \sigma_J^{\alpha,\alpha'}(E) \tag{3.17}$$

Here, J_i is the spin of nucleus i, I is the channel spin, and l is the relative orbital angular momentum of the colliding particle in initial channel.

The parameters of R-matrix formalism, *viz*, the pole energy E_λ and reduced widths γ_λ^2 are connected to the physical quantities like the resonance energy and width but can not be obtained directly from experiment. Also the formal R-matrix parameters depend on the channel radius.

In case of an isolated resonance in l-th partial wave, the observed reduced width γ_{obs}^2 is related to the resonance width as

$$\Gamma_R = 2\gamma_{obs}^2 P_l(E_R) \tag{3.18}$$

The formal reduced width parameter for a single pole in R-matrix formalism is obtained from the observed quantity by the relation

$$\gamma_1^2 = \gamma_{obs}^2(1 - \gamma_{obs}^2 S_l'(E_R))^{-1} \tag{3.19}$$

while the pole energy E_1 is given as

$$E_1 = E_R + \gamma_{obs}^2 S_l(E_R) \tag{3.20}$$

The function $S_l(E)$ is termed as the *shift function* related to the logarithmic derivatives of ingoing and outgoing waves. It gives a measure of the shift in the resonance energy with respect to the pole energy. This weak energy dependent function also depends upon the channel radius. The expressions are further generalized for multiples poles in the formalism.

3.3.4 R-Matrix Approach To Radiative Capture

The total radiative capture cross-section populating the ground and excited states of the residual nucleus is given by [112]

$$\sigma(E) = \sum_{J j_n} \sigma_{J j_n}(E) \tag{3.21}$$

where J is the total angular momentum of the colliding particles, j_n is the spin of the n th bound state in residue, and

$$\sigma_{J j_n}(E) = \frac{\pi}{k^2} \frac{2j_n + 1}{(2J_t + 1)(2J_p + 1)} \sum_{I,l} |U_{IlJj_n}|^2 \tag{3.22}$$

as $T_{cc'}$ = - $U_{cc'}$ for reaction channel. Here, J_i is the spin of nucleus i, I is the channel spin, and l is the relative orbital angular momentum of the colliding particle in initial channel. In R-matrix approach this collision matrix has been divided taking into account the contributions from resonance and direct capture part [112, 79, 113]

$$U_{IlJj_n}(E) = U^R_{IlJj_n}(E) + U^{(DC,M_\lambda)}_{IlJj_n} \tag{3.23}$$

The resonance part of the collision matrix describing particle capture into the resonance level λ with spin J and with the subsequent decay of this resonance into the bound state with quantum numbers j_n is given in the standard multi-level R-matrix approximation by

[79]

$$U^{R}_{IlJj_n}(E) = \exp -i\delta_l \frac{\sqrt{\Gamma_p \Gamma_\gamma}}{E_\lambda - E - i\Gamma_\lambda/2} \tag{3.24}$$

The radial direct capture part of the collision matrix for n th bound sate is written as [114]

$$U^{(DC,M_\lambda)}_{IlJ} \propto \sqrt{S_{Il_n j_n}} \int_0^\infty \varphi_{l_n,J_n}(r) r^{\ell+2} \, \psi_{l,k}(r) dr \tag{3.25}$$

Where $S_{Il_n j_n}$ is spectroscopic factor of the target + projectile configuration for a given bound state of the composite nucleus, ℓ is the multipolarity of the transitions, $\varphi_{l_n,J_n}(r)$ is the bound state wave function, $\psi_{l,k}(r)$ is the scattering wave function for initial channel with l relative orbital angular momentum. In R-matrix formalism, the DC part of the collision matrix is divided as

$$U^{(DC,M_\lambda)}_{IlJj_n} \propto \sqrt{S_{Il_n j_n}} \int_0^{r_c} \varphi^{in}_{l_n,J_n}(r) r^{\ell+2} \, \psi^{in}_{l,k}(r) dr + C_{Il_n j_n} \int_{r_c}^\infty W_{-\eta,l_n+1/2}(2\kappa_n r) r^{\ell+2} \, \psi^{ext}_{l,k}(r) dr \tag{3.26}$$

Where $C_{Il_n j_n}$ is the ANC of the same configuration for which the spectroscopic factor is $S_{Il_n j+n}$. The external term in Eq. (3.25) contains radial integral ranging from channel radius ($\mathrm{r}_c \geq \mathrm{r}_0(\mathrm{A}_p{}^{1/3} + \mathrm{A}_t{}^{1/3})$) to infinity, since the internal term is modeled using R-matrix methods in Refs. [112, 113, 124]. The internal contributions for loosely bound states is almost zero but has some contribution for deeply bound states.

3.4 R-matrix calculation for direct capture in ^{22}Ne$(p,\gamma)^{23}$Na

The low energy behavior of off-resonance astrophysical S-factor for $^{22}Ne(p,\gamma)^{23}Na$ reaction is determined by the direct capture process and a broad sub-threshold resonance at 8664 keV in compound nucleus ^{23}Na [104]. Present work attempts a R-matrix description of the low energy behavior of the off-resonance S-factor through the estimation of direct capture component and the contribution of the sub-threshold state constrained by the extracted asymptotic normalization coefficients (ANC-s) from one proton transfer reaction.

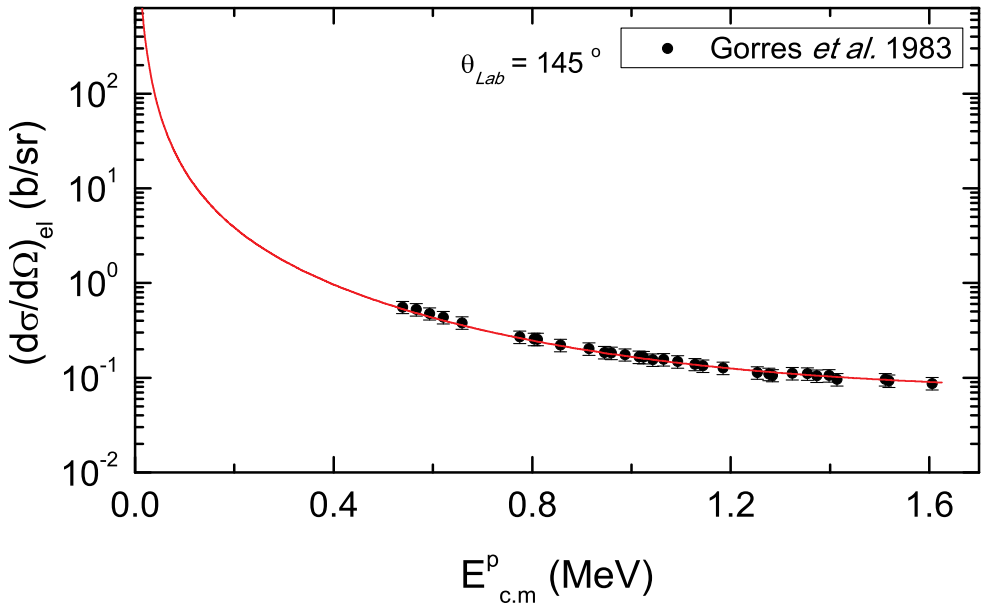

Figure 3.12: *R*-matrix fit to the ^{22}Ne(p, p)^{22}Ne elastic scattering data

The modeling of direct capture in $^{22}Ne(p,\gamma)^{23}Na$ is done using the *R*-matrix code AZURE2 [124] based on the basic theory developed in the seminal works of Lane and Thomas [79] and Vogt [125]. In *R*-matrix modeling, the *channel radius* (r_c) divides the radial space into external and internal parts [79].

Accordingly, the capture cross section is divided into external capture contribution coming from the radial region beyond r_c and internal capture contribution from the region below r_c. The magnitude of the external component of the direct capture cross-section is determined by the ANC of the final bound state [124, 126, 107]. The internal capture component of the direct or non-resonant contribution, on the other hand, is simulated by the high energy background states in the composite nucleus [127]. Thus the direct capture part of the cross-section is modeled as a sum of external capture component and the contribution from high energy background to account for the internal direct capture poles in AZURE2.

In the present work, we have fitted simultaneously the direct capture data of Rolfs *et al.* [97] and Göress *et al.* [98] along with elastic scattering data of Göress *et al.* [98] A detailed experimental study of nonresonant or direct capture component of the reaction $^{22}Ne(p,\gamma)^{23}Na$ by Rolfs *et al.* [97] reported the measurement of cross sections for the

transitions to six excited states in ^{23}Na and the ground state of ^{23}Na for proton energy varying from E_p = 550 keV to 2 MeV. In a subsequent experiment, Göress *et al.* [98] remeasured the direct capture cross sections elaborately from E_p=550 keV to 1.6 MeV and also deduced the spectroscopic factors of the final bound states from the fit to the capture data. The data from recent low energy direct or off-resonance capture measurements by Kelly *et al.* [103] at E_p= 425 keV and by Ferraro, *et al.* [104] at E_p=188, 205, 250 and 310 keV beam energies have also been included in the *R*-matrix analysis. Ferraro *et al.* provided *S*-factor data for off-resonance capture to the ground state including the contribution of decay of sub-threshold resonance at 8664 keV and the total off-resonance *S*-factor data. The new measurements restricted the *R*-matrix model prediction for low energy *S*-factor data for off-resonance capture in $^{22}Ne(p,\gamma)^{23}Na$.

The channel radius, r_c, is fixed at r_c = 5.5 fm, a value greater than the nuclear radius of $R_N = 1.25 \times (A_p^{1/3} + A_T^{1/3}) = 4.75\ fm$ for ^{22}Ne + p system. Channel radius is not a parameter in *R*-matrix modeling. A value of r_c = 5.5 fm has been chosen based on χ^2 minimization employing a grid search technique keeping the ANC-s fixed but varying the parameters of the background poles. Search has been performed on the total off-resonance *S*-factor data to choose the radius.

To fit the data for direct capture to individual states and the total off-resonant capture *S*-factor simultaneously, we consider $M1$ transitions to states with $J^\pi = 1/2^+$ (s-wave capture), $M1 + E2$ transitions to $J^\pi = 3/2^+$, $5/2^+$ (d-wave capture) and $M1$ transition to $J^\pi = 1/2^-$ (p-wave capture) final bound states. The ANC-s for the bound states required for external capture estimates, derived from transfer reaction analysis and listed in Tables 3.2 and 3.4, are kept fixed during the fit to the *S*-factor data. To account for the internal capture component, we introduced the high energy background poles in the *R*-matrix analysis. The poles having spin parity $1/2^+$, $1/2^-$, $3/2^-$ are included and only the $E1$ decay of the background states has been considered. This number of background poles is found to be minimum to obtain a simultaneous fit to the data set considered. The poles are placed at an excitation energy of 15 MeV [127]. The proton partial width of the poles is fixed at Γ_p = 5 MeV and it is within the estimated Wigner limit [17] for particle widths at that excitation. However, Γ_γ values of the background poles are left as free parameters with

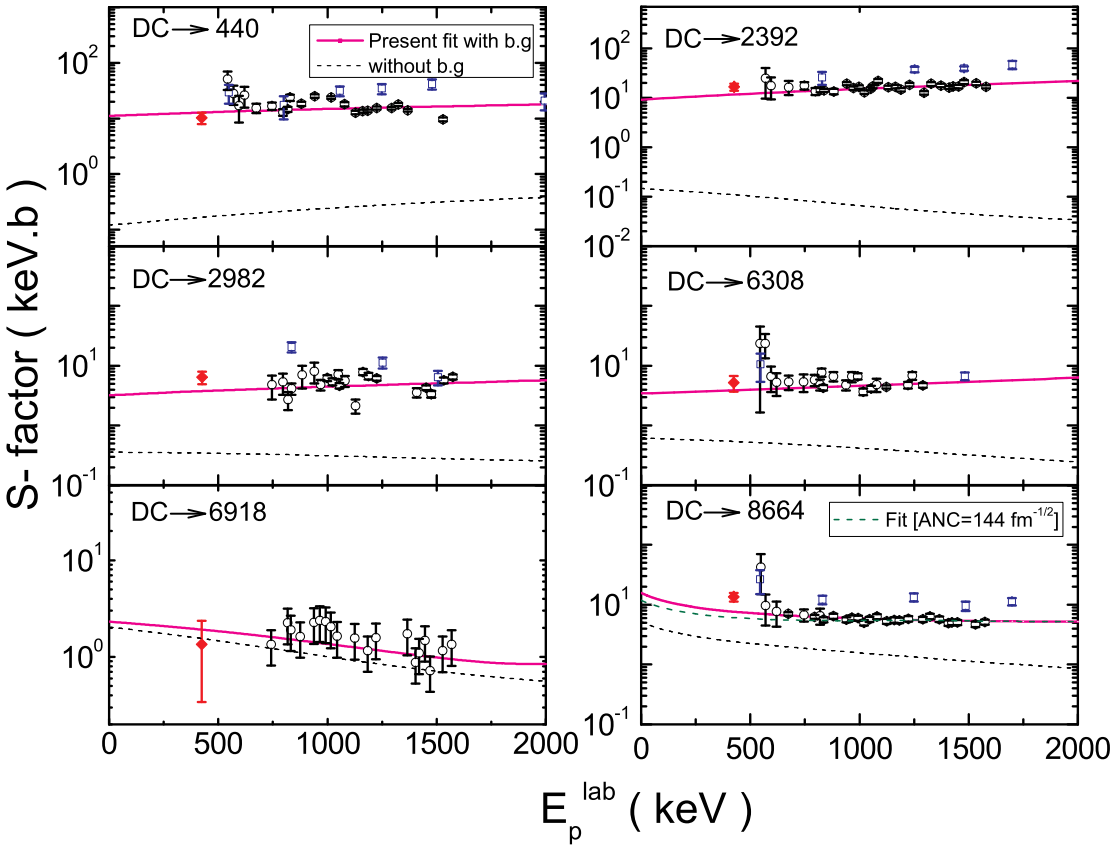

Figure 3.13: *R*-matrix fit to the *S*-factor curve for direct capture to six bound states of ^{23}Na. The red solid curves are the *R*-matrix fits with the contribution of background poles while the dashed curves represent the calculation without the background poles. The panel showing the *S*-factor curve for DC→8664 keV sub-threshold state also includes the *R*-matrix fit (green dashed) with ANC value fixed from transfer reaction calculation. The solid curve in this panel depicts the *R*-matrix fit with ANC value of 166 fm$^{-1/2}$ for the state.

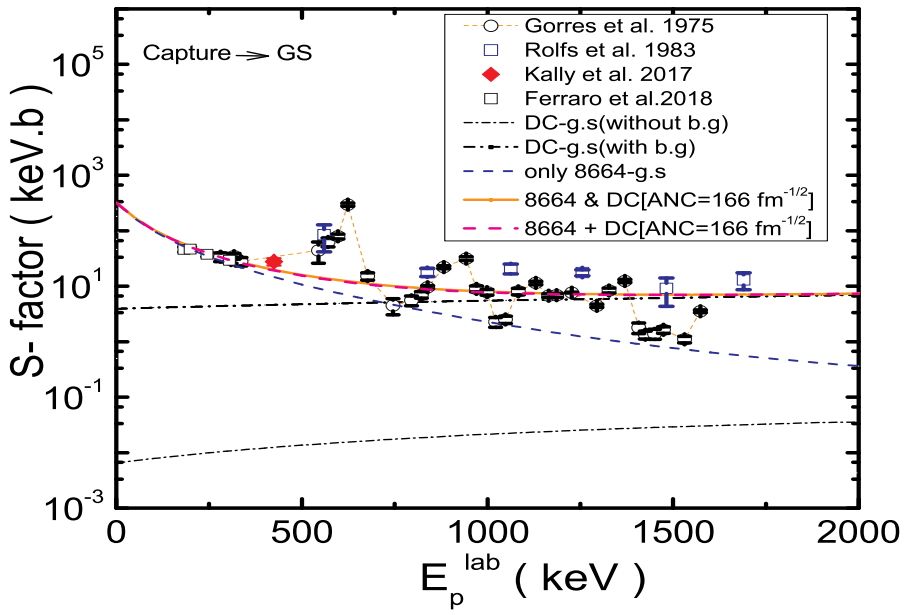

Figure 3.14: *R*-matrix fit to the data of direct capture to the ground state of ^{23}Na

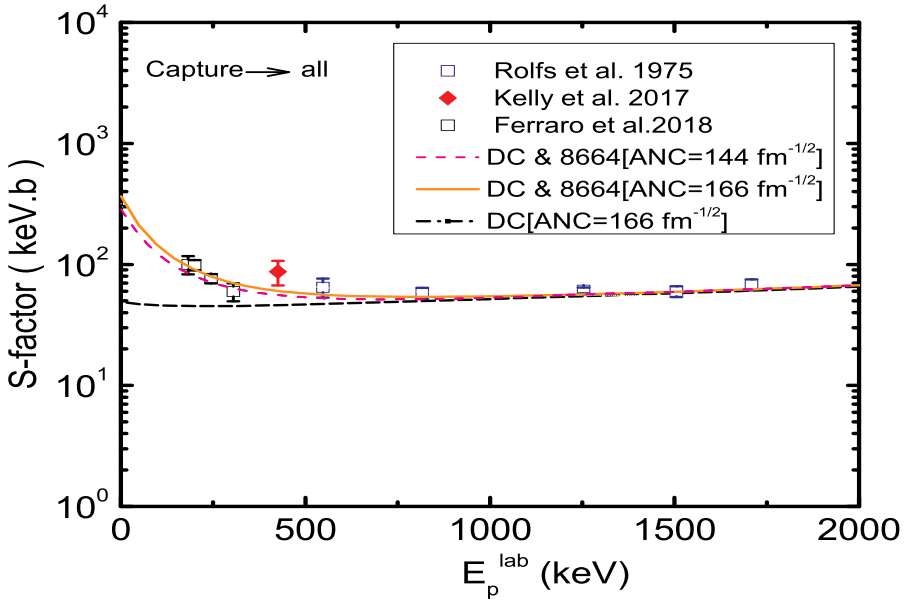

Figure 3.15: *R*-matrix fit to the data of total direct capture in ^{23}Na

the initial value taken from the Weisskopf limit for the corresponding gamma transitions. The fitted background pole parameters are shown in Table 3.6. The resultant *R*-matrix fits to the astrophysical S(E) data for direct capture to excited states along elastic scattering data are shown in Fig. 3.13 and Fig. 3.12 respectively. In Fig. 3.13, the dashed curves represent the contributions of external direct capture to the states. For each state, the external contribution has been estimated by subtracting the contribution of background poles as an internal contribution from the best fit total direct capture cross-section. It is observed that for near-threshold states, the external capture process constitutes almost the whole of the direct capture cross-section [107].

In the last panel of Fig. 3.13, it is observed that a better fit to DC $\rightarrow$ 8664 keV capture data is obtained for ANC of 166 fm$^{-1/2}$ instead of 144 fm$^{-1/2}$ from transfer calculation. The value and its uncertainty have been obtained from a simultaneous best fits, with minimum total χ^2, to DC $\rightarrow$ 8664 keV state, 8664 keV $\rightarrow$ GS, and the total S-factor data. In the multiparameter fit, the background Γ_γ values are kept free while a grid search is performed over the ANC of the state. The corresponding background pole parameters are listed in Table 3.6. The condition of simultaneous fitting has reduced the uncertainty in the ANC value. The enhanced ANC corresponds to spectroscopic factor C^2S = 0.43 for the state compared to the value of 0.32 that yielded ANC = 144 fm$^{-1/2}$ from transfer calculation. The higher spectroscopic factor corroborates well with the value given by Ferraro, *et al.* [104].

In Fig. 3.14, along with the DC $\rightarrow$ GS contribution (black dashed line), we have shown the contribution from the decay of 8664 keV sub-threshold (-130 keV) resonance (blue dashed line). The state decays to the ground state with a branching of (84$\pm$3)% [128] (Γ_γ = 4.7 eV [105]). The orange solid line in Fig. 3.14 represents the result from *R*-matrix fit to total off-resonance capture to the ground state of ^{23}Na. External direct capture to this state has been shown by the black dashed-dotted line in Fig. 3.14. The rise in the low energy S-factor data has been nicely reproduced. No interference effect between the two transitions is observed as the summed contribution (pink dashed line) of individual DC $\rightarrow$ GS and 8664 keV $\rightarrow$ GS coincides with the solid orange line obtained directly. The total S(E) for off-resonance capture in ^{22}Ne(p,γ)^{23}Na obtained by summing all the individual

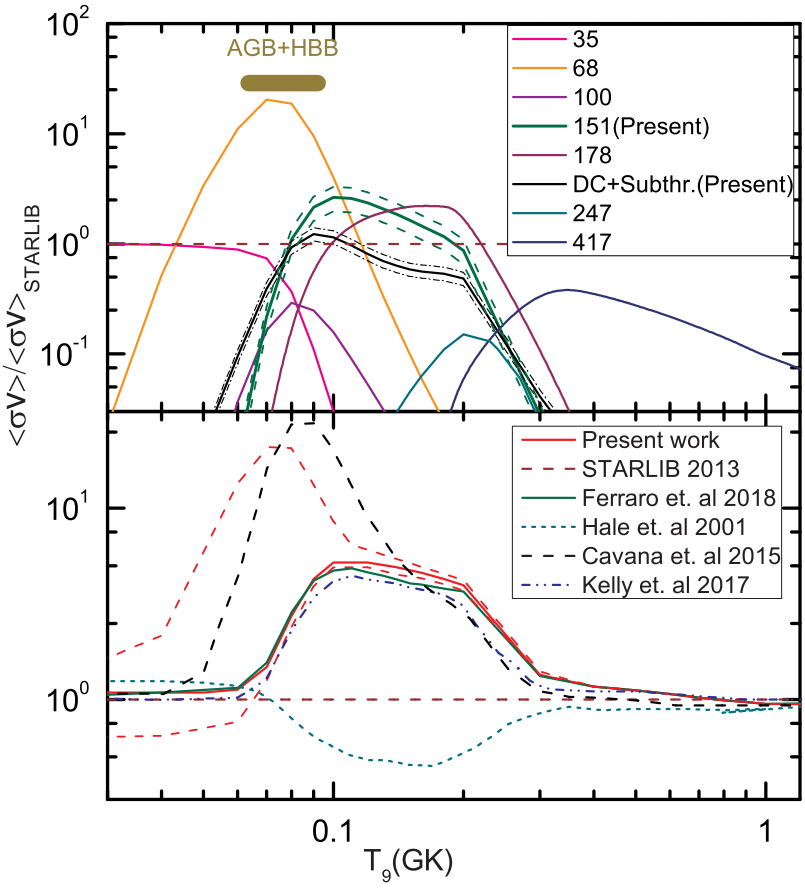

Figure 3.16: Ratio of reaction rate from present calculation to the STARLIB rate for direct and resonant captures in ^{22}Ne(p,γ)^{23}Na reaction. The solid curve represents the ratio with the total capture rate of the reaction.

S(E) functions for transitions to the ground and the excited states are shown in Fig. 3.15. Excellent overall fits to the data sets are obtained.

The total $S^{DC}_{tot}(0)$ value for direct capture contribution is 48.8±9.5 keV.b from the present *R*-matrix calculation. The uncertainty in the value includes the contributions from the variation in r_c, energy location of background poles and uncertainty values of the ANCs added in quadrature. The dominating contribution comes from the uncertainty in the ANC of the 8664 keV sub-threshold state. Also a 10% variation in r_c introduces a variation of 6.24 keV.b in total direct capture *S*-factor. The present value is close to $S^{DC}_{tot}(0)$ = (50±12) kev.b reported by Ferraro, *et al.* [104] but less than the previously adopted value of 62 keV.b [105, 126]. However, the resultant uncertainty from the present estimation is less.

Table 3.7: Summary of resonance strengths ($\omega\gamma$) used in reaction rate estimation.

E_x (keV)	E_r (keV)	$\omega\gamma$(keV)[4] Literature	$\omega\gamma$(keV) Present
8830	35	$(3.6\pm0.2)\times10^{-15}$ [99]	
8862	68	$\leq 6\times10^{-11}$ [104]	
8894	100	$\leq 7.0\times10^{-11}$ [104]	
8945	151	2.7×10^{-7} [104]	$(2.0\pm0.5)\times10^{-7}$
		2.03×10^{-7} [103]	
8944	150	$\leq 9.7\times10^{-8}$ [103]	$(3.93\pm0.9)\times10^{-9}$
8972	178	$(2.7\pm0.2)\times10^{-6}$ [104]	
9000	205.6	$\leq 2.8\times10^{-8}$ [101]	
9042	248.4	$(9.7\pm0.7)\times10^{-6}$ [104]	
9211	417	$(8.8\pm1.02)\times10^{-2}$ [103]	
9252	458	0.5 [129]	

3.5 Thermonuclear reaction rate of ^{22}Ne (p,γ) ^{23}Na.

The thermonuclear reaction rate of ^{22}Ne(p,γ)^{23}Na is controlled by several non-interfering low energy narrow resonances and the total off-resonance capture reaction. The reaction rate for narrow resonance is calculated using the Eq.2.14.

The resonance strengths used in the estimation of reaction rate are listed in Table 6.1. Only the strengths of the doublet states at around E_r = 151 keV have been determined in the present work and the corresponding summed contribution is shown by the green solid line in the figure. In estimating the reaction rate, all the resonance strengths have been divided by the calculated electron screening enhancement factor corresponding to respective excitation energy and tabulated in Table I of Ref.[104]. The rates plotted for E_r = 68 and 100 keV are calculated with only the experimental upper limits of the respective resonance strengths reported by Ferraro, *et al.* [104]. The S_{tot}(E), yielded by the *R*-matrix calculation for total DC plus sub-threshold contribution to the ground state, is used to get the rate for the off-resonant component (black solid line in the upper panel). The uncertainty limits of the off-resonant contribution (black dashed-dot line) are calculated from the total uncertainty in the off-resonant astrophysical S-factor. Individual components are shown in the upper panel of Fig. 3.16. The non-resonant reaction rates have been determined using the code EXP2RATE V2.1 by Thomas Rauscher [130].

The total rate, which is the sum of all individual components, is indicated in Fig. 3.16 by a bold red line in the lower panel of Fig. 3.16. Based on their estimation of the upper limits of 68 and 100 keV resonance strengths, Ferraro, *et al.* assumed that the role of these resonances in the total rate at relevant temperature is insignificant. To compare our total rate in the same temperature window with that of Ferraro, *et al.*, Hale, *et al.* and Cavanna, *et al.*, we estimated the total rate without the contributions of 68 and 100 keV resonances. At around T = 0.1 GK, the present rate is about an order higher than Hale's rate but only slightly higher compared to the rates determined by Cavanna, *et al.* as well as Ferraro, *et al.* For 0.1 GK $\leq$ T $\leq$ 0.2 GK region, the estimated rate is distinctly higher than both the rates. In the T $\leq$ 0.1 GK, our rate is similar to the rate obtained by Ferraro, *et al.*. The associated upper and lower uncertainty limits are shown by the red dashed lines. While calculating the limits for the resonant capture rate, we took into account the uncertainties of the energy locations of states along with respective uncertainties of the resonance strengths. While the upper limits of the strengths of 68 and 100 keV resonances are considered in estimating the upper limit of the total rate, for the lower limit of the total rate the lower limits of the strengths are set to zero [102]. Thus the effect of 68 and 100 keV resonances is included in the uncertainty region of the total rate bounded by the red thin lines.

3.6 Conclusion

A consistent analysis of direct capture reaction in ^{22}Ne(p,γ)^{23}Na has been performed within the *R*-matrix framework. constrained with the asymptotic normalization constants of the bound states of ^{23}Na obtained from the transfer reaction calculation. Asymptotic normalization constants have been extracted from finite DWBA analysis of ^{22}Ne(^{3}He,d)^{23}Na transfer data.

Astrophysical S-factor data for capture to the bound states of ^{23}Na have been reproduced from the analysis. Contribution of capture through the sub-threshold resonance at 8664 keV excitation in the total capture to the ground state of ^{23}Na has been delineated. The observed rise in the ground state capture data is reproduced nicely. The total direct capture

S-factor at zero relative energy, $S_{DC}(0)$, is found to be 48.8 ± 9.5 having less uncertainty.

The total reaction rate obtained as a function of temperature differs from the recent estimations by Ferraro *et al.* in the temperature window of 0.1 GK ≤ T ≤ 0.2 GK. The difference is caused due to a slightly higher contribution from direct plus sub-threshold capture to the ground state. However, the present uncertainty in the total rate in this region is relatively higher due to the uncertainty in the resonance strength of the unbound state extracted from transfer angular distribution data. However, in T ≤ 0.1 GK, the uncertainty in the rate is comparable with the result of Ferraro, *et al.*.

Chapter 4

Nuclear level density of ^{69}Zn and ^{68}Zn(n, γ)^{69}Zn capture cross section

4.1 The ^{68}Zn(n, γ)^{69}Zn capture reaction

In nuclear astrophysics, neutron capture reactions play a decisive role in the explaining the origin of elements heavier than iron. The neutron capture reaction ^{68}Zn(n, γ)^{69}Zn capture reaction has the highest impact on ^{68}Zn abundance produced in the weak and enhanced s-process in massive stars. The reaction acts as a poison reaction for the production of ^{68}Zn in the s-process nucleosynthesis path. However, the abundance of ^{68}Zn is now found to have a strong correlation on a single reaction ^{68}Zn(n, γ)^{69}Zn [132]. From a recent compilation of Koloczek [133] for s-process nucleosynthesis, it was found that the abundance of ^{80}Kr is also highly sensitive on ^{68}Zn(n, γ)^{69}Zn capture reaction.

The description of neutron capture reaction relies on statistical model(SM) calculations to determine the astrophysical reaction rate. The Hauser-Feshbach model is used to calculate the reaction cross-section. The model requires the optical model potentials (OMP) for particle transmission coefficients, nuclear level density (NLD) parameter and γ-ray strength function for extraction of γ-ray transmission coefficients [66]. The previous statistical model calculation of ^{68}Zn(n, γ)^{69}Zn capture cross-section considering different NLD prescriptions (Farmi Gas model, Constant Temperature model, microscopic NLD of

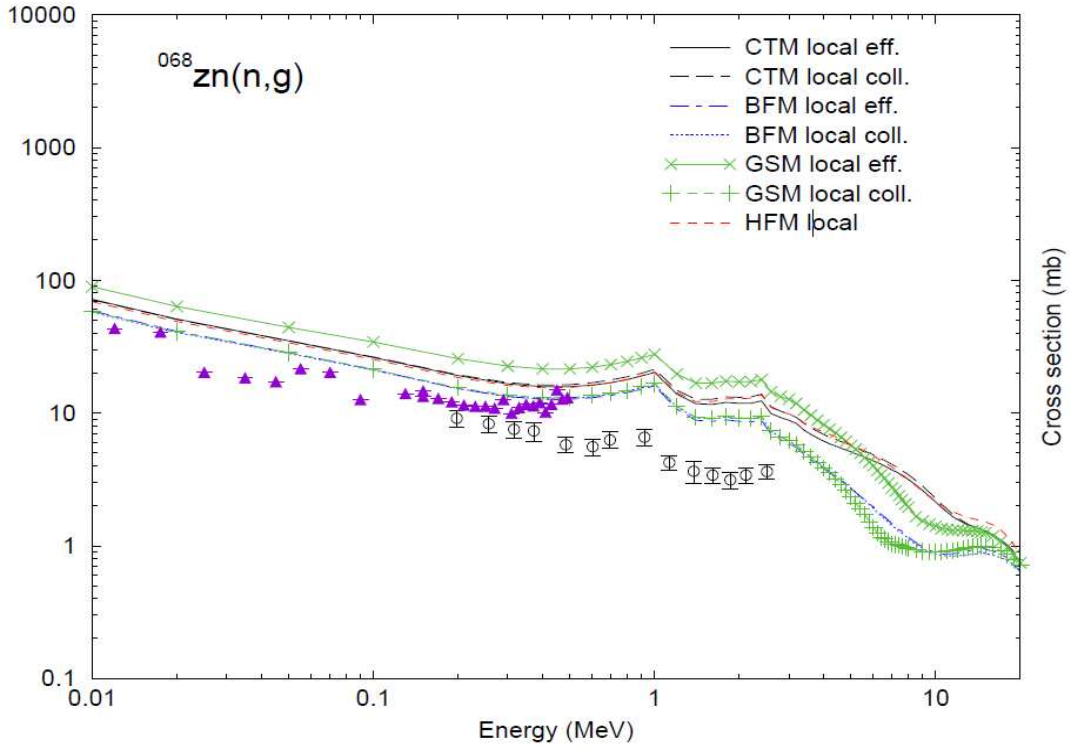

Figure 4.1: (Color online) The comparison of ^{68}Zn(n, γ)^{69}Zn capture data [136] (triangular and circular points) with statistical model calculation considering different NLD prescription(Color line).

Goriely [134]) overestimated the available experimental cross-section data [136] shown in Fig. 4.1. This over prediction motivated us to look into the aspect of extraction of NLD of ^{69}Zn from experiment and use it as input parameter in SM calculation to constrain the model calculation of the ^{68}Zn(n, γ)^{69}Zn capture cross-section.

4.2 The Approach

The approach adopted in this thesis is based on particle-γ coincidence technique, as mentioned in Chap.II, to extract the nuclear level density parameter (NLD) of nucleus ^{69}Zn for describing the neutron capture reaction ^{68}Zn(n, γ)^{69}Zn.

To populate the nucleus ^{69}Zn of interest, we chose the compound nuclear reaction ^{64}Ni(^{9}Be,$\alpha n\gamma$)^{68}Zn reaction. Through the first chance α emission from the compound nucleus ^{73}Ge, i.e., through the evaporation steps ^{73}Ge(α)^{69}Zn(n)^{68}Zn(γ), the population of the intermediate

nucleus ^{69}Zn was investigated. The de-exciting γ rays from the residue ^{68}Zn were used to the alpha evaporation to identify the intermediate nucleus ^{69}Zn. The effect of first chance neutron emission or $n\alpha$ decay channel, populating the same residue ^{68}Zn is discussed in subsequent sections. The approach, thus has two parts.

• Hauser-Feshbach modeling of fusion evaporation reaction to extract the nuclear level density (NLD) of the nucleus of interest, identified through the γ-gated evaporation particle spectrum. Here the γ-s of the residue ^{68}Zn is used to gate the first chance evaporation α particle spectrum to obtain the NLD of nucleus ^{69}Zn.

• Hauser-Feshbach modeling of ^{68}Zn(n, γ) capture reaction cross section for production of the nucleus ^{69}Zn of interest, using the extracted NLD from the previous step as an input parameter.

In this work, since the statistical model has been used extensively, we have presented the essential mathematical relations of the model in the following section.

4.3 Statistical model calculation for fusion evaporation reaction

In the statistical model, the main assumption is that a compound nucleus is formed with excitation energy high enough so that many states may be excited by the interaction of projectile nucleons with the target nucleons. Moreover, before the decay process takes place all the degrees of freedom(mass, Energy, Angular momentum) reach the equilibrium. The equilibrated compound nucleus, following Bohr's hypothesis, decays without remembering the way it has been formed in the entrance channel except for the conserved quantities such as excitation energy, Angular momentum, parity, isospin.The compound nucleus mainly decays via particle (n, p and α) evaporation or γ-emission.

4.3.1 CASCADE: statistical model calculation code

CASCADE is a statistical model code for the decay of a compound nucleus populated in a nuclear reaction. Originally, it was developed by Puhlhofer in 1977 [135] and with time,

different scientific groups have modified, revised, and improved the original code for their own need. The code is based on Hauser-Feshback formalism of the statistical decay of the compound nucleus. This code actually calculates the CN decay probabilities where the exited CN is characterized by an initial excitation energy(E*) and a distribution of angular momenta (J) in the form of (E*, J) matrix. For each matrix element, the neutron, the proton, α, γ, and fission probabilities are calculated and the corresponding populations go to new (E*, J) matrices. This process is continued until the exited nucleus reaches below the particle threshold energy. Below the particle threshold energy, the compound nucleus emits the statistical γ-ray in between particle threshold and the yrast line and go to another (E*, J) matrix and finally, it is finished off by the subsequent emission of low energy discrete yrast γ-ray. Based on the initial population, the code calculates the energy spectra for evaporated neutron, proton, α, and γ-rays. There are two main ingredients in the statistical model calculation- the decay probability, and the nuclear level density (NLD).

4.3.2 Decay probabilities

A compound nucleus populated at high excitation energy and angular momentum, decays via particle (mainly n,p,α) or γ-ray emission. The particle emission probability is generally determined by the statistical weight of the initial and final states and transmission coefficients (barrier penetrability) using the reciprocity theorem. The decay rate R_p for emitting a particle p from an exited nucleus i (at excitation energy E_i, spin J_i, parity π_i) to form a daughter nucleus f (at E_f, J_f, π_f) is given by [137]:

$$R_p d\epsilon = \frac{\rho_f(E_f, J_f, \pi_f)}{2\pi\hbar\rho_i(E_i, J_f, \pi_i)} \sum_{S=J_f-s_p}^{S=J_f+s_p} \sum_{L=J_i-S}^{L=J_i+S} T_L^p(\epsilon_p) d\epsilon_p \tag{4.1}$$

Where ϵ_p is the kinetic energy of particle p. B_p s_p, and L are binding energy, spin, and orbital angular momentum of the emitting particle, respectively. ρ_i and ρ_f are the level densities of the initial and final states of the nuclei. T_L^p is the transmission coefficient for a particle of energy ϵ_p. The particle transmission coefficients are calculated by solving

the optical model equations of the nuclear system. In the present study we are looking at evaporated alpha particle. The optical model potential parameters for the alpha transmission coefficient are taken from Refs.[138].

4.3.3 Nuclear level density

The basic nuclear level density formula, which is widely used in statistical model calculation, derived from the Fermi gas model, based on the pioneering work of Bethe[139] is given by

$$\rho(E^*, J) = \frac{2J+1}{12\theta^{3/2}}\sqrt{a}\frac{exp(2\sqrt{aU})}{U^2} \tag{4.2}$$

where, U=E*$-\frac{J(J+1)}{\theta}$$-S_\alpha$$-\Delta$P, θ=$\frac{2I_{eff}}{\hbar^2}$, with I$_{eff}$, S$_\alpha$ and ΔP being the effective rigid-body moment of inertia, partile, here it is α separation energy and pairing energy, respectively. Ignatyuk prescription [140] of level density parameter a, which takes into account the shell effects as a function of excitation energy, is adopted and it is expressed as

$$a = \tilde{a}[1 + \frac{\delta S}{U}[1 - \exp(-\gamma U)]] \tag{4.3}$$

where, $\tilde{a}$ = A/k and k is inverse level density parameter. δS is ground-state shell correction defined as the difference of the experimental and theoretical (liquid drop) masses. γ^{-1} = $\frac{0.4A^{4/3}}{\tilde{a}}$ is the rate at which the shell effect is damped with the increase in excitation energy. The moment of inertia of the CN is taken as $I_{eff} = I_0(1 + \delta_1 J^2 + \delta_2 J^4)$, where I_0(= $\frac{2}{5}MA^{5/3}r_0^2$) is the moment of inertia of a spherical nucleus. δ_1 and δ_2 are the deformability parameters, r$_0$ is the radius parameter and J is the total spin of the nucleus.

4.3.4 Hausher-Feshback modeling of (n, γ) capture reaction

The description of neutron capture reactions relies on statistical model calculations to determine the astrophysical reaction rate. The Hauser-Feshbach model is used to calculate the reaction cross-section. The model requires the optical model potentials (OMP) for particle transmission coefficients, nuclear level density (NLD) and gamma-ray strength

function for extraction of γ-ray transmission coefficients [66] of the composite nucleus after neutron capture.

Optical model potential

The optical model is that the complicated interaction between an incident particle and a nucleus can be represented by a complex mean-field potential, which divides the reaction flux into a part covering shape elastic scattering and a part describing all competing non-elastic channels. Solving the Schrodinger equation numerically with this complex potential yields a wealth of valuable information. First, it returns a prediction for the basic observable, namely the elastic angular distribution and polarization, the reaction and total cross-section and, for low energies, the s, p-wave strength functions and the potential scattering radius R'. The s, p-wave strength functions are used to calculate the formation cross-section of the compound nucleus.

γ-ray strength function

Gamma-ray transmission coefficients are important for the description of the gamma emission channel in nuclear reactions. This is an almost universal channel since gamma rays, in general, may accompany the emission of any other emitted particle. Like the particle transmission coefficients that emerge from the optical model, gamma-ray transmission coefficients enter the Hauser-Feshbach model for the calculation of the competition of photons with other particles. The gamma-ray transmission coefficient for multipolarity l of type X (where X = M or E) is given by

$$T_{Xl}(E_\gamma) = 2\pi f_{Xl}(E_\gamma) E_\gamma^{2l+1}, \tag{4.4}$$

where E_γ denotes the gamma energy and $f_{Xl}(E_\gamma)$ is the energy-dependent gamma-ray strength function. Different models were used for gamma-ray strength function. In the present calculation, we use the Brink-Axel option for all transition types other than E1. For E1 radiation, the default option used in TALYS is the generalized Lorentzian form of

Kopecky and Uhl[141].

$$f_{E1}(E_\gamma, T) = K_{E1}[\frac{E_\gamma \Gamma_{E1}(E_\gamma)}{(E_\gamma^2 - E_{E1}^2)^2 + E_\gamma^2 \Gamma_{E1}^2(E_\gamma)} + \frac{0.7\Gamma_{E1} 4\pi^2 T^2}{E_{E1}^3}]\sigma_{E1}\Gamma_{E1}, \tag{4.5}$$

where the energy-dependent damping width Γ_{E1} is given by

$$\Gamma_{E1}(E_\gamma) = \Gamma_{E1}\frac{E_\gamma^2 + 4\pi^2 T^2}{E_{E1}^2} \tag{4.6}$$

and T is the nuclear temperature given by[142]

$$T = \sqrt{\frac{E_n + S_n - \Delta P - E_\gamma}{a(S_n)}} \tag{4.7}$$

where S_n is the neutron separation energy, E_n the incident neutron energy, ΔP the pairing correction (see the Section on level densities) and the level density parameter at S_n.

4.4 Experimental Details

An experiment was performed at BARC-TIFR Pelletron Linac Facility Mumbai, India in June 2018. A self-supporting ~99 % enriched metallic ^{64}Ni was used as the target in the experiment. The target was of thickness about 507 ± 10 μg/cm^2 thickness from Oak Ridge National Laboratory, USA. The thickness of the target was checked previously [143] with charge particle energy loss technique. A beam of ^{9}Be particle at 30 MeV was incident on the ^{64}Ni target populating the compound nucleus ^{73}Ge at 41.8 MeV excitation energy.

4.4.1 Detector setup and data acquisition

The detector setup consists of two major detector systems which are given below:

• The CsI(Tl) detector for detecting evaporated light charged particle (α, proton) from the compound nucleus (CN).

Table 4.1: Orientation of the detectors in INGA array.

Pocket No.	Distance from target (in cm)	Polar angle (θ) (in deg.)	Azimuthal angle (ϕ) (in deg.)
1	25	157	0
2	25	157	120
3	25	157	240
4	25	140	60
5	25	140	180
6	25	140	300
7	25	115	150
8	25	115	270
9	25	90	120
10	25	90	180
11	25	90	240
12	25	90	300
13	25	40	60
14	25	40	300

• The INGA set up [144] for detecting de-exciting discrete γ-rays from the residual nucleus.

The geometry of the INGA array was spherical and capable of placinga maximum of 24 clover detectors. The radial distance of the clover detectors crystal from the target center is 25 cm. The orientation of the clover detectors in the present experiment have been listed in Table 4.1. Within this array, a small spherical chamber of diameter 20 cm was placed to mount CsI(Tl) detectors and target frames respectively shown in the right panels of Fig. 4.2. Eight CsI(Tl) detectors, each of thickness 3 mm (size 15x15 mm^2), were used to detect the outgoing charged particles. Two sets with four detectors combination each were placed symmetrically about the beam axis at 5 cm from the target center. The detectors were put on both sides of the beamline covering an annular region from 22° to 67° in the reaction plane. Tantalum absorbers of thickness 30 mg/cm^2 were used before the CsI(Tl) detectors to stop the elastically scattered particles from entering the detectors. The INGA γ-detector setup consisting of 14 Compton-suppressed Clover detectors arranged in five angles, with two at 40°, four at 90°, two at 140°, two at 115°and four at 157° with respect to the beam direction. The picture of the detector set up has been shown in Fig 4.2.

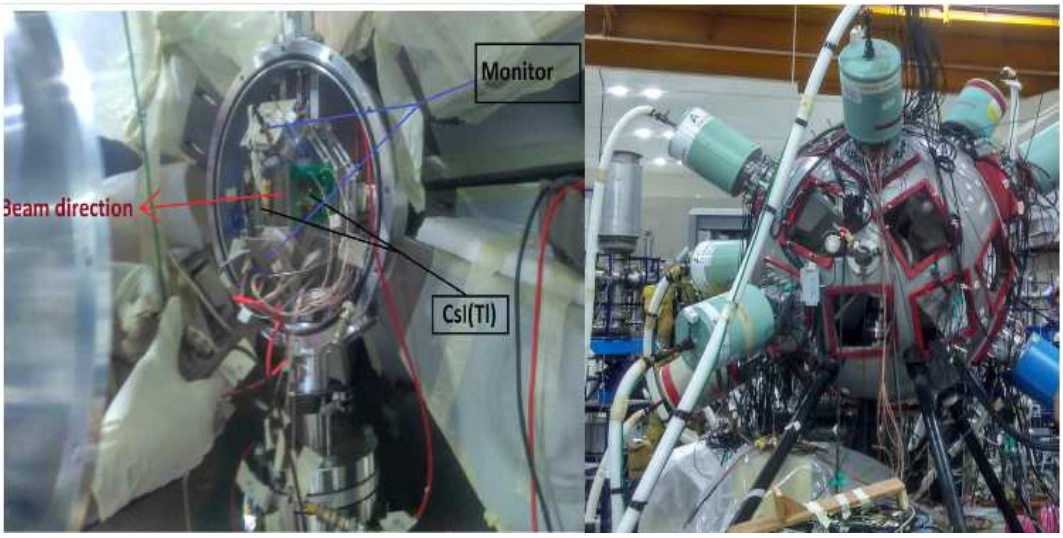

Figure 4.2: Picture of detector set up at TIFR-BARC Pelletron Linac Facility.

Data were recorded in list mode in a digital data acquisition system (DDAQ) based on Pixie-16 modules of XIA-LLC, which provided both energy and timing information. This system has capable of the digitization of 96 channels of 24 Clover detectors and 16 channels of 16 CsI(Tl) with a 100 MHz sampling rate. It can operate both in trigger-less as well as multi-fold coincidence mode. The BGO signals from the anti-Compton shields of the respective clovers were used for vetoing the individual channels. Time-stamped data were collected event by event in singles mode. The pulse shape parameters of CsI(Tl) detectors (i.e; short gate integrated charge and long gate integrated charge) were also recorded for particle identification.

4.4.2 Data analysis

The raw data were sorted using the Multiparameter time-stamped based coincidence search program (MARCOS) [145] to generate the data in Radware and root compatible format for further analysis. Initially, from the sorted data, we calibrated the clover and the CsI(Tl) detectors independently.

Clover Detector Calibration

The energy of the incident γ-rays are digitized in the Analog to Digital Converter (ADC) for each HPGe crystal of clover detectors, where the channel number of ADC is proportional (if there is no offset) to the energy of the incident γ-ray. Generally, the gain of each crystal of the clover detector is different. For that reason, the correlation between the channel and the energy has to be established using known radioactive sources. We have used ^{152}Eu and ^{133}Ba standard sources for energy calibration. The γ-ray energy for ^{152}Eu and ^{133}Ba sources were plotted against the channel numbers and fitted with a quadratic equation.

$$E(keV) = a_0 + a_1 \times x + a_2 \times x^2 \tag{4.8}$$

where x is channel number, a_i-s are calibration constants. A comparison of the gain matched spectrum with their respective raw spectrum of the four crystals ofclover is shown in Fig. 4.3. From Fig. 4.3 it is clearly observed that after gain matching the energy peaks of four crystals overlay on each other justifying the calibration.

Add-back mode: Add the energy spectrum of each crystal of a clover detector due to photoelectric absorption it adds only photo peaks counts only. In addition, if we add the correlated events in the two adjacent crystals then the events which are Compton scattered from one crystal and get absorbed in the adjacent crystal also contribute to the full energy peak. So, the full energy peak now contains the photoelectric events of all four crystals and also part of the Compton events. This is known as an add-back mode. A comparison of add and add-back spectrum of one clover is shown in Fig. 4.4 for the Eu and Ba decay line. We also calculate the add-back factor for $E_\gamma \approx 82$ to 1408 keV region. The add-back factor is basically the ratio of add-back counts and sum photopeak counts. It is clearly observed from Fig. 4.5 that a low energy factor is closed to one as expected. The factor then starts increasing with increasing γ-ray energies, because at these moderate energies, the probability of Compton scattering becomes comparable with the photoelectric effect and the add-back mode starts contributing.

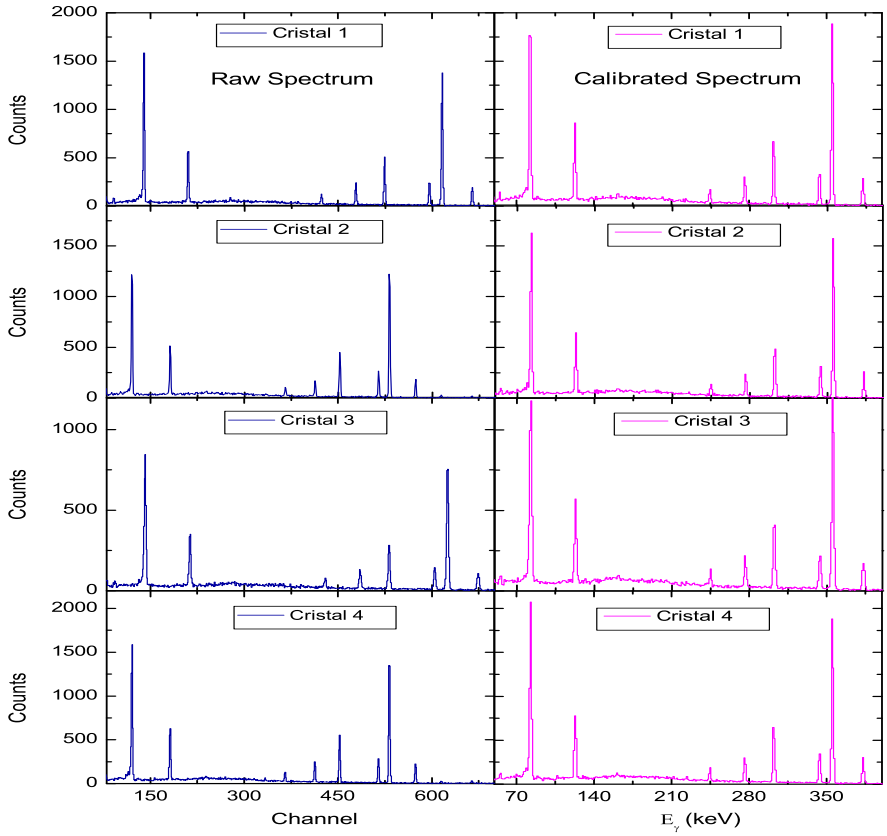

Figure 4.3: A comparison of the calibrated spectrum with their respective raw spectrum of the four crystals of a clover for ^{152}Eu and ^{133}Ba sources.

Particle identification using CsI(Tl) Detector

As mentioned earlier that during the online experiment we recorded two-plus shape parameters of CsI(Tl) signals. 1) Integrated charge in the time interval from t=0 to t_{max} call short gate. Where t_{max} is a time at which signals height is maximum.
2) Integrated charge in the time interval from t=0 to ∞ call long gate.

Now we plot a 2D spectrum Q_{long} vs. Q_{short} . From this 2D spectrum we observed that α, proton bands are clearly separated shown in Fig. 4.8. We also take data for ^{229}Th source also and generate the same QDC spectrum shown in Fig. 4.6. The peak positions of α energy for ^{229}Th sources were plotted against the channel numbers of Q_{long} and fitted with quadratic equation shown in Fig. 4.7. Now calibrate QDC channels into the energy of online data using quadratic equations for α-particles.

the coincidence matrix between CsI(Tl) and clover detector event. Finally, save this coin-

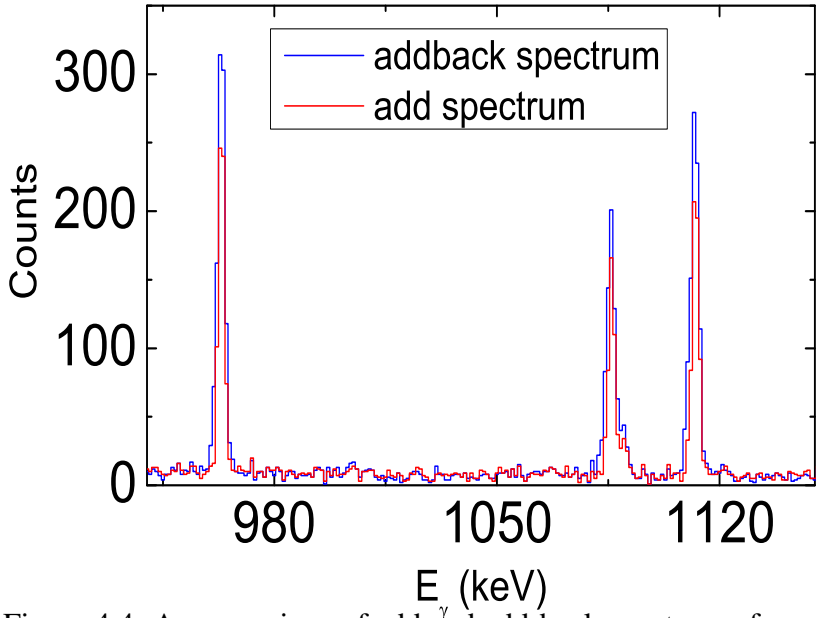

Figure 4.4: A comparison of add and add-back spectrum of one clover.

cidence event into a root file format. Further data analysis has been done in root software. The α-events of CsI(Tl) detectors were identified from plus shape discrimination technique. Coincidence α-γ events are sorted into a matrix with the α-energy E_α versus the γ energy E_γ as shown in Fig. 4.9. The projected γ-spectra of E_α versus E_γ matrix is shown in Fig. 4.9 and the various transitions of different α channels have been identified. This γ-line are used to extract γ-gated α spectra for a particular residue related to α-decay channel.

4.4.3 Extraction of evaporated α-spectra from CN decay

The main aim of this present work is to extract the NLD of ^{69}Zn and use it to calculate the ^{68}Zn(n, γ)^{69}Zn capture cross-sections. In this section, we discuss the extraction process of NLD from γ-gated α-spectra. While extracting the NLDs from the particle evaporation spectrum, it is to be ensured that the contributions from non-compound processes are negligibly small. This is the pre-requisite for the extraction of the NLD parameter by particle evaporation technique. To select out the purely compound events, the γ-decay (E_γ = 332 and 152 keV of ^{68}Zn) of lowest-lying negative parity states 6^- and 8^- have been chosen

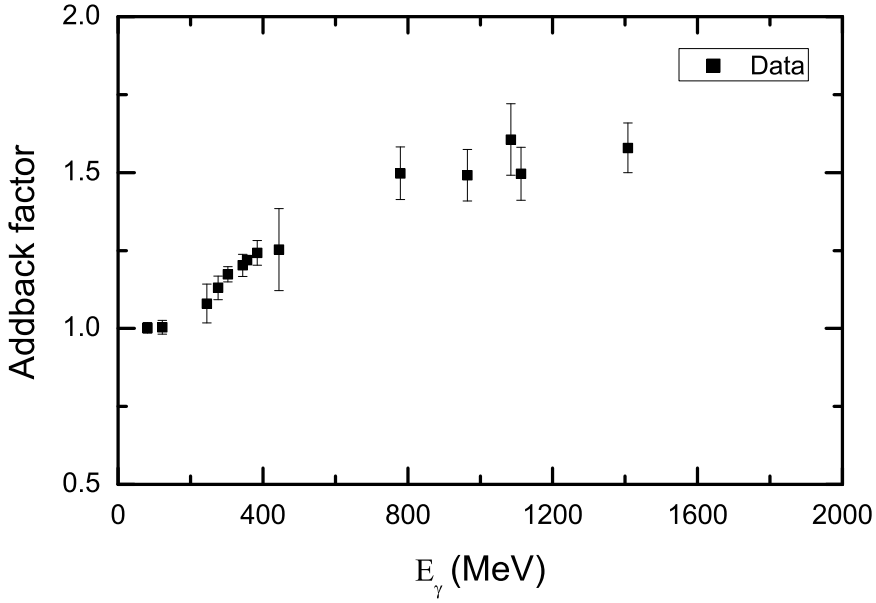

Figure 4.5: The variation of add-back factor with energy of γ-rays.

to gate the α-spectrum. It should be mentioned that the level scheme of ^{68}Zn (as shown in Fig. 4.11) from the γ-γ coincidence matrix of the present experiment also conforms to the level scheme reported earlier in Ref. [146]. The nucleus ^{68}Zn can be produced directly by αn decay of compound nucleus ^{73}Ge or by n emission after incomplete fusion/transfer of ^{5}He fragment from ^{9}Be to ^{64}Ni. Again, ^{68}Zn can also be produced by direct transfer of α fragment of ^{9}Be to the bound excited states of ^{68}Zn. The CN decay can populate the even spin, odd parity 6^- and 8^- states in ^{68}Zn residue. Direct $\alpha(0^+)$ transfer to ^{64}Ni(0^+) can not populate these even spin, odd parity states. In case of transfer of heavier ^{5}He fragment having Q-value of +10.24 MeV, the outgoing α from ^{9}Be will have kinetic energy in the range of 36.0 to 39.5 MeV within the measured angular domain of 22° to 67°. On the other hand, kinematically the energy of break up α corresponding to incomplete fusion of ^{5}He with ^{64}Ni target will lie within 8 to 12 MeV. Thus, in the measured γ-gated α-particle energy spectrum, the contributions of different reaction channels, other than the CN process, beyond 12 MeV kinetic energy will be negligibly small. The γ-gated α-energy spectra are shown in the upper and lower panels of Fig.4.12. The γ-gated alpha energy spectra are converted into the CM frame in order to compare them with the statistical model calculations and carried out to investigate the NLDs as a function of excitation

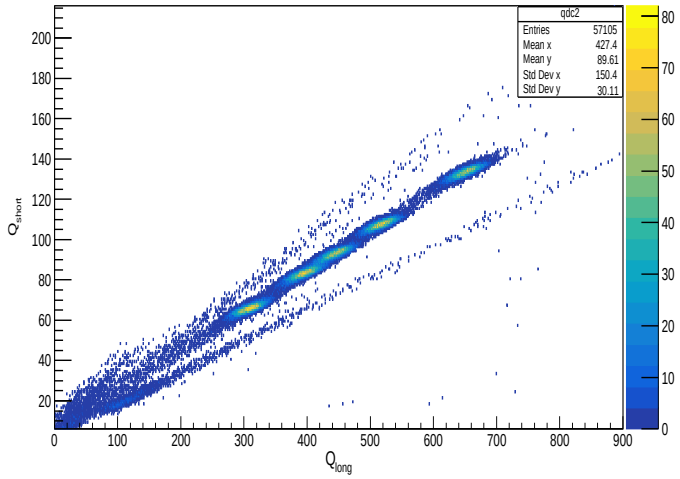

Figure 4.6: (Color online) QDC spectrum of CsI(Tl) for ^{229}Th source.

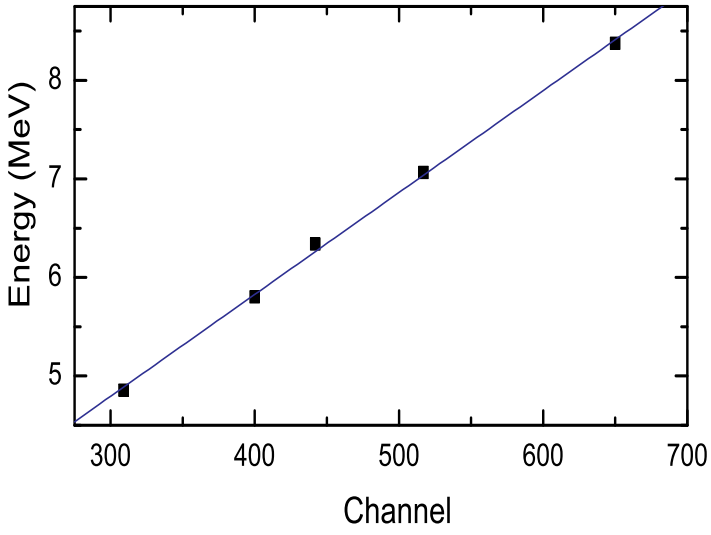

Figure 4.7: (Color online) Calibration curve for a CsI(Tl) detector.

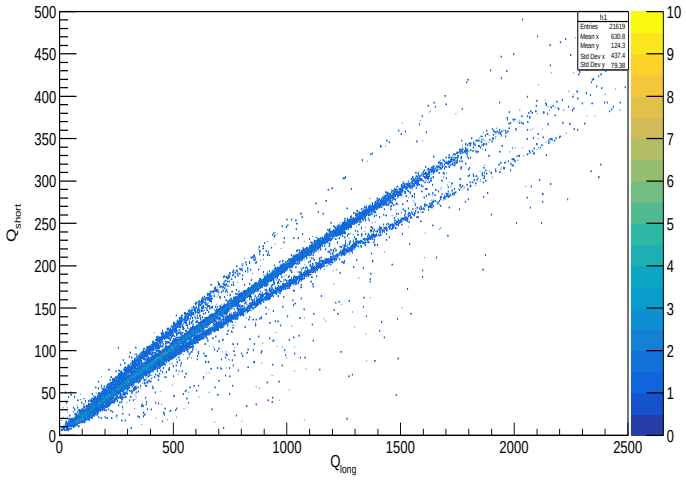

Figure 4.8: (Color online) QDC spectrum of CsI(Tl) for ^{9}Be + ^{64}Ni reaction at 30 MeV.

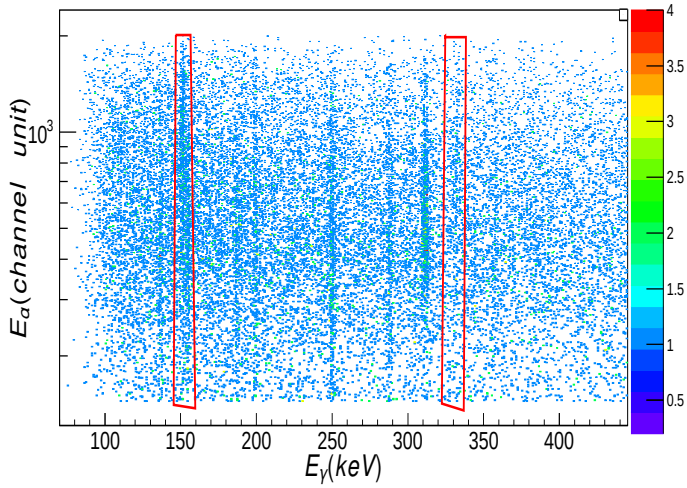

Figure 4.9: (Color online) α-γ coincidence matrix extracted from raw particle-γ matrix. The events of interest are bounded by solid red boxes.

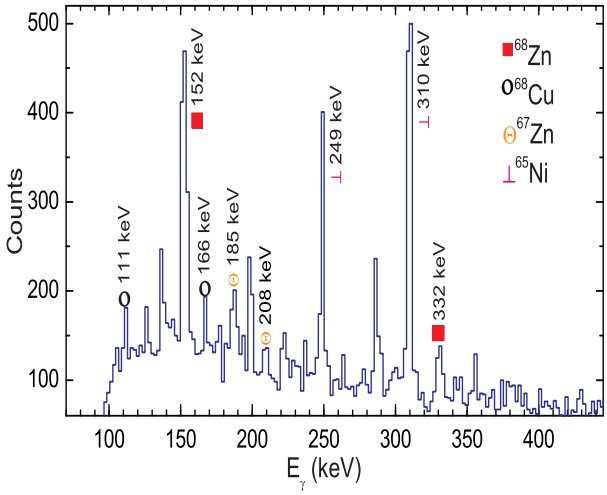

Figure 4.10: Projected gamma energy spectrum from Fig. 4.9. Symbol with γ-energy indicate γ-lines of different residual nuclei associated with α-emitting channels.

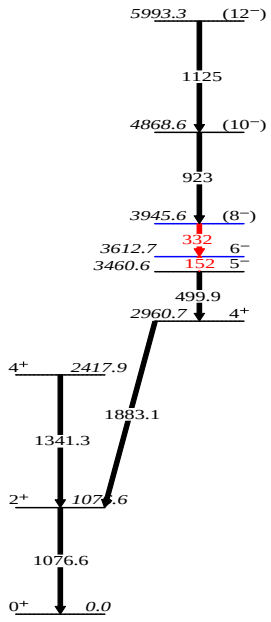

Figure 4.11: Partial level scheme of ^{68}Zn based on its population in the present experiment. Transitions of interest and states shown in red and blue respectively.

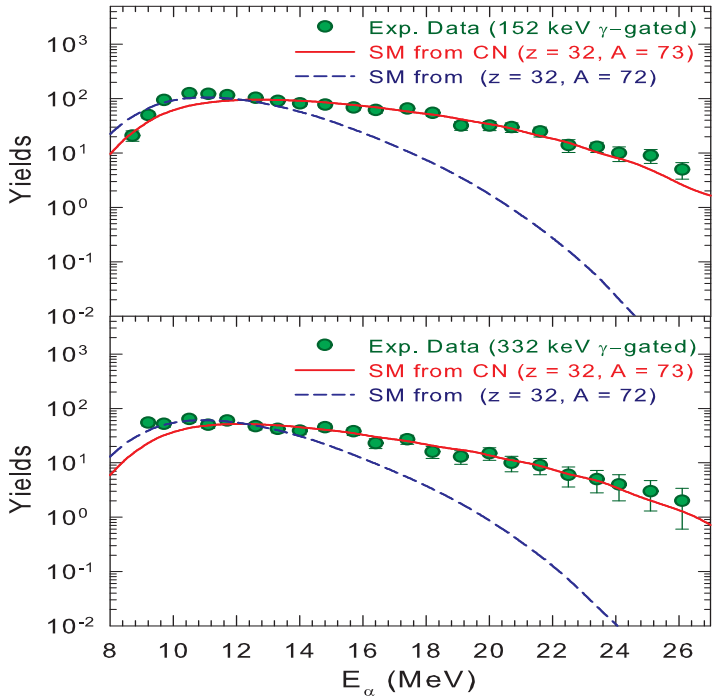

Figure 4.12: (Color online) Filled symbols represent the experimental γ-gated alpha energy spectra. Lines represent the statistical model calculations with CASCADE code. Red continuous line represents spectrum of first chance α decay from compound nucleus ^{73}Ge. Black dashed line represents the contribution of α emission following first step one neutron decay of ^{73}Ge.

energy.

4.4.4 Statistical model calculation and estimation of ^{69}Zn NLD

The statistical model calculations (CASCADE) [135] have been carried out to fit the 152 and 332 keV γ-gated α spectra. The deformability parametersδ_1 (= 2×10^{-6}) and δ_2 (= 2×10^{-8}) are taken in present calculation, r_0 =1.25 fm is the radius parameter and J is the total spin of the nucleus. The effect of the deformability parameters δ_1 and δ_2 has been checked and found to be insignificant. The shape of α energy spectra depends mostly on the level density parameter and partly on the potential parameters. The normalized fits from statistical model calculation are shown in Fig.4.12 in comparison with the data. The solid curve is the prediction for first chance α evaporation from the compound nucleus with a subsequent n emission while the dashed line represents the prediction for first chance n evaporation followed by α emission. Same normalization has been used for both the curves. It is clear from the Fig.4.12 that ($n\alpha$) decay has insignificant contribution

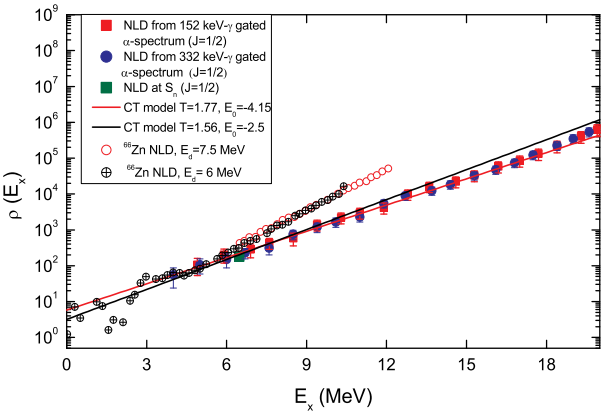

Figure 4.13: Nuclear level densities as a function of excitation energy. Histogram represents the NLD taken from RIPL3, filled symbols represent the present extracted NLD from γ-gated alpha spectra, filled square (green) denotes the NLD from neutron resonance data determined at neutron binding energy [148]. Data for ^{69}Zn from present experiment is compared with the NLD of ^{66}Zn nucleus [149]

compared to (αn) decay channel above 12 MeV α energy. Thus the value of k has been extracted from the best-fit statistical model calculations using a χ^2-minimization in the energy range of $E_\alpha \sim$ 12-24 MeV. The extracted values of inverse level density parameter ($k = A/\tilde{a}$) are 9.5 ± 0.6 MeV and 9.7 ± 0.6 MeV from 152 keV and 332 keV γ-gated α spectra, respectively.

Finally, the experimental level density of residual nucleus has been determined in terms of the measured and calculated yields of α emission following the prescription of Refs.[150, 149, 151, 152]

$$\rho_{\rm exp}(E_X) = \rho_{\rm fit}(E_X)\frac{(d\sigma/dE)_{\rm exp}}{(d\sigma/dE)_{\rm fit}} \ . \tag{4.9}$$

here, $(d\sigma/dE)_{\rm exp}$ and $(d\sigma/dE)_{\rm fit}$ are proportional to the experimental and the best-fit theoretical α energy spectra, respectively. $E_X = U - E_\alpha^{\rm CM}$ is the effective excitation energy, where $E_\alpha^{\rm CM}$ is the alpha energy in the center-of-mass frame. It should be pointed out that the state with maximum angular momentum in the level scheme of ^{68}Zn is found to be 12 $\hbar$ in the present reaction. Therefore, the angular momentum range of 152 keV and 330 keV γ-gated particle spectra are typically $\sim$ 6-12 $\hbar$ and $\sim$ 8-12 $\hbar$, respectively. Here, the mean angular momenta (J = 9±3 and 10±2 $\hbar$ for 152 keV and 332 keV γ-gated alpha spectra, respectively) have been considered in the calculation of level density. The ex-

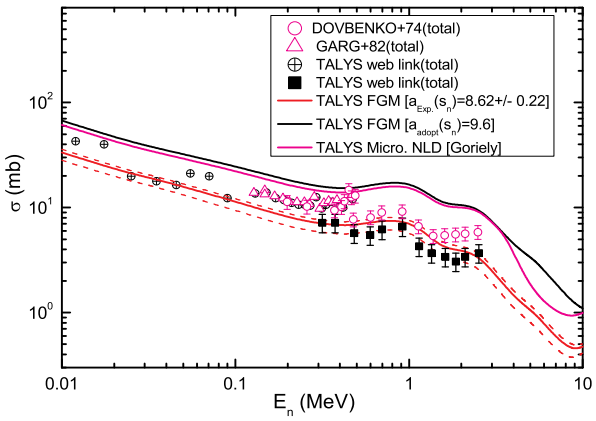

Figure 4.14: The ^{68}Zn(n, γ)^{69}Zn capture cross-section as function of neutron energy. Reported experimental data are compared with the results obtained from TALYS calculation using the present experimentally measured level density parameter.

tracted level density of ^{69}Zn residual nucleus as a function of excitation energy is shown in Fig.4.13. The uncertainty in the level density due to statistical model parameters has been checked and found to be $\sim$ 10%. The slope of the extracted level densities is normalized to the slope generated from the density of known levels in the discrete energy region *i.e* the RIPL data [153] and the level density at the neutron binding energy from neutron resonance data [148]. The comparison establishes the correctness of the slope of the extracted level density versus the energy curve for ^{69}Zn. The importance of this extracted NLD lies in the measurement of inverse level density parameter ($k = A/\tilde{a}$) from evaporated alpha energy spectra gated by the chosen low energy discrete γ-rays. In addition, the extracted NLD have been compared with constant temperature (CT) formula $\rho_{\mathrm{CT}} = \frac{1}{T}\mathrm{e}^{(E-E_0)/T}$. The value of E_0 and T are found to be -2.6 MeV and 1.6 MeV, respectively, which nicely explain the present extracted NLD as shown in Fig. 4.13. It should be pointed out here that the obtained E_0 and T do not corroborate with the systematic values reported in Ref.[154]. The latter reference, unlike the present work, has only used the RIPL data for normalization.

4.4.5 Extraction of level density parameter $a(S_n)$ and calculation of ^{68}Zn(n, γ)^{69}Zn capture cross-section

Furthermore, the extracted inverse level density parameter k is used to calculate the nuclear level density parameter a at neutron separation energy S_n from Eq. 4.3 for ^{69}Zn. Taking $U(S_n) = S_n - \Delta = 5.114$ MeV determined from $S_n = 6.48$ MeV and $\Delta = 1.368$ MeV [155] and $\delta S = 3.37$ MeV from Ref.[156], we obtained $a(S_n) = 8.625 \pm 0.225$ which is consistent with the result of Dilg *et al.* [157] for this nucleus. The value has been utilized subsequently in TALYS1.9 nuclear reaction code [136] to calculate ^{68}Zn(n, γ)^{69}Zn capture cross-section.The Fermi gas model of NLD [147] has been used in the TALYS code. The neutron capture process is predominantly of $E1$ type, only the $E1$ strength function has been considered taking a generalized Lorentzian form [158]. Global neutron optical model potential valid over the energy region of 0.001 MeV to 200 MeV for the mass range of 24≤A≤209 as the neutron potential in the statistical model calculation [159]. In the code, all other parameters are kept fixed except the nuclear level density parameter, which is taken from the present measurement. Interestingly, it is observed that the reaction cross-sections obtained from TALYS calculation using the measured NLD parameter explain the available data quite nicely without any further normalization, as shown in Fig. 4.14. The estimation with the systematic value of NLD parameter a(S_n)=9.614 [136] clearly over predicts the data in the energy region of measurement. Finally, reaction rate and the Maxwell-Avarage cross-section (MACS) of ^{68}Zn(n, γ)^{69}Zn has been estimate as a function of the steller temperature shown in Fig. 4.15.

4.4.6 Conclusion

In summary, the low energy (E_γ = 152 and 332 keV) γ-gated alpha emission spectra from the reaction ^{9}Be + ^{64}Ni have been measured. The γ-gated alpha energy spectra is predominantly from the compound nuclear events ensured by the even spin, odd parity (6^- or 8^-) of the decaying states in ^{68}Zn, the residual nucleus from αn decay of compound nucleus ^{73}Ge. The measured alpha energy spectra have been compared with the statistical model calculations to extract the NLD parameter and utilized to extract the level density

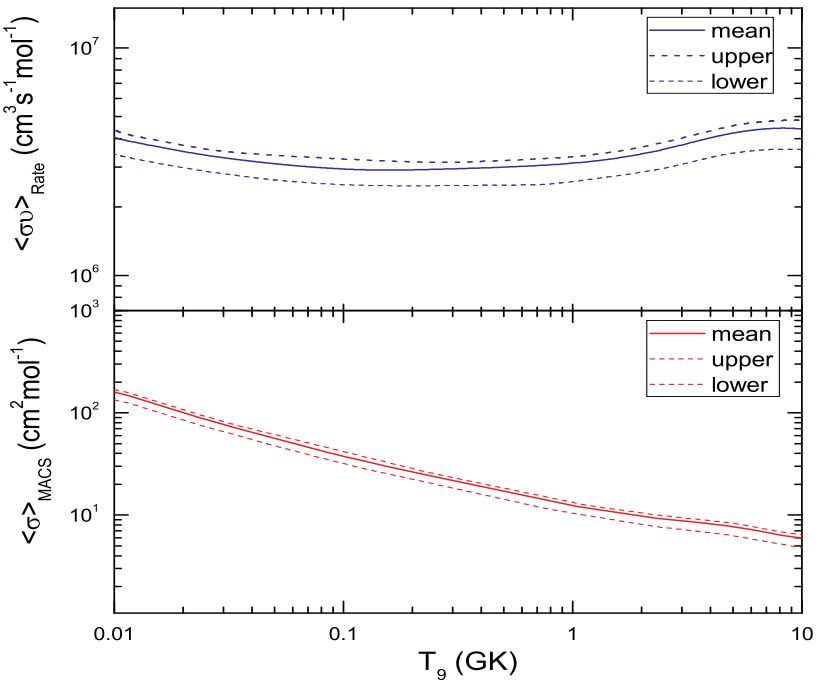

Figure 4.15: The racation rate and MACS cross-section variation with the steller temperature of ^{68}Zn(n, γ)^{69}Zn capture reaction.

of ^{69}Zn nucleus as a function of excitation energy. The obtained NLD parameter evaluated at neutron separation has been used in TALYS code to calculate the ^{68}Zn(n, γ)^{69}Zn capture cross-sections. The excellent agreement with measured (n, γ) cross-section achieves the objective of experimentally constraining the parameters of the statistical model for a more accurate description of astrophysical reactions.

Chapter 5

The $\alpha\alpha$(n, γ)^{9}Be capture reaction

The rapid neutron capture (r-process) mainly activated in explosive environment with a sufficiently high neutron flux ($\approx 10^{20}$ cm^{-3}) like in supernovae explosions [21], neutron star mergers [22]. It is found that the production of heavy elements in explosive nucleosynthesis scenario depends on the production rate of ^{9}Be. Formation of ^{9}Be in neutron rich explosive scenario in stars proceeds primarily through two steps. First step consists of $\alpha + \alpha \rightarrow {}^8$Be formation and then in the second step n- capture by ^{8}Be to form ^{9}Be, i.e. through ^{8}Be(n, γ) reaction. This reaction path of formation of ^{9}Be bridges the mass stability gap at A = 5 and 8. Subsequently, the production of heavy nuclei in explosive nucleosynthesis-scenario is sensitive to the rate of ^{9}Be production [24].

5.1 Earlier Work and Motivation of the present work

Arnold et al. [160] estimated from ^{9}Be(γ, n)^{8}Be reaction, that 1/2$^+$ first excited state at 1.68 MeV has almost full contribution in $\alpha(\alpha$n, $\gamma)^9$Be reaction rates at all temperatures and the estimated rate is 40% larger than the NACRE [168] result for the energy range 1 GK $\leq$ T $\leq$ 5 GK, most important for r-process nucleosynthesis. Thus, the rate uncertainty is dominated by the cross-section uncertainty for that state. Notice that all but one of the evaluated virtual photon (e, e$'$) data produced a reduced transition strengths and γ-ray partial widths that are about half of the value of their real photon (γ, n) counter-

Table 5.1: Resonance parameters of the $1/2^+$ state of ^{9}Be from virtual and real photon experiments.

Reaction	Ref.	Γ_n (keV)	Γ_γ (eV)	B(E1) $\downarrow$ (e^2 fm^2)
(e, e′)	Clerc *et al.* [162]	150 ± 50	0.3	0.05 ± 0.02
(e, e′)	Kuechler *et al.* [163]	217 ± 10	0.27	0.054
(e, e′)	Glick *et al.* [164]	200 ± 20	0.34	0.068
(e, e′)	Barker *et al.* [165]	270	0.75	0.137
(e, e′)	Burda *et al.* [166]	274 ± 8	0.302 ± 0.045	0.054
(γ, n)	Barker *et al.* [167]	227 ± 50	0.577	0.106 ± 0.018
(γ, n)	Angulo *et al.* [168]	227 ± 15	0.51 ± 0.1	0.094 ± 0.020
(γ, n)	Utsunomiya *et al.* [169]	283 ± 50	0.598	0.107 ± 0.007
(γ, n)	Sumiyoshi *et al.* [170]	225 ± 50	0.568	0.104 ± 0.002
(γ, n)	Arnold *et al.* [160]	213 ± 6	0.738 ± 0.002	0.136 ± 0.002

parts. A comparison of resonance parameters of this $1/2^+$ state are shown in Table 5.1 from earlier work from virtual and real photon experiments. Another thing is that, any previous measurement did not address the possibility of contributions by the three-body processes [160] at the lowest temperatures. In this context, we would like to estimate the partial decay width Γ_γ and the ratio Γ_n/Γ for $1/2^+$ state from the same inelastic scattering experiment of ^{9}Be$(\alpha, \alpha')^9$Be* $(1/2^+)$. The motivation of the experiment is to populate the near threshold resonance states by inelastic scattering and look for the decay particles in coincidence with the inelastically scattered ejectile to estimate the parameters.

5.2 Scheme of the present Work

In this work, we intend to employ the ^{9}Be$(\alpha, \alpha')^9$Be* inelastic scattering of energetic α particles to populate the near threshold states in ^{9}Be. The excited states of ^{9}Be decay by emission of a neutron through the two body decay channels ^{8}Be+n and ^{4}He+^{5}He, which decays immediately to ^{4}He+n and through the three body decay channel α+α+n. The state of particular interest, *i.e.* the $1/2^+$ state at 1.68 MeV excitation, decays predominantly by the 2-body channel ^{8}Be+n and the 3-body channel $\alpha + \alpha + n$. The experimental plan is to detect the α particles inelastically scattered from the excited states of ^{9}Be, both in *singles*

and in kinematic *coincidence* with the two decay α particles. The yield of the singles inelastically scattered α particle will provide the population of a particular resonant state in ^{9}Be, that can decay by particle as well as γ emissions. Thus an estimate of the total width Γ can be obtained from it with the proper knowledge of the other sources of the width of the peak in the experimental spectrum. On the other hand, the yield of scattered α in coincidence with the two decay α particles (after efficiency correction) from a resonant state of ^{9}Be will indicate the fraction of population that can decay by particle emission only and, hence, an estimate of the particle partial width. Thus the basic idea is that the ratio of the two yields can provide an estimate of the branching ratio Γ_n/Γ of the resonance state. In the same experiment, the inelastic scattering angular distribution data can be used to extract B(E1)/Γ_γ , which in turn can be used to obtain the partial γ width Γ_γ. However, in this chapter we will present our attempt to extract experimentally the particle width or the neutron branching ratio of ^{9}Be only.

5.3 Experimental details

The experiment was performed at Variable Energy Cyclotron Center, located at Kolkata, India. The detectors and targets were setup inside a scattering chamber of 150 cm diameter and the photograph of the setup is shown in Fig. 5.1. The ^{9}Be and standard Au targets were mounted on a target lader shown at the centre. The metallic ^{9}Be target is self-supported with $\approx$ 99 % enrichment and of thickness about 1.409 mg/cm^2. The target was bombarded with 34.5 MeV α beam from K130 cyclotron populating exited states of ^{9}Be via inelastic scattering. The Au foil of thickness 2 mg/cm^2 was also used for detector calibration at high energy. Typical beam current used for the experiment was $\sim$ 1 nA.

5.3.1 Target thickness measurement

The charge particle energy loss technique was used to measure the thickness of the target using a triple-α source containing ^{239}Pu (<E_α>=5.147 MeV), ^{241}Am (<E_α>=5.480 MeV) and ^{244}Cm (<E_α>=5.790 MeV). A silicon ORTEC Make surface barrier detector of thick-

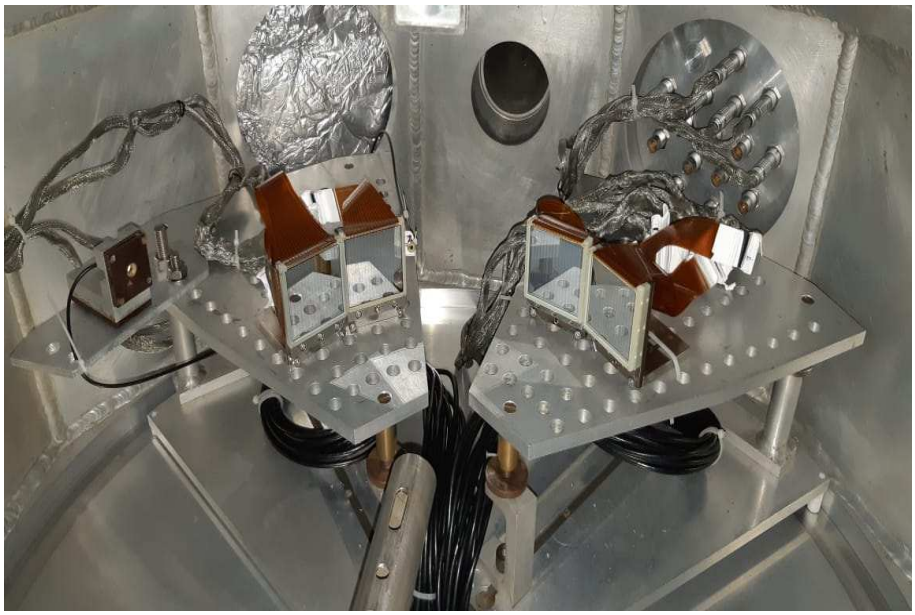

Figure 5.1: The schematic of detector setup at VECC.

ness 100 μm with standard electronic setup was used for α detection. The alpha energies from the 3-line source was also used for energy calibration. The energy difference between the alpha energy peaks corresponding to the with foil and without foil conditions were measured. The energy loss (ΔE) of α-particles in the target foil were used to and the effective thickness (ΔX) of the target was estimated using the relation

$$\Delta X = \frac{\Delta E}{(\frac{dE}{dx})} \tag{5.1}$$

where $\frac{dE}{dx}$(E) is specific energy loss of α-particles in ^{9}Be foil at energy E (taking from SRIM 2013 calculation). ΔX is effective thickness of Mylar foil in between source and detector. Now we estimated effective thickness of Mylar for three peak and averaging three thickness value from three α-peak energy. The thickness found to be 1.409 mg/cm^2 for ^{9}Be from this method.

5.3.2 Detector setup

The photograph of the detector setup in the present experiment is shown in Fig. 5.2. The inelastically scattered α particle was detected using two strip detector telescopes with 500

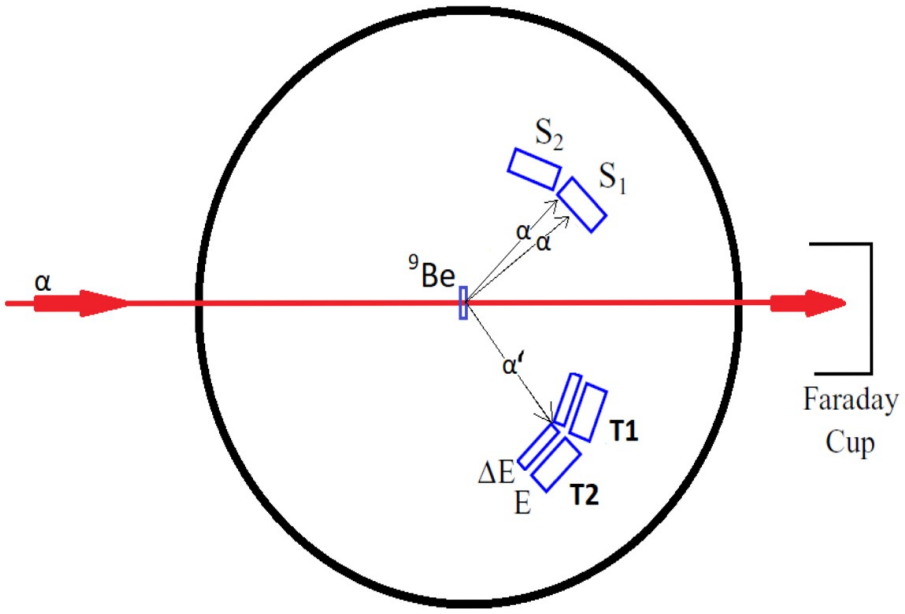

Figure 5.2: The schematic of detector setup at VECC.

μm thick stop E detectors and 50 μm thick transition ΔE detectors (henceforth labeled as T1 and T2). The telescopes are placed at 17 cm from the target on one side of the beam axis. The angular coverage of each telescope is about 16°. From LISE++ [171] kinematic calculation, the maximum energy of α-particles scattered elastically from gold target for beam energy of 34.5 MeV, and lab angle of 18° , is 33 MeV. So thickness of the telescope setup were sufficient to stop maximum energy scattered α-particles. The α-particles emitted from the decay of ^{9}Be resonance state were detected in coincidence with the inelastically scattered particles, using two 500 μm double-sided silicon strip detectors (DSSD) with 16 strips (each 50 mm $\times$ 3 mm) per side in mutually orthogonal directions. The detectors were placed in the forward angles with angular coverage of $\sim$ 52deg (labeled S1 and S2 hereafter). This thickness was also sufficient to stop alphas coming from ^{9}Be decay. The detector angles were chosen to fulfill the kinematic coincidence condition between the inelastically scattered α particle and the ^{8}Be particle from ^{8}Be + n two body decay of ^{9}Be.

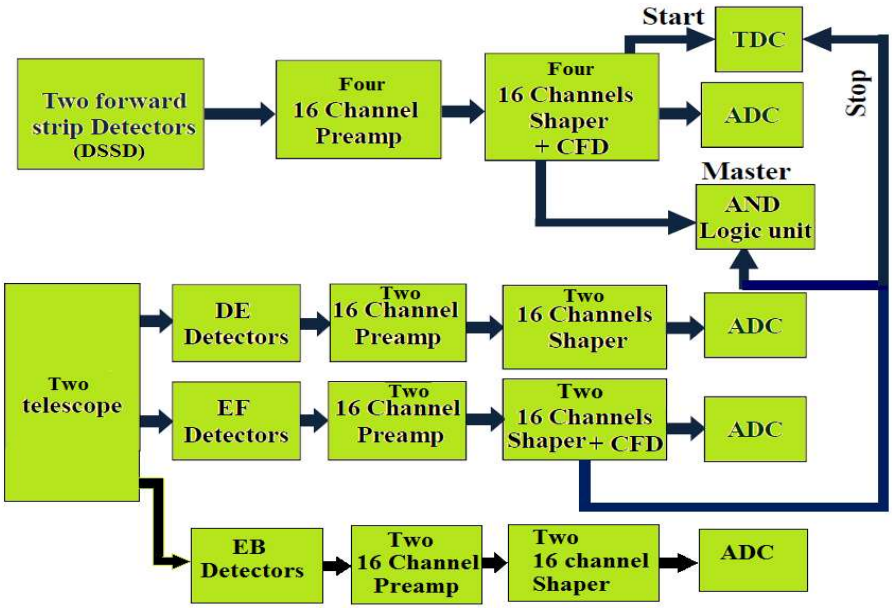

Figure 5.3: The schematic diagram showing the electronics of detector setup at VECC.

5.3.3 Electronics and Data Acquisition

The block diagram of electronics setup used in the present experiment has been shown in Fig. 5.3. As each Si-strip detector has 16 channels per side, so we have used 16 channels pre-amplifier MPR-16 module from Mesytec. The pre-amplifier output signal was a differential signal with fast rise time ($\sim$ 30 ns) and slow fall time ($\sim$ 50 μs) signal. The differential output of pre-amplifier is fed to the 16 channels amplifier MSCF-16 by Mesytec for further amplification and shaping. The output of the amplifier is a Gaussian shaped pulse of height $\sim$ a few volts and a width of 1 μs, which was directly fed to the analog to digital converter (ADC) (maximum of 8 volts, range of ADC) and stored using the data acquisition system. The MSCF 16 channel amplifier has in-built TFA (Timing-Filter-Amplifier- CFD (Constant Fraction Discriminator) circuit, for timing and threshold applications. In addition to the energy signal, these amplifiers also generate one OR-logic output of all 16 channels, which was used for master trigger generation after some logic operation. The amplifier signals were fed to 32 channel ADC (Model CAEN V778) for further processing with the help of a Versa-Module Eurocard (VME) based data acquisition system (DAQ) developed at VECC, Kolkata.

5.4 Data Analysis

In this section, the data analysis procedure adopted will be described. All the analysis procedures, have been developed using the C++ based ROOT platform.

5.4.1 Detector Calibration

In present experimental study there are in total 160 output channels (were four DSSD with 32 strips each and from two SSD detectors, each with 16 strips). The ADC channel number of each strip is calibrated separately. The energy calibrations has been performed twice, once before the actual experiment started, and finally after the experiment was over. The practice helped to identify the possible shift in the gain and deterioration of resolution during the experiment. To perform the energy calibration of the strips, ^{229}Th α-source has been used. The source has five groups of α energies (4.79, 5.82, 6.34, 7.07 and 8.38 MeV), the spectrum of which is shown in Fig. 5.4 for a particular strip. In the case of S_1, S_2 and ΔE strip detectors of the telescopes, the interest range of α energy is maximum of $\sim$ 10 MeV. Hence, only ^{229}Th source peaks have been used for calibration and the corresponding linear fitting for a single strip is shown in Fig. 5.5. But for E detectors of telescopes the energy of interest is upto $\sim$ 30 MeV. So these detectors are calibrated using elastic and inelastic scattering of α from ^{9}Be (ground state and 2.43 MeV state) and from Au (ground state) target respectively. The linear fitting for a typical strip of E (DSSD) detector is shown in Fig. 5.5.

5.4.2 Event selection

Depending upon noise in the experiment, set a threshold in data shorting programs to select only valid event and extract all event with full information from raw data. Next, energy calibration of each channel is done. The single DSSD detectors all ADC numbers are converted into the corresponding angular positions (θ, ϕ) in lab frame.

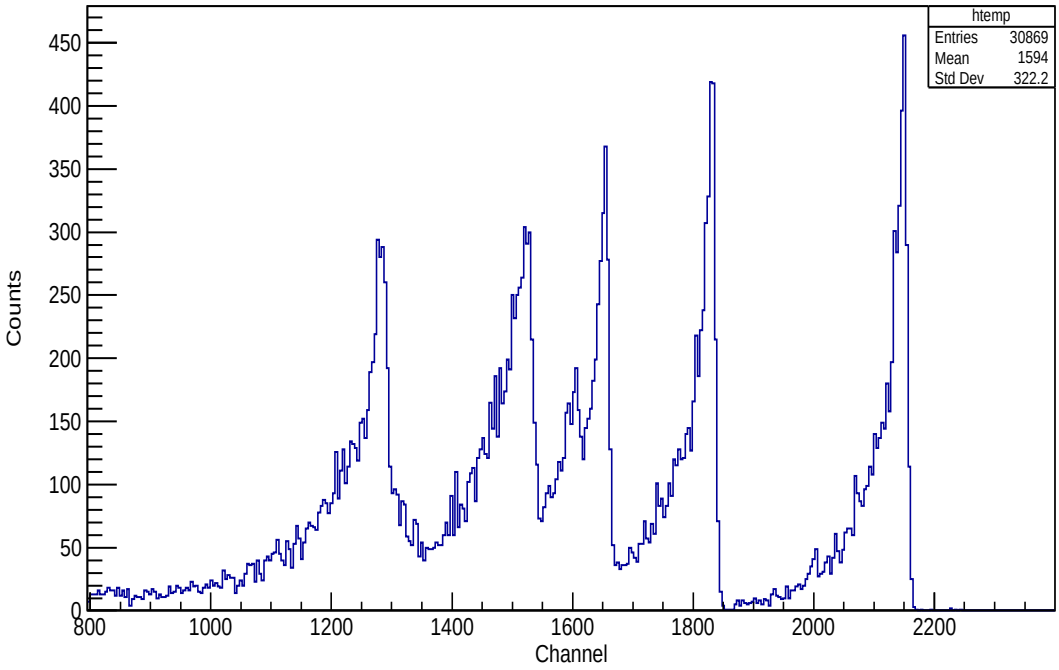

Figure 5.4: The example of ^{229}Th α-spectrum from a front strip of DSSD used for calibration.

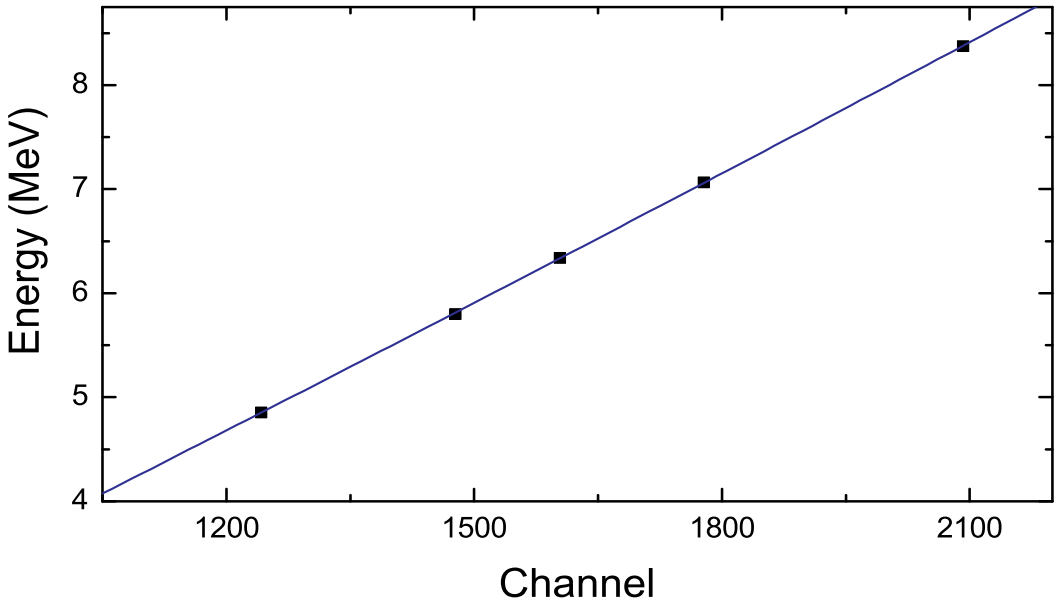

Figure 5.5: Calibration curve for a typical strip of 500m, The single E-detector .

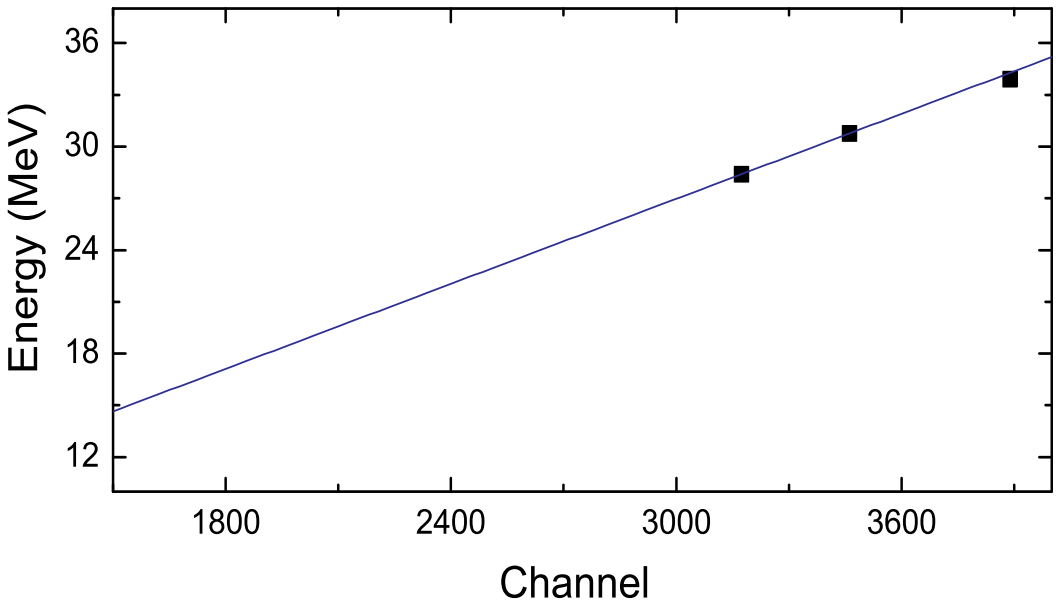

Figure 5.6: Calibration curve for a typical strip of E-ΔE telescope.

5.4.3 Extraction of scattered α energy spectrum

From sorted events the E-ΔE two dimensional spectrum has been generated for the telescope setup. A typical total energy (E+ΔE) vs. partial energy loss ΔE spectrum of the particles produced in the reaction of α particle with ^{9}Be target, at E_{lab} = 34.5 MeV, is shown in Fig. 5.7. From the Fig. 5.7, it is seen that good isotopic separation has been achieved for particles of charge Z = 1 and Z = 2. Setting the gate on the α band of the 2-dimensional spectrum, one dimensional E + ΔE total energy versus yield spectrum has been generated and is shown in Fig. 5.8. In Fig. 5.8 exited states of ^{9}Be are identified that are populated via inelastic scattering. At forward angle ($\theta_{lab} \approx 18^{\circ}$) spectrum showing better resolution is also shown in Fig. 5.9.

5.4.4 Coincidence event reconstruction

The main goal of present experiments is to study neutron producing decay channels of resonances of ^{9}Be resulting into two α particles in the exit channel and estimate the neutron decay branching ($\frac{\Gamma_n}{\Gamma}$) of low lying resonance states (mainly 1.68 MeV $1/2^{+}$ state) of ^{9}Be by inclusive and exclusive kinematic coincidence measurement. In this context, a

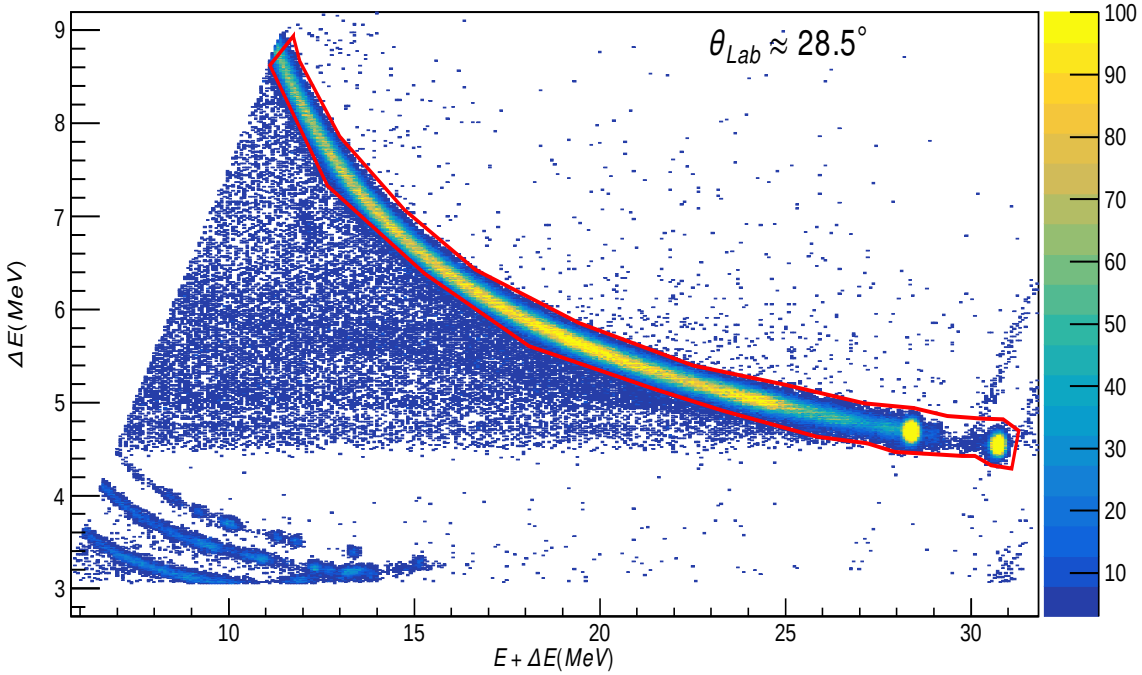

Figure 5.7: Two-dimensional scattered plot between ΔE vs. E for the of the E-ΔE telescope.

C++ program has been developed to extract kinematically correlated events of three α particle (two are from the ^{8}Be decay along with the inelastically scattered one detected separately) from the raw data. In the first step, the scattered α-particle is identified in the telescope by the particle identification method [172]; Then for each detected α in telescope, the programme look for two hits in the singles detectors and store the information as an interesting event for further processing. In the next step, the relative and total energy distribution between two breakup hits can be calculated from their individual energies E_1 and E_2 and the opening angle of their velocity vectors θ_{12}, as given by

$$E_{rel} = \frac{m_2 E_1 + m_1 E_2 - 2\sqrt{m_1 m_2 E_1 E_2}\cos\theta_{12}}{m_1 + m_2} E_{total} = E_1 + E_2 \tag{5.2}$$

The programme to generate the relative energy spectra has been written in C++ and a copy of the programme, written for the present analysis, is given in the Appendix I.

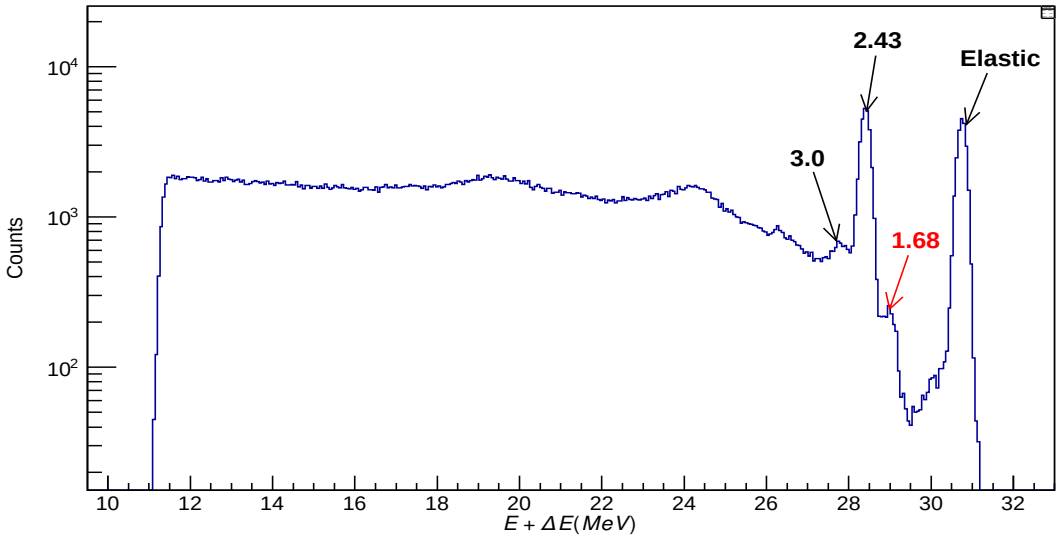

Figure 5.8: The α-particle energy spectrum in the E-ΔE telescope at θ_{lab} = 28.5°.

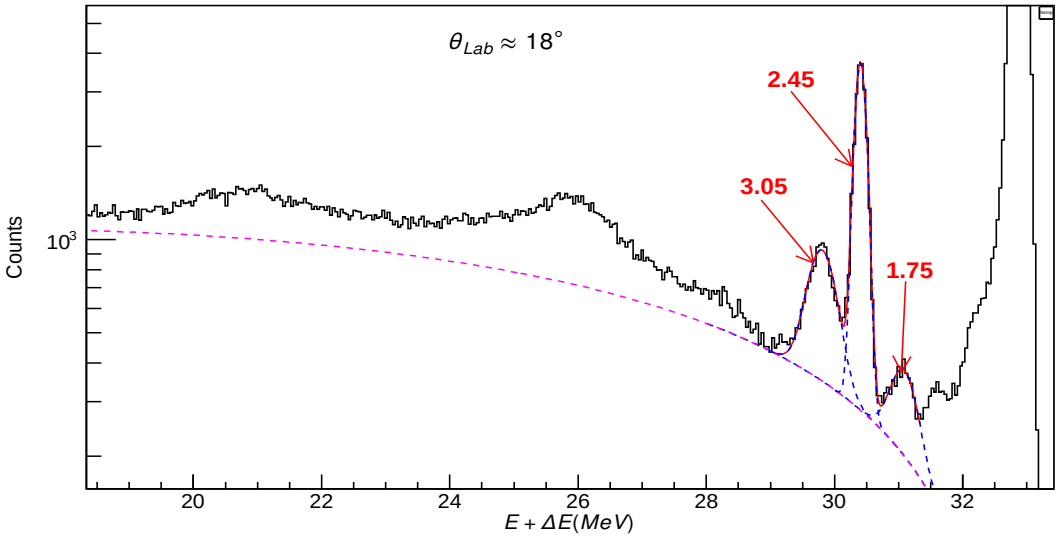

Figure 5.9: The α-particle energy spectrum in the E-ΔE telescope at $\theta_{lab} \approx 18°$.

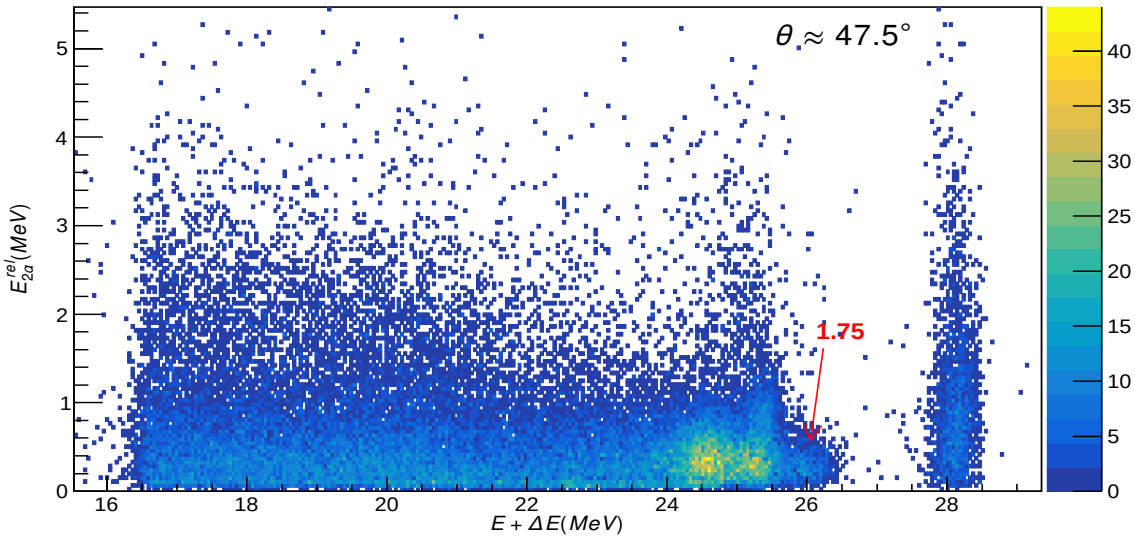

Figure 5.10: The relative energy of two decay particle vs. the energies scattered α-particles two-dimensional scattered plot at $\theta_{lab} \approx 47°$.

5.5 Results

Estimation of total width

In the one dimensional projection spectrum of total energy E+ΔE from the telescopes, the peaks corresponding to scattered α particles are identified and shown in Fig. 5.9. The FWHM and peak positions of elastic and $1/2^+$ resonance state obtained by the Gaussian fit of corresponding peaks in the energy calibrated spectrum. Subtracting in quadrature the FWHM of the elastic peak, which includes the beam resolution, spread due to electronic noise and energy straggling in the target, from the FWHM of peak from the resonant $1/2^+$ state, the actual width of the state (Γ) is estimated. Same procedure is also followed for the 2α-gated inelastic peaks for these $1/2^+$ state 2α-decay width($\Gamma_{2\alpha}$). The observed widths and energy location of these $1/2^+$ state are listed in Table 5.2 and 6.1.

Table 5.2: The measured widths(Γ) and excitation energy(E_x) for low lying resonance states of ^{9}Be.

E_x (MeV)	J^π	Angle Lab	Γ_R keV	Γ_R(Present) keV	Γ_R(Litt.) keV
		18.5°	283±24		274.3±8 [166]
1.75±0.15	$1/2^+$	19.5°	284±28	280±26	283±42 [169]
		28.5°	277±25		213.73±6 [160]
		33°	276±27		270.7 [165]
					227.5±50 [167]

Table 5.3: The measured widths($\Gamma_{2\alpha}$) gated by 2α for low lying resonance states of ^{9}Be.

E_x (MeV)	J^π	Angle Lab	$\Gamma_{2\alpha}$ keV	$\Gamma_{2\alpha}$(Present) keV	Γ_n(Litt.) keV	$\frac{\Gamma_{2\alpha}}{\Gamma_R}$(Present) keV	$\frac{\Gamma_n}{\Gamma_R}$(Litt.) keV
		47.5°	270±24		274±8		
1.75±0.15	$1/2^+$	46.5°	273±26	273±26	213±6 [160]	0.97	1.0 [160]
			276±25		270 [165]		
					227±50 [167]		
					283±42 [169]		

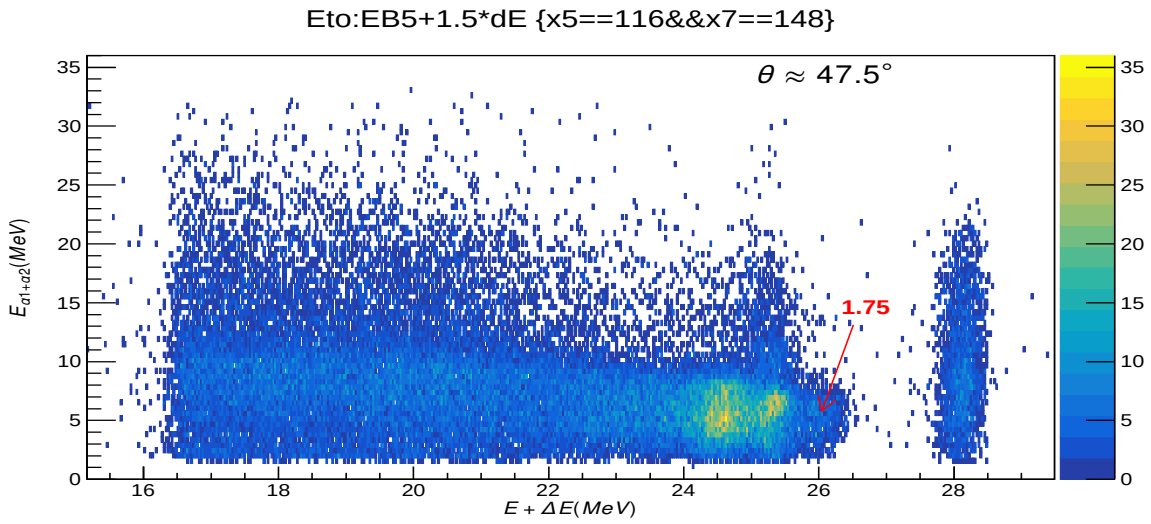

Figure 5.11: The total energy of two decay particle vs. scattered α-particles energies two-dimensional scattered plot at $\theta_{lab} \approx 47°$.

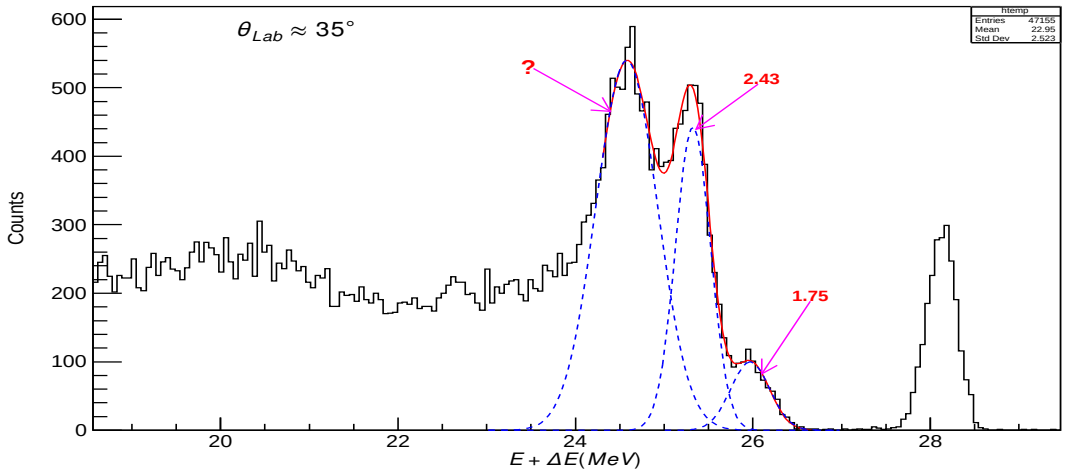

Figure 5.12: The x-projection spectrum of Fig. 5.10.

5.5.1 Conclusion

The scattered α-particles from ^{9}Be target in singles and in coincidence with the two decay α-s from a resonant state of ^{9}Be were measured. In scattered α spectrum (both in singles and in coincidence) the $1/2^{+}$ state at 1.68 MeV is identified and fitted with Gaussian functions.The Gaussian functions FWHM of the corresponding peaks in the α energy spectrum provide the measure of the total width and the neutron decay width of the state. The resulting neutron branching ratio is comparable with the adopted value of real photon experiments.

The measured Γ_R and $\Gamma_{2\alpha}$ width are almost equal within the error as expected due to very small Γ_γ(<1eV) [160]. The present Γ_R and $\Gamma_{2\alpha}$ values are comparable with the (γ,n) measurement Utsunomiya *et al.* [169] and are also within the error bars with the result of (e, e′) [162, 163, 164, 165, 166] and (γ,n) [167, 168, 169, 170, 160]. Howevers, the widths obtained from the present inelastic scattering experiment are higher compared to the latest precision (γ,n) measurement of Arnold et al. [160].

Chapter 6

6.1 Development of a hybrid telescope

The term telescope in experimental nuclear physics stands for a combination of two charged particle detectors, capable of identifying the charge and mass (at least for light ions) of the incident particles. The combination works on the principle of partial energy loss in a thin detector (ΔE) followed by a detector thick enough to stop the incident particle with residual energy (Stop E). Normally, the telescopes consist of a thin solid state detector as ΔE and another thick silicon semiconductor detector as stopping detector. Normal minimum 10 μm thickness of silicon detector are used as a ΔE detector in nuclear physics experiment. This thin silicon detectors have very poor energy resolution coming from large capacitance (C = $\frac{\epsilon_0 A}{d}$) and short life as they are very prone to radiation damage. Also the ΔE-E particle identification technique with silicon-silicon combination has a threshold dependence, governed by the thickness of the ΔE detector. A telescope with a 10 μm thick ΔE detector is capable of particle identification for minimum 3-4 MeV α-particles with low noise pulse processing electronics. For such low energy light ions, particle identification using a gas ΔE detector is an useful alternative. Such a combination of gas ΔE and solid state stop E detector for particle identification is termed as *hybrid* telescope setup. Gas ΔE has an important advantage that its active thickness can be varied by simply adjusting the gas pressure and thus making it a transmission type for low energy ions according to one,s requirement.

In the present work, we fabricate and characterize a hybrid telescope for alpha particles

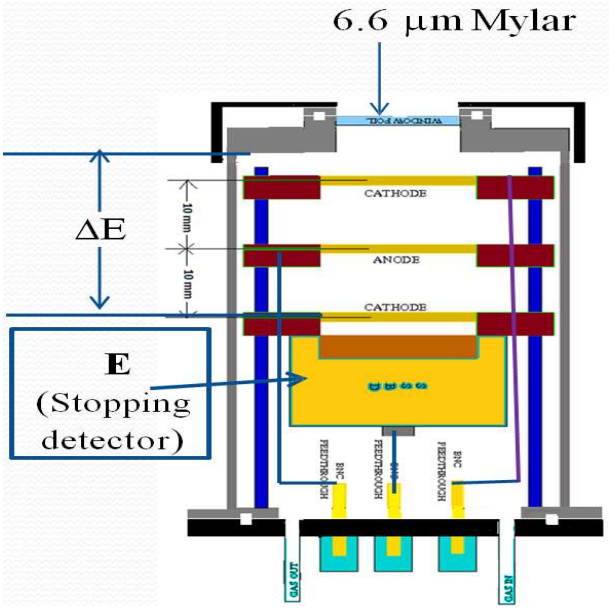

Figure 6.1: The block diagram of E-ΔE telescope.

with energy ranging from 5 MeV to about 1 MeV. We used standard radioactive α-source for this characterization.

6.2 Detector structure

In Fig. 6.1, a schematic diagram of the hybrid telescope detector developed has been shown. The present hybrid telescope consists of an ionization chamber, followed by a Silicon surface barrier detector of thickness 100 μm and 200 mm^2 active area from ORTEC. The gas ΔE detector operate as an axial field ionization chamber. It has a three electrode geometry [173] with a central anode sandwiched between two cathodes. As shown in Fig. 6.1, the electrodes are mounted with their plane perpendicular to the direction of the incoming particle. In an axial geometry, a uniform electric field covering the entire ionization volume can be maintained. The electrodes are fabricated using 25 μm diameter gold plated tungsten wires. The stretched wires are soldered on a 1.6 mm thick annular printed circuit board (PCB) with a pitch of 1mm. Inter electrode distance is 10 mm giving a two-stage active length of 20 mm inside the gas volume. The wire frames are a cathode, a central anode frame, and another cathode wire frame. The distance be-

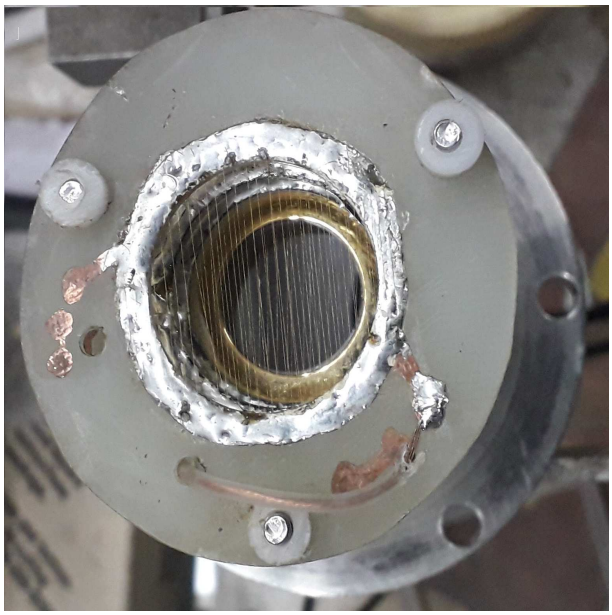

Figure 6.2: The assembled wire frame.

tween adjacent wire frames is 10 mm. Diameter of the active region is 20 mm. Fig. 6.2 shows an assembled wire frame. The detector is operated within a range of electric field to pressure (E/p) ratio values of 1 to 8 Volt.cm^{-1}.mbar^{-1} maintaining the operation in the ionization region. Typical working pressures of the detector are in the range of 24-288 mbar with Isobutene(C_4H_{10}) gas, depending on the measurements to be performed. The particles enter the detector through a Mylar window. Thickness of the Mylar window used is 6 μm. The signals from the anode of the gas detector and from the Silicon surface barrier detector are processed using the MSI-8 module of charge sensitive pre-amplifier and shaper amplifier combination.

6.3 Offline performance of the detector

The detector is tested in the laboratory with a 3-line α source with average energy of 5.147 MeV from ^{239}Pu, 5.485 MeV from ^{241}Am and 5.79 MeV from ^{244}Cm. Main motivation of the work is to study the performance of the hybrid detector as a telescope upto how much low energy. To obtain lower energy alphas, absorber foils have been used before the detector. The calibration of the Silicon stop detector is done without introducing any gas

Table 6.1: The gas pressures and electric fild between anode-cathode.

Gas	pressure(P) mbar	electric fild (E) V. cm^{-1}	$\frac{E}{P}$ V. cm^{-1}. $mbar^{-1}$
Isobutene(C_4H_{10})	238	270	1.13
	147.4	266	1.8
	78.6	200	2.56
	53.6	200	3.77
	24.7	200	8.0

in the detector and without any absorber foil. Also in each stage of increasing thickness, the energy of the alpha particle incident on the detector has been determined form the stop detector without any gas in the active volume. For different set of initial α-energy values, the gas pressure has been optimized to obtain sufficient signal strength above the noise level from both the gas ΔE and stop E detectors. As mentioned earlier, the primary motivation here is to achieve a reasonable sensitivity with this detector configuration in energy identification at very low energy. Thus, the optimum sensitivity of the detector as a telescope has been studied down to a lowest energy value of 0.89 MeV α particles with suitable combination of electric field and pressure or E/p value in the ionization region. The resultant two- dimensional ΔE vs. E spectra for different gas pressures in the ΔE detector are shown in Figs. 6.3 6.4 6.5 6.6. Even for an α energy of less than 1 MeV the response of the detector is reasonable shown in Fig. 6.7.

6.3.1 Conclusion

In the present configuration and operating condition of the detector we could detect α-particles of energy just below 1 MeV. We used the detector in the laboratory with only α-particles. Therefore the natural extension is to use it with the beam and check the particle the particle identification capability of the detector. Also, by using a thinner window ($\sim$ 0.5 μm) and maintaining a stable gas flow mode in the detector, I would like to use the detector for the detection of light heavy ions like C and O. The particular interest is to use two such detectors in kinematic coincidence mode for detection of ^{12}C + ^{12}C from ^{24}Mg compound nucleus.

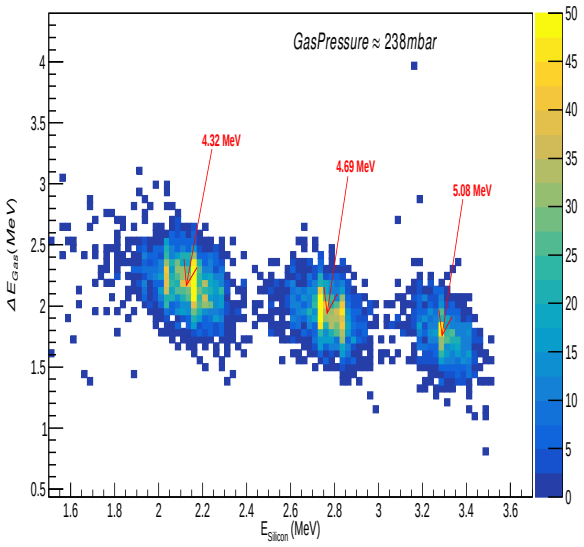

Figure 6.3: The two-dimensional scattered plot between ΔE(gas) vs E(silicon) for 238 mbar gas pressure.

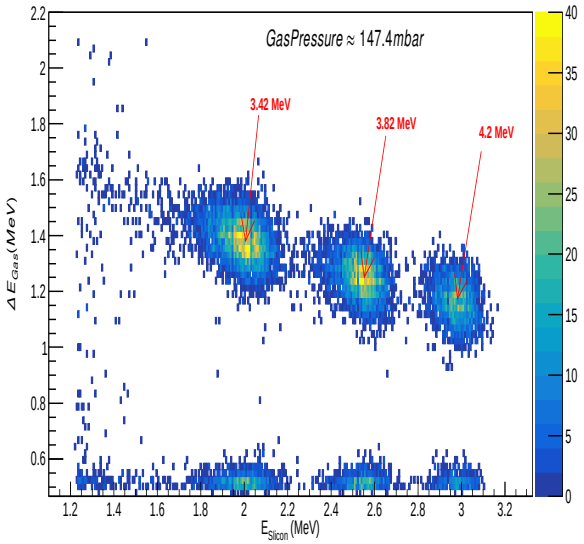

Figure 6.4: The two-dimensional scattered plot between ΔE(gas) vs E(silicon) for 147.4 mbar gas pressure.

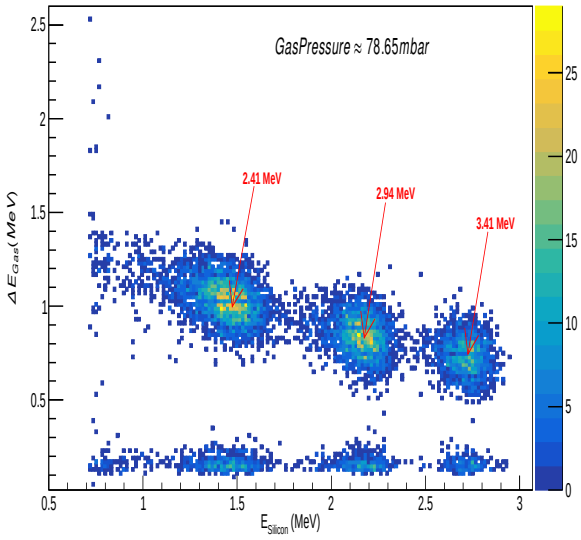

Figure 6.5: The two-dimensional scattered plot between ΔE(gas) vs E(silicon) for 78.6 mbar gas pressure.

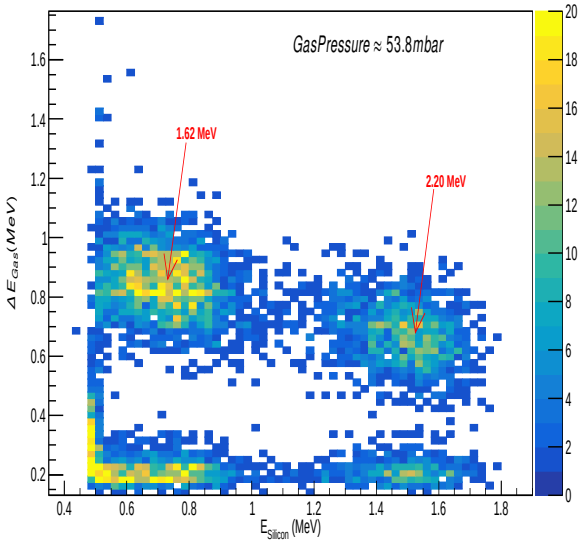

Figure 6.6: The two-dimensional scattered plot between ΔE(gas) vs E(silicon) for 53.8 mbar gas pressure.

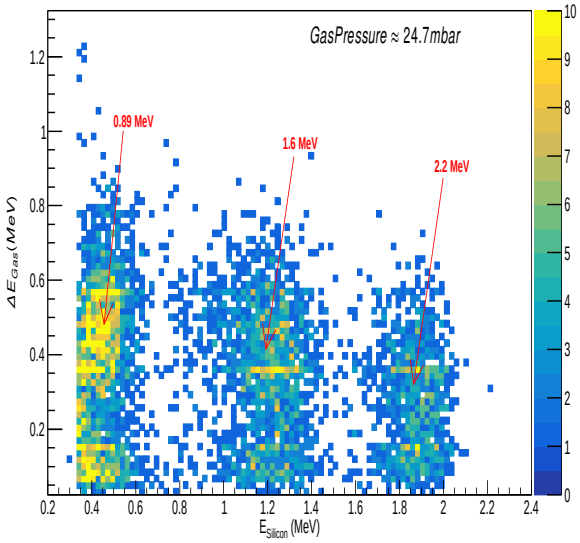

Figure 6.7: The two-dimensional scattered plot between ΔE(gas) vs E(silicon) for 24.7 mbar gas pressure.

Chapter 7

7.1 Future direction

In future, I have a plan to complete my work on ^{9}Be(α, α')^{9}Be. The analysis presented in the thesis is not a detailed one. I intend to construct the Q-value spectrum including the energy of the missing neutron from the ^{9}Be(α, α')2α + n reaction. The particle widths then be estimated more accurately. I also like to extend the work to look for the fractions of 2-body or 3-body configurations present in each of the near threshold resonances in ^{9}Be. The 1.68 MeV state of ^{9}Be is , the state through which the formation of ^{9}Be takes place predominantly, resonance state near the threshold of neutron decay. The width of this state is highly energy dependent. The energy dependence of the neutron width can be looked into, using the present triple coincidence data, by taking gates with smaller excitation energy bins over the width of the state. However, this will probably require a repeat experiment to gather higher statistics to get significant counts under gates with smaller energy bins. I would also like to complete the extraction of the angular distribution data corresponding to this 1/2^{+}, 1.68 MeV state of ^{9}Be and model the data with DWBA calculation to estimate the B(E1)/Γ_{γ} value.Also, I would like to continue my research work on experimental nuclear astrophysics using both the direct and the indirect techniques.

7.1.1 Direct methods

I am also interested to undertake direct measurement of low energy cross sections of ^{22}Ne(p, γ)^{23}Na capture reaction. My study of this reaction with existing data indicates the requirement of further measurement of some near threshold resonances. Significant uncertainty still exists for the resonance strengths of E_R = 68 and 100 keV states. The capture reaction ^{22}Ne(p, γ)^{23}Na is a competing reaction for the neutron producing reaction ^{22}Ne(α, n)^{25}Mg. A complimentary measurement of the (α, n) with the (p, γ) reaction can provide the necessary correlation in destroying ^{22}Ne and neutron production rates in the relevant astrophysical site.

7.1.2 Indirect methods

In nuclear astrophysics, neutron capture reactions in s-and r-processes of nucleosynthesis play a decisive role in the understanding of origin of elements heavier than iron. My plan is to study the neutron capture reactions via indirect (d, p-γ), (p, p'-γ) and (^{9}Be, ^{8}Be-γ) reaction on a few stable, isotopic chains of nuclei beyond iron that can lead to improved astrophysical rates in several ways. Also I would like to study (^{3}He, d), (^{6,7}Li, d/t) transfer reactions and Trojan horse method (THM) for A<25 mass regions for modeling of astrophysical (p, γ), (α, γ) and (p, α) or (α, n) reactions.

In the present thesis work, one of the highlights is the experimental determination of nuclear level density (NLD) parameter through the detection of first chance evaporation particle in coincidence with γ-rays of the residual nucleus. I intend to farther extended this technique for neutron capture on heavier nuclei. In present work the gamma strength function could not estimated through experiment. I intend to explore the particle-gamma coincidence technique for extraction of the gamma-ray strength function simultaneously with the level density (NLD).

7.2 List of references

Bibliography

[1] E.M. Burbidge, G.R. Burbidge, William Fowler and Fred Hoyle, Rev. Mod. Phys, **1957**, 29, 547-647.

[2] https://en.wikipedia.org/wiki/Abundance-of-the-chemical-elements.

[3] Ian J. Thompson and Filomena M. Nunes, Nuclear Reactions for Astrophysics(Cambridge University Press, Cambridge, **2009**).

[4] http://www.einstein-online.info/images/spotlights/BBN physI/reactions.gif.

[5] C Iliadis. Nuclear Physics of Stars. Wiley-VCH, **2007**.

[6] https://en.wikipedia.org/wiki/Proton

[7] F. Hoyle, Astro. J. Suppl., **1954**, 1, 121-146.

[8] H. O. U. Fynbo, Christian Aa. Diget, Uffe C. Bergmann, Maria J. G. Borge, Nature, **2005**, 433, 136-139.

[9] A. Coc, S. Ekstrom, P. Descouvemont, G. Meynet, J.-Ph. Uzan *et al.*, AIP Conference Proceedings, **2010**, 1269, 21-26.

[10] Straniero O, Chieffi A, Limongi M, Busso M, Gallino R and Arlandini C, Astrophys. J., **1997**, 487, 332-336.

[11] A. Boeltzig, C.G. Bruno, F. Cavanna, S. Cristallo, *et al.* Eur. Phys. J. A **2016**, 52-75.

[12] T. A. Weaver and S. E. Woosley, Phys. Rep., **1993**, 227, 65-96.

[13] F. Herwig. Evolution of Asymptotic Giant Branch Stars. Ann.Rev. Astron. and Astroph., **2005**, 43, 435-479, A. I. Karakas, M. Lugaro, C. Ugalde, M. Wiescher, and J. Gorres. Mg and Al production in intermediate-mass asymptotic giant branch stars. New A. Rev., **2006**, 50, 500-503.

[14] E. Carretta, S. Lucatello, R. G. Gratton, A. Bragaglia, and V. D'Orazi, Astron. Astrophys.**533**, A69 (2011). of the 23Na(p,γ)20Ne reaction rate. Astron. and Astrophys. , 457:995-1001, October 2006.

[15] R. G. Izzard, M. Lugaro, A. I. Karakas, C. Iliadis, and M. van Raai. Reaction rate uncertainties and the operation of the NeNa and MgAl chains during HBB in intermediatemass AGB stars. Astron. and Astrophys., **2007**, 466, 641-648.

[16] J. Jose, A. Coc, and M. Hernanz, Nuclear Uncertainties in the NeNa-MgAl Cycles and Production of ^{22}Na and ^{2}6Al during Nova Outbursts. Astroph. J., **1999**, 520, 347–360. from 11 to 120 $M_{\odot}$: The Hydrostatic and Explosive Contributions. Astroph. J., **2006**, 647, 483-500.

[17] C. E. Rolfs and W. S. Rodney. Cauldrons in the Cosmos: Nuclear Astrophysics. University of Chicago Press, **1988**.

[18] T.A. Weaver,G.B. Zimmerman and S.E. Woosley, Astrophys. J., **1978**, 225, 1021-1029.

[19] F. Kappeler, EPJ Web of Conferences, **2012**, 03006, 1-11.

[20] S. Goriely. Physics Letters B **1998**, 436, 10–18.

[21] S. E. Woosley, J. R. Wilson, G. J. Mathews, R. D. Hoffman, and B. S. Meyer, Astrophys. J. 433, 229 (1994).

[22] C. Freiburghaus, S. Rosswog, and F.-K. Thielemann, Astrophys. J. 525, 121 (1999).

[23] M. Terasawa, K. Sumiyoshi, T. Kajino, G. Mathews, and I. Thanihata, Astrophys. J. 562, 470 (2001).

[24] T. Sasaqui, K. T. Kajino, G. Mathews, K. Otsuki, and T. Nakamura, Astrophys. J. 634, 1173 (2005).

[25] T. Sasaqui, K. Otsuki, T. Kajino, and G. Mathews, Astrophys. J. 645, 1345 (2006).

[26] R. Surman and G. McLaughlin (private communication).

[27] A. Mengoni and T. Otsuka, AIP Conf. Proc. 529, 119 (2000).

[28] Tribble: R.E. Tribble, C.A. Bertulani, M. La Cognata, A.M. Mukhamedzhanov and C. Spitaleri, Rev. Prog. Phys. **2014**, 77, 106901 (1-49).

[29] L. Trache and F. Carstoiu, doi: 10.1007/s1143-000-0000-0(2019).

[30] Mukhamedzhanov A M and Timofeyuk N K, Sov. J. Nucl. Phys. **1990**, 51., 431. [Yad. Fiz. **1990**, 51, 679].

[31] D. W. Bardayan 2016 J. Phys. G: Nucl. Part. Phys. **2016**, 43, 043001 (1-25).

[32] F.M. Nunes, G. Potel, T. Poxon-Pearson, and J.A. Cizewski, Annu. Rev. Nucl. Part. Sci. **2020**, 70, 147-70.

[33] C.Rolfs, Nucl. Phys. A **1973**, 217, 29-70.

[34] A. Azhari, V. Burjan, F. Carstoiu, H. Dejbakhsh, *et al.*, Phys. Review. Letters **1999**, 82., 3960-3963.

[35] A. Azhari, V. Burjan, F. Carstoiu, V. Kroha, *et al.*, Phys. Review C **1999**, 60, 055803 (1-5).

[36] L. Trache, A. Azhari, F. Carstoiu, H. L. Clark, *et al.*, Phys. Review C *2003*, 67, 062801(R) (1-5).

[37] A. Banu, T. Al-Abdullah, C. Fu, C. A. Gagliardi, *et al.*, Phys. Review C *2009*, 79, 025805 (1-10).

[38] N.K. Timofeyuk, R.C. Johnson and A.M. Mukhamedzhanov, Phys. Review. Letters **2003**, 91, 232501 (1-4).

[39] Mukhamedzhanov A M and Tribble R E, Phys. Rev. C **1999**, 59, 3418-3424.

[40] Mukhamedzhanov A M, R. E. Tribble, and N. K. Timofeyuk, Phys. Rev. C **1995**, 51, 3472-3478.

[41] Mukhamedzhanov A M, H. L. Clark, C. A. Gagliardi, Y.-W. Lui, *et al.*, Phys. Rev. C **1997**, 56, 1302-1312.

[42] Mukhamedzhanov A M,C. A. Gagliardi, and R. E. Tribble, Phys. Rev. C **2001**, 63, 024612 (1-6).

[43] Mukhamedzhanov A M, A. Azhari, V. Burjan, C. A. Gagliardi, *et al.*, Phys. Rev. C **2002**, 66, 027602 (1-4).

[44] Mukhamedzhanov A M, P. Bem, B. A. Brown, V. Burjan, *et al.*, Phys. Rev. C **2003**, 67, 065804 (1-7).

[45] Mukhamedzhanov A M, A. Azhari, V. Burjan, C. A. Gagliardi, *et al.*, Nucl. Phys. A **2003**, 725, 279-294.

[46] C.R. Brune, W. H. Geist, R. W. Kavanagh, and K. D. Veal, Phys. Review. Letters **1999**, 83, 4025-4028.

[47] M.L. Avila, G. V. Rogachev, E. Koshchiy, L. T. Baby, *et al.*, Phys. Rev. C **2014**, 90, 042801(R) (1-5).

[48] M. L. Avila, G. V. Rogachev, E. Koshchiy, L. T. Baby, *et al.* Phys. Review. Letters **2015**, 114, 071101.

[49] E.D. Johnson, G. V. Rogachev, A. M. Mukhamedzhanov, L. T. Baby, **et al.**, Phys. Review. Letters **2006**, 97, 192701 (1-4).

[50] S Adhikari, C Basu, P Sugathan, A Jhingan, *et al.*, Journal Of Physics G **2017**, 44., 015102 (13pp).

[51] E.D. Johnson, G. V. Rogachev, J. Mitchell, L. Miller, and K. W. Kemper, Phys. Rev. C **2009**, 80, 045805 (1-9).

[52] L. Trache, F. Carstoiu, C. A. Gagliardi, and R. E. Tribble, Phys. Review. Letters **2001**, 87, 271102 (1-4).

[53] L. Trache, F. Carstoiu, C. A. Gagliardi, and R. E. Tribble, Phys. Rev. C **2004**, 032802(R) (1-5).

[54] A. Banu, L. Trache, F. Carstoiu, N. L. Achouri, *et al.*, Phys. Rev. C **2010**, 84, 015803 (1-7).

[55] F.M. Nunes, G. Potel, T. Poxon, and J. A. Cizewski, Ann. Rev. Nucl. Sci. **2020**, 70., 147-172.

[56] C. Spitaleri, M. Aliotta, S. Cherubini, M. Lattuada, *et al.*, Phys. Rev. C **1999**, 60., 055802 (1-7).

[57] A. Tumino, C. Spitaleri, M La Cognata, S Cherubini, *et al.*, Nature **2018**, 557., 687-690.

[58] M. La Cognata, C. Spitaleri, A. Mukhamedzhanov, A. Banu, *et al.*, Astrophys. J. **2010**, 708., 796-811.

[59] S. Cherubini, M. Gulino, C. Spitaleri, G. G. Rapisarda, *et al.*, Phys. Rev. C **2015**, 92., 015805 (1-7).

[60] R.G. Pizzone, M. La Cognata, L. L *et al.*, Eur. Phys. J. A **2016**, 52., 77 (1-9).

[61] A.M. Mukhamedzhanov, Phys. Rev. C **2011**, 84., 044614.

[62] C.A. Bertulani, M.S. Hussein and S. Typel, Phys. Lett. B **2018**, 776., 217-221.

[63] G. Baur, Phys. Lett. B **1986**, 178., 135-138.

[64] G. Baur, C. Bertulani and H. Rebel, Nucl. Phys. A **1986**, 458., 188-204.

[65] http://fpsalmon.usc.es/genp/doc/nuclear/experiments/s223/coulomb.shtml.

[66] A.V. Voinov, S.M. Grimes, A.C. Larsen, C.R. Brune, Phys. Rev. C **2008**, 77., 034613 (1-6).

[67] J. Escher, L Ahle, L Bernstein, J Burke, *et al.*, J.Phys.G **2005**, 31., S1687-S1690.

[68] J.E.Escher and F.S.Dietrich, Phys.Rev.C **2006**, 74., 054601 (1-16).

[69] Thomas Rauscher. Physical Review C **2010**, 81., 045807 (1-8).

[70] J. Jose and M. Hernanz, Astrophys. J. **1998**, 494., 680-690.

[71] C. Iliadis, A. Champagne, J. José, S. Starrfield, and P. Tupper, Astrophys. J. Suppl. Ser. **2002**, 142., 105-137.

[72] M. Pignatari, E. Zinner, P. Hoppe, C. J. Jordan, B. K. Gibson, R. Trappitsch, F. Herwig, C. Fryer, R. Hirschi, and F. X. Timmes, Astrophys. J. Lett. **2015**, 808., L43 (6pp).

[73] Direct Nuclear Reactions By G. R. Satchler, Clarendon Press Oxford,Oxford University Press-New York, **1983**.

[74] Pilachowski, C.A, Astrophys. J. **1988**, 237., L87 (6pp).

[75] G. Paltoglou and J.E. Norris, Astrophys. J. **1989**, 336., 185-206.

[76] K. Lind, C. Charbonnel, T. Decressin, F. Primas, F.Grundahl, and M. Asplund, Astron. Astrophys. **2011**, 527., A148 (1-16).

[77] D. Yong, F. Grundahl, D. L. Lambert, P. E. Nissen, and M. D. Shetrone, Astron. Astrophys. **2003**, 402., 985-1001.

[78] E. Uberseder. Private Communication, **2012**.

[79] A. M. Lane and R. G. Thomas. Review of Modern Physics **1958**, 30(2)., 257-353.

[80] M. Abramowitz and I. A. Stegun. Handbook of Mathematical Functions with Formulas, Graphs, and Mathematical Tables. Courier Dover Publications, **1964**.

[81] F.C. Barker and T. Kajino, Aust. J. Phys. **1991**, 44., 369-396.

[82] Blatt, J. M., and Weisskopf, V. F., Theoretical Nuclear Physics (New York: Wiley, 1962).

[83] J. Rekstad, A. Henriquez, F. Ingebretsen, G. Midttun, B. Skaali, R. Фуан, J. Wikne, T. Engeland, T. F. Thorsteinsen, E. Hammaren, et al., Phys. Scr. **1983**, T5., 45-50.

[84] L. Henden, L. Bergholt, M. Guttormsen, J. Rekstad, T. Tveter, Nuclear Physics A **1995**, 589., 249-266.

[85] T. Tveter, L. Bergholt, M. Guttormsen, E. Melby, J. Rekstad, Physical Review Letters **1996**, 77., 2404-2407.

[86] A. Schiller, L. Bergholt, M. Guttormsen, E. Melby, J. Rekstad, S. Siem, Nucl. Instrum. Methods Phys. Res. A **2000**, 447., 498-511.

[87] Mary Beard, Ethan Uberseder, and Michael Wiescher, EPJ Web of Conference **2015**, 93., 04001.

[88] Robert M. Cavallo, Allen V. Sweigart, Roger A. Bell, The Astrophysical Journal **1998**, 492., 575-595.

[89] P.L. Cottrell and G.S. Da Costa, Astrophys. J. **1981**, 245., L79 (6pp).

[90] Pilachowski, C.A, 1988, Astrophys. J. 237, L87, (1988).

[91] G. Paltoglou and J.E. Norris, Astrophys. J. **1989**, 336, L37-L39.

[92] K. Lind, C. Charbonnel, T. Decressin, F. Primas, F.Grundahl, and M. Asplund, Astron. Astrophys. **2011**, 527., A148 (1-16).

[93] D. Yong, F. Grundahl, D. L. Lambert, P. E. Nissen, and M. D. Shetrone, Astron. Astrophys. **2003**, 402., 985-1001.

[94] J. Jose and M. Hernanz, Astrophys. J. **1998**, 494., 680-690.

[95] C. Iliadis, A. Champagne, J. José, S. Starrfield, and P. Tupper, Astrophys. J. Suppl. Ser. **2002**, 142., 105-137.

[96] M. Pignatari, E. Zinner, P. Hoppe, C. J. Jordan, B. K. Gibson, R. Trappitsch, F. Herwig, C. Fryer, R. Hirschi, and F. X. Timmes, Astrophys. J. Lett. **2015**, 808., L43 (6pp).

[97] C. Rolfs, W.S. Rodney, M.H. Shapiro and H. Winkler Nucl. Phys. A **1975**, 241., 460-486.

[98] J. G*ö*rres, H. W. Becker, L. Buchmann, C. Rolfs, P. Schmalbrock, H.P. Trautvetter, and A. Vlieks, Nucl. Phys. A **1983**, 408., 372-396.

[99] S. E. Hale, A. E. Champagne, C. Iliadis, V. Y. Hansper, D. C.Powell, and J. C. Blackmon, Phys. Rev. C **2001**, 65., 015801 (1-11).

[100] A. L. Sallaska, C. Iliadis, A. E. Champange, S. Goriely, S. Starrfield, and F. X. Timmes, Astrophys. J. Suppl. Ser. **2013**, 207., 18 (58pp).

[101] F. Cavanna, R. Depalo *et al.* and LUNA Collaboration, Phys. Rev. Lett. **2015**, 115., 252501 (1-6).

[102] R. Depalo, F. Cavanna, M. Aliotta, M. Anders, D. Bemerrer, A. Best et al., Phys. Rev. C **2016**, 94., 055804 (1-13).

[103] K.J Kelly, A.E. Champagne, L.N.Downen, J.R. Dermigny, S. Hunt, C. Iliadis and A.L. Cooper Phys. Rev. C **2017**, 95., 015806 (1-22).

[104] F.Ferraro, M.P. Tak*á*cs, D. Piatti, F. Cavanna, *et al.*, Phys. Rev. Lett. **2018**, 121., 172701 (1-6).

[105] J. G*ö*rres, C. Rolfs, P. Schmalbrock, H.P. Trautvetter, and J. Keinonen, Nucl. Phys. A **1982**, 385., 57-75.

[106] Direct Nuclear Reactions By G. R. Satchler, Clarendon Press Oxford,Oxford University Press-New York, **1983**.

[107] P. Descouvemont and D. Baye, Rep. Prog. in Phys. **2010**, 73., 036301 (44pp).

[108] P Descouvemont. Private Communication, **2011**.

[109] C. R. Brune, Phys. Rev. C **2002**, 66, 044611.

[110] P Descouvemont and D Baye. Reports on Progress in Physics **2010**, 73., 036301 (44pp).

[111] M. Abramowitz and I. A. Stegun. Handbook of Mathematical Functions with Formulas, Graphs, and Mathematical Tables. Courier Dover Publications,1964.

[112] F.C. Barker and T. Kajino, Aust. J. Phys. **1991**, 44., 369-396.

[113] R.J. Holt, H.E. Jackson, R.M. Laszewski, J.E. Monahan, and J.R. Specht, Phys. Rev. C **1978**, 18., 1962-1972.

[114] A. Sattarov *et al.* Phys. Rev C. **1999**, 60., 035801 (7pp).

[115] I.J. Thompson, Comp. Phys. Rep. **1988**, 7., 167-212.

[116] J. R. Powers, H. T. Fortune, R. Middleton, and O. Hansen, Phys. Rev. C **1971**, 4., 2030-2046.

[117] P. Bem, V. Burjan, V. Kroha, J. Nov*á*k, *Š*. Pisko*ř*, E. *Š*imečkov*ă*, J. Vancour, C.A. Gagliardi, A.M. Mukhamedzhanov and R.E. Tribble, Phys. Rev. C **2000**, 62., 024320 (1-5).

[118] A.Terakawa et al., Phys. Rev. C **1993**, 48., 02775-2788.

[119] D.Y. Pang and A.M. Mukhamedzhanov, Phys. Rev. C **2014**, 90., 044611 (15pp).

[120] N. Keeley, K.W. Kemper and K. Rusek, Eur. Phys. J. A **2018**, 54., 71 (3pp).

[121] D. G. Jenkins, M. Bouhelal, S. Courtin, M. Freer, B. R. Fulton, F. Haas, R. V. F. Janssens, T. L. Khoo, C. J. Lister, E. F. Moore, W. A. Richter, B. Truett, and A. H. Wuosmaa, Phys. Rev. C **2013**, 87., 064301 (20pp).

[122] W. A. Childs, R. C. Ritter, B. D. Murphy, and R. M. Strang, Nucl. Phys. A **1973**, 203., 133-144.

[123] P. D. Kunz, program DWUCK4 (unpublished), extended version of J. R. Comfort (unpublished).

[124] R.E. Azuma, E. Uberseder, E.C. Simpson, C.R. Brune *et al.* Phys. Rev. C **2010**, 81., 045805 (17pp).

[125] E. Vogt, Rev. Mod. Phys. **1962**, 34., 723.

[126] C. Angulo, M. Arnould, M. Rayet, P. Descouvemont *et al.*, Nucl. Phys. A **1999**, 656., 3-183.

[127] A. Contos, J. Görres, A. Best, M. Couder *et al.*, Phys. Rev. C **2012**, 86., 055801 (14).

[128] R. B. Firestone, Nucl. Data Sheets **2007**, 108., 1-78.

[129] M. A. Meyer and J. J. A. Smit, Nucl. Phys. A **1973** , 205., 177-192.

[130] Thomas Rauscher, EXP2RATE V2.1, https://nucastro.org.

[131] E.P. Wigner and L. Eisenbud, Phys. Rev. **1947**, 72., 29-41.

[132] Nishimura *et al.*, MNRAS, **2017**, in press.

[133] Koloczek *et al.* Atomic Data and Nuclear Data Tables **2016**, 108., 1–14.

[134] S. Goriely, S. Hilaire, and A. J. Koning, Phys. Rev. C **2008**, 78., 064307 (14pp).

[135] F. Puhlhofer *et al.*, Nucl. Phys. A **1977**, 280., 267-284.

[136] A.J. Koning, D. Rochman, J.-Ch. Sublet, N. Dzysiuk, *et al.*, Nuclear Data Sheets **2019**, 155., 1–55.

[137] Balaram Dey, The Temperature Dependence Of Giant Diple Resonance Width at Excited States Of Atomic Nuclei, Ph.D Thesis, **2015**.

[138] Xin-Wu Su and Yin-Lu Han, International Journal of Modern Physics E **2015**, 24., 1550092 (18pp).

[139] H. A. Bethe, Phys. Rev. **1936**, 50., 332-341; Rev. Mod. Phys. **1937**, 9., 69-244.

[140] A. V. Ignatyuk, G. N. Smirenkin, and A. S. Tishin, Sov. J. Nucl. Phys. **1975**, 21., 255-258.

[141] J. Kopecky and M. Uhl, Phys. Rev. C **1990**, 41., 1941-1955.

[142] J. Kopecky, M. Uhl and R.E. Chrien,, Phys. Rev. C **1993**, 47., 312-322.

[143] Md. Moin Shaikh, Subint Roy, S. Rajbanshi, M. K. Pradhan, *et al.*, Phys. Rev. C **1995**, 51, 2942 (1-6).

[144] R. Palit, S.Saha, J. Sethi, T. Trivedi, *et al.*, Journal of Physics: Conference Series **2013**, 420., 012159 (9pp).

[145] R. Palit, S.Saha, J. Sethi, T. Trivedi, *et al.*, Nucl. Instrum. Methods A **2012**, 680., 90-96.

[146] J. F Bruandet, B. Berthet, C. Morand, A. Giorni, *et al.*, Phys. Rev. C **1976**, 14., 103-108.

[147] H. A. Bethe, Phys. Rev. 50, 332 (1936); Rev. Mod. Phys.9, 69 (1937).

[148] Till von Egidy and Dorel Bururescu, Phys. Rev. C **2005**, 72., 044311 (22pp).

[149] A. P. D. Ramirez, A. V. Voinov, S. M. Grimes, A. Schiller, C. R. Brune, and T. N. Massey., Phys. Rev. C **2013**, 88., 064324 (6pp).

[150] A. V. Voinov, S. M. Grimes, U. Agvaanluvsan, E. Algin, *et al.*, Phys. Rev. C **2006**, 74., 014314 (6pp).

[151] A. P. D. Ramirez, A. V. Voinov, S. M. Grimes, Y. Byun, C. R. Brune, T. N. Massey, S. Akhtar, S. Dhakal, and C. E. Parker., Phys. Rev. C **2015**, 92., 014303 (8pp).

[152] D. R. Chakrabarty, V. M. Datar, Suresh Kumar, E. T. Mirgule, *et al.*, Phys. Rev. C **1995**, 51., 2942-2951.

[153] https://www-nds.iaea.org/RIPL-3/.

[154] Nobuyuki. Iwamoto, Journal of Nuclear Science and Technology **2007**, 44., 1131-1141.

[155] https://www.nndc.bnl.gov

[156] P. Moller, J. R. Nix, W. D. Myers, Atomic Data and Nuclear Data Tables **1995**, 59., 185-381.

[157] W. Dilg, W. Schantl, H. Vonach, M. Uhl, Nuclear Physics A **1973**, 217, 269-298.

[158] J. Kopecky and M. Uhl, Phys. Rev. C **1990**, 41., 1941-1955.

[159] A.J. Koning and J.P. Delaroche, Nucl. Phys. A **2003**, 713., 231-310.

[160] C. W. Arnold, T. B. Clegg, C. Iliadis, H. J. Karwowski, G. C. Rich and J. R. Tompkins Phys. Rev. C **2012**, 85., 044605 (11pp).

[161] C. Angulo, M. Arnold, M. Rayet, P. Descouvemont *et al.*, Nucl. Phys. A **1999**, 656., 3-183.

[162] H.-G. Clerc, K. Wetzel, and E. Spamer, Nucl. Phys. A **1968**, 120., 441-459.

[163] G. Kuechler, A. Richter, and W. von Witsch, Z. Phys. A - Atomic Nuclei **1987**, 326., 447-454.

[164] J. P. Glickman *et al.*, Phys. Rev. C **1991**, 43., 1740-1757.

[165] F. Barker, Aust. J. Phys. **2000**, 53., 247-257.

[166] O. Burda, P. von Neumann-Cosel, A. Richter, C. Forssén, and B. A. Brown, Phys. Rev. C **2010**, 82., 015808 (7pp).

[167] F. Barker, Can. J. Phys. **1983**, 61., 1371-1373.

[168] C. Angulo, M. Arnould, M. Rayet, P. Descouvemont, *et al.*, Nucl. Phys. A **1999**, 656., 3-183.

[169] H. Utsunomiya, Y. Yonezawa, H. Akimune, T. Yamagata, M. Ohta, M. Fujishiro, H. Toyokawa, and H. Ohgaki, Phys. Rev. C **2000**, 63., 018801 (4pp).

[170] K. Sumiyoshi, H. Utsunomiya, S. Goko, and T. Kajino, Nucl. Phys. A **2002**, 709., 467-486.

[171] lise.nscl.msu.edu/lise.html.

[172] Glenn F. Knoll, Radiation Detection and Measurement, Fourth Edition (WILEY publishers, USA, **2011**).

[173] A. Jhingan, S. Barua, J.J. Das, T. Varughese, P. Sugathan, N. Madhavan, S. Nath, K. Kalita, S. Verma, Nucl. Instrum. Methods Phys. Res. A **2018**, 903., 326-334.

Chapter 8

```
  #include<iostream>
   #include<fstream>
   #include<iomanip>
   #include "TTree.h"
   #include <TMath.h>
   #include "TBrowser.h"
   #include "Riostream.h"
   #include "TCanvas.h"
   #include "TFile.h"
   #include "TNtuple.h"
   #include "TH1F.h"
   #include "TH2F.h"
void concidence()
{
//TH1F *h = new TH1F("h","histogram", 700,-1.0,10.0);
//TH2F *h2 = new TH2F("h2","histogram1", 500, 0.0, 35.0,500,0.0,20.0);
ifstream infile;
infile.open("/run/media/rajkumar/Seagate Expansion Drive/vecc_expt_data/
vme_data/1d_file/con95115.dat");
ofstream outfile;
outfile.open("/run/media/rajkumar/Seagate Expansion Drive/vecc_expt_data/
vme_data/1d_file/con95-115.dat");
ofstream outfile1;
outfile1.open("/run/media/rajkumar/Seagate Expansion Drive/vecc_expt_data/
vme_data/1d_file/plot.dat");
int n,cnt1=0,cnt2=0;
n=825239;

Double_t
d1,d2,d3,d4,th1,fi1,th2,fi2,th3,x1,x2,x3,x4,x5,x6,x7,EF1,EB1,EF2,EB2,dE,EF5,EB5,csth12,pi,Ere,Eto;
pi=3.14;

for(int i=1;i<n;i++)
{

infile>>x1>>EF1>>x2>>EB1>>x3>>EF2>>x4>>EB2>>x5>>dE>>x6>>EF5>>x7>>EB5;
cnt1++;

d1=abs(EF1-EB1),d2=abs(EF2-EB2),d3=abs(EF5-EB5);
//if(d1<0.0&&d2<0.0&&d3<0.0){
//d1=d1*-1,d2=d2*-1,d3=d3*-1;
//}
//if(d3<1.0){
//if(x5==124){
if(x1>31&&x2>31&&x3>31&&x4>31){
cnt2++;
th1=(x1-32)*1.38+45.45;
fi1=(55-x2)*1.34+0.67;
th2=(x3-32)*1.38+45.45;
fi2=(55-x4)*1.34+0.67;
//cout<<th1<<"  "<<d1<<"  "<<fi1<<"  "<<EB1<<"  "<<th2<<"  "<<EF2<<"  "<<fi2<<"
"<<EB2<<"  "<<x5<<"  "<<dE<<"  "<<x6<<"  "<<EF5<<"  "<<x7<<"  "<<EB5<<endl;
cout<<th1<<"  "<<EF1<<"  "<<fi1<<"  "<<EB1<<"  "<<th2<<"  "<<EF2<<"  "<<fi2<<"
"<<EB2<<"  "<<x5<<"  "<<dE<<"  "<<x6<<"  "<<EF5<<"  "<<x7<<"  "<<EB5<<endl;
outfile<<x1<<"  "<<EF1<<"  "<<x2<<"  "<<EB1<<"  "<<x3<<"  "<<EF2<<"  "<<x4<<"
"<<EB2<<"  "<<x5<<"  "<<dE<<"  "<<x6<<"  "<<EF5<<"  "<<x7<<"  "<<EB5<<endl;
//outfile<<th1<<"  "<<EF1<<"  "<<fi1<<"  "<<EB1<<"  "<<th2<<"  "<<EF2<<"  "<<fi2<<"
"<<EB2<<"  "<<x5<<"  "<<dE<<"  "<<x6<<"  "<<EF5<<"  "<<x7<<"  "<<EB5<<endl;
csth12=(cos(th1*pi/180)*cos(th2*pi/180))+(sin(th1*pi/180)*sin(th2*pi/180))*cos((fi1-
fi2)*pi/180);
Ere=(EF1+EF2-(2*sqrt(EF1*EF2)*csth12))/2;
Eto=EF1+EF2;
```

Figure 8.1:

```
//+(2*sqrt(EF1*EF2)*csth12))/2;
outfile1<<Eto<<"  "<<Ere<<"  "<<x5<<"  "<<dE<<"  "<<x6<<"  "<<EF5<<"  "<<x7<<"
"<<EB5<<endl;
//h2->Fill(EB5,Ere);
//h2->Fill(x1,x2);
//h2->Fill(x3,x4);
//h->Fill(Ere);
}

if(x1<32&&x2<32&&x3<32&&x4<32){
cnt2++;
th1=x1*1.34+22.2;
fi1=(23-x2)*1.34+0.67;
th2=x3*1.34+22.2;
fi2=(23-x4)*1.34+0.67;
//cout<<th1<<"  "<<d1<<"  "<<fi1<<"  "<<EB1<<"  "<<th2<<"  "<<EF2<<"  "<<fi2<<"
"<<EB2<<"  "<<x5<<"  "<<dE<<"  "<<x6<<"  "<<EF5<<"  "<<x7<<"  "<<EB5<<endl;
cout<<th1<<"  "<<EF1<<"  "<<fi1<<"  "<<EB1<<"  "<<th2<<"  "<<EF2<<"  "<<fi2<<"
"<<EB2<<"  "<<x5<<"  "<<dE<<"  "<<x6<<"  "<<EF5<<"  "<<x7<<"  "<<EB5<<endl;
outfile<<x1<<"  "<<EF1<<"  "<<x2<<"  "<<EB1<<"  "<<x3<<"  "<<EF2<<"  "<<x4<<"
"<<EB2<<"  "<<x5<<"  "<<dE<<"  "<<x6<<"  "<<EF5<<"  "<<x7<<"  "<<EB5<<endl;
//outfile<<th1<<"  "<<EF1<<"  "<<fi1<<"  "<<EB1<<"  "<<th2<<"  "<<EF2<<"  "<<fi2<<"
"<<EB2<<"  "<<x5<<"  "<<dE<<"  "<<x6<<"  "<<EF5<<"  "<<x7<<"  "<<EB5<<endl;
csth12=(cos(th1*pi/180)*cos(th2*pi/180))+(sin(th1*pi/180)*sin(th2*pi/180))*cos((fi1-
fi2)*pi/180);
Ere=(EF1+EF2-(2*sqrt(EF1*EF2)*csth12))/2;
Eto=EF1+EF2;
//+(2*sqrt(EF1*EF2)*csth12))/2;
outfile1<<Eto<<"  "<<Ere<<"  "<<x5<<"  "<<dE<<"  "<<x6<<"  "<<EF5<<"  "<<x7<<"
"<<EB5<<endl;
//h2->Fill(EB5,Ere);
//h2->Fill(x1,x2);
//h2->Fill(x3,x4);
//h->Fill(Ere);
}

if(x1<32&&x2<32&&x3>31&&x4>31){
cnt2++;
th1=x1*1.34+22.2;
fi1=(23-x2)*1.34+0.67;
th2=(x3-32)*1.38+45.45;
fi2=(55-x4)*1.34+0.67;
//cout<<th1<<"  "<<d1<<"  "<<fi1<<"  "<<EB1<<"  "<<th2<<"  "<<EF2<<"  "<<fi2<<"
"<<EB2<<"  "<<x5<<"  "<<dE<<"  "<<x6<<"  "<<EF5<<"  "<<x7<<"  "<<EB5<<endl;
cout<<th1<<"  "<<EF1<<"  "<<fi1<<"  "<<EB1<<"  "<<th2<<"  "<<EF2<<"  "<<fi2<<"
"<<EB2<<"  "<<x5<<"  "<<dE<<"  "<<x6<<"  "<<EF5<<"  "<<x7<<"  "<<EB5<<endl;
outfile<<x1<<"  "<<EF1<<"  "<<x2<<"  "<<EB1<<"  "<<x3<<"  "<<EF2<<"  "<<x4<<"
"<<EB2<<"  "<<x5<<"  "<<dE<<"  "<<x6<<"  "<<EF5<<"  "<<x7<<"  "<<EB5<<endl;
//outfile<<th1<<"  "<<EF1<<"  "<<fi1<<"  "<<EB1<<"  "<<th2<<"  "<<EF2<<"  "<<fi2<<"
"<<EB2<<"  "<<x5<<"  "<<dE<<"  "<<x6<<"  "<<EF5<<"  "<<x7<<"  "<<EB5<<endl;
csth12=(cos(th1*pi/180)*cos(th2*pi/180))+(sin(th1*pi/180)*sin(th2*pi/180))*cos((fi1-
fi2)*pi/180);
Ere=(EF1+EF2-(2*sqrt(EF1*EF2)*csth12))/2;
Eto=EF1+EF2;
//+(2*sqrt(EF1*EF2)*csth12))/2;
outfile1<<Eto<<"  "<<Ere<<"  "<<x5<<"  "<<dE<<"  "<<x6<<"  "<<EF5<<"  "<<x7<<"
"<<EB5<<endl;
//h2->Fill(EB5,Ere);
//h2->Fill(x1,x2);
//h2->Fill(x3,x4);
//h->Fill(Ere);
}
```

Figure 8.2:

```
//}
//h2->Fill(EF1,EF2);
//}
//}
//}
}
//h->Draw();
//h2->Draw("colz");
outfile1.close();
infile.close();
outfile.close();
cout<<cnt1<<"  "<<cnt2<<endl;
}
```

Figure 8.3: The C++ programme to generate the relative energy spectra.

Any other information

NA

Thesis Highlight

Name of the Student: RAJKUMAR SANTRA

Name of the CI/OCC: Saha Institute of Nuclear Physics, Kolkata

Enrolment No.: PHYS05201604018

Thesis Title: Indirect Experimental Technique For Nuclear Astrophysics

Discipline: Physical Sciences **Sub-Area of Discipline: Nuclear Astrophysics**

Date of viva voce: 25/05/2021

'Nuclear Astrophysics' is an overlay area of nuclear physics and astrophysics. In astrophysical environment, the energy at which the majority of capture reactions occur makes it difficult or some times impossible to probe in the laboratory. Indirect methods, based on low energy nuclear physics experimental techniques, have been developed, as an alternative, to determine the cross-sections of astrophysical reactions and to estimate the corresponding reaction rates.

The thesis explores some of the experimental techniques of nuclear reactions as indirect methods in the study of astrophysical capture reactions. The work deals with the modeling of the astrophysical capture cross sections with relevant quantities extracted from the nuclear reaction studies. Three different astrophysical capture reactions viz. ^{22}Ne(p, γ)^{23}Na of Ne-Na cycle, ^{68}Zn(n, γ)^{69}Zn of s-process nucleosynthesis path and αα(n,γ)^{9}Be of r-process nucleosynthesis path have been studied.

Asymptotic normalization constants of the bound states of ^{23}Na were estimated from finite range DWBA analysis of ^{22}Ne(^{3}He, d)^{23}Na transfer reaction data. A consistent analysis of the direct capture component of ^{22}Ne(p, γ)^{23}Na reaction was performed within the R-matrix framework, constrained with the asymptotic normalization constants of the bound states of ^{23}Na obtained from the transfer reaction calculation. The contribution of capture through the sub-threshold resonance at 8664 keV excitation in the total capture to the ground state of ^{23}Na was also determined. The observed rise in the astrophysical S-factor data for ground state capture, including the effect of capture through sub-threshold state, was reproduced nicely. The total direct capture S-factor at zero relative energy was found to be 48.8 ± 9.5 keV b, having less uncertainty. The value corroborates with the recent measurements. The total reaction rate obtained as a function of temperature differs from the recent estimations by Ferraro et al. in the temperature window of $0.1 \leq T \leq 0.2$ GK.

In the ^{68}Zn(n,γ)^{69}Zn reaction study, the thesis attempts the extraction of nuclear level density (NLD) of ^{69}Zn experimentally. Evaporated α-spectra have been measured in coincidence with the low energy γ-rays from the purely compound nuclear reaction ^{64}Ni(^{9}Be,αn)^{68}Zn at E(^{9}Be)=30 MeV . The first chance α emission spectrum, producing 69Zn, have been compared with statistical model calculation to extract the asymptotic value of NLD. Subsequently, with the asymptotic NLD, the NLD parameter at neutron separation energy of ^{69}Zn has been evaluated and used in the TALYS reaction code to calculate the ^{68}Zn(n, γ)^{69}Zn capture cross-sections. Excellent agreement with the measured (n, γ) cross-section, does highlight the objective of direct experimental determination of the parameters of statistical model for more accurate description of astrophysical reactions.

To investigate the formation of ^{9}Be in the explosive astrophysical scenario, we studied the population of near threshold states of ^{9}Be by inelastic α scattering and their decay by emission of two α particles. As the $1/2^{+}$ state at 1.68 MeV is of particular interest as a doorway for formation of ^{9}Be, the scattered α-particles from the state in singles and in coincidence with the two decay α-s were detected. The FWHM of the corresponding peaks in the α energy spectrum provide the measure of the total width and the neutron decay width of the state.